An investigation of the seakeeping behaviour of a polar vessel in waves

by

Armand van Zuydam

Thesis presented in partial fulfilment of the requirements for the degree of Master of Engineering (Mechanical) in the Faculty of Engineering at Stellenbosch University

Supervisor: Prof. A. Bekker
Co-supervisor: Prof. C. J. Meyer

March 2021

Declaration

By submitting this thesis electronically, I declare that the entirety of the work contained therein is my own, original work, that I am the sole author thereof (save to the extent explicitly otherwise stated), that reproduction and publication thereof by Stellenbosch University will not infringe any third party rights and that I have not previously in its entirety or in part submitted it for obtaining any qualification.

Date: March 2021

Abstract

An investigation of the seakeeping behaviour of a polar vessel in waves

A. van Zuydam

Department of Mechanical and Mechatronic Engineering,
University of Stellenbosch,
Private Bag X1, Matieland 7602, South Africa.

Thesis: MEng (Mech)

March 2021

The SA Agulhas II plays a crucial role in logistical and research support in the Southern Ocean and Antarctica. It is estimated that open water transits account for up to 85 % of her total voyages. She is built to Polar Class PC5 with a thick rounded stem and a full fore-body. Instinctively, these characteristics improve her performance in ice but may lead to sharp increases in open-water resistance and affect other seakeeping aspects. In particular, her spoon-shaped bow and flat raised transom predispose her to slamming.

In rough sea conditions, significant motions are induced, which subsequently leads to an increase in resistance and fuel consumption. To ensure efficient performance at sea, vessel owners must have knowledge about a ship's responses in these environments. Therefore, an investigation was undertaken to evaluate the seakeeping behaviour of the SA Agulhas II.

Full-scale measurements were conducted onboard the vessel during a cruise in the Southern Ocean. Data obtained from this campaign were used to determine the heave, roll and pitch motion responses in irregular waves. Strip theory was implemented to determine the motion Response Amplitude Operators of the vessel. Through superposition of the Response Amplitude Operators and the wave spectrum, the motion responses in irregular waves were predicted. A comparison between measured and predicted motion responses showed that heave and pitch could be predicted with reasonable accuracy. Roll motion showed various discrepancies and future research is recommended to study non-linear effects, such as roll damping.

Computational Fluid Dynamics was identified as an essential tool to investigate her motion responses and added resistance in head waves. During this

work, three speeds were evaluated, her design speed of 14 kn, a reduced speed of 10 kn, and an increased speed of 18 kn. Overall, the results showed that the maximum heave and pitch motions are expected to occur when the encounter frequency ranges between 0.124-0.143 Hz. For all three speeds, the maximum added resistance in waves was observed when large-amplitude motion occurs. It was further shown that a reduction of speed from 14 kn to 10 kn could decrease her effective power by 42 %. On the other hand, increasing speed by 4 kn from 14 kn to 18 kn could lead to a maximum increase in effective power of 87 %. Computational Fluid Dynamics investigations further showed that slamming could occur at the bow region of the SA Agulhas II even though she is not operating in extreme conditions. Computational Fluid Dynamics shows clear potential for further investigations into bow and stern slamming for the SA Agulhas II.

Uittreksel

'n Ondersoek van die seewaardigheidsrespons van 'n poolskip in golwe

(An investigation of the seakeeping behaviour of a polar vessel in waves'

A. van Zuydam

Departement Meganiese en Megatroniese Ingenieurswese,
Universiteit van Stellenbosch,
Privaatsak X1, Matieland 7602, Suid Afrika.

Tesis: MIng (Meg)

Maart 2021

Die SA Agulhas II speel 'n deurslaggewende rol in logistiek en navorsingsondersteuning in die Suidelike Oseaan en Antarktika. Na beraming behels 85% van haar werk operasies in oop water. Sy is geklassifisser as 'n ysklas skip en voldoen aan die stipulasies vir Pool Klas 5. Haar boeg is lepelvormig en haar longitudinale sentrum van dryfvermoë is ver vorentoe geposisineer. Hierdie eienskappe verbeter haar vermoë om ys te breek, maar dit kan lei tot 'n skerp toename in oop water weerstand en ander seewaardigheidsimplikasies, bv. branderimpak by die lepelvormige boeg en verlengde agterskip.

Rowwe seetoestande induseer beduidende rigiede ligaamsbeweging, wat lei tot 'n toename in weerstand en brandstofverbuik. Om bedryfsdoeltreffendheid op see te verseker, is dit van uiterste belang vir vaartuigeienaars om kennis te dra oor die gedrag van 'n skip in hierdie omgewings. Daarom is 'n ondersoek onderneem om die seewaardigheid van die SA Agulhas II te evalueer.

Volskaal metings is aan boord die skip uitgevoer tydens 'n vaart in die Suidelike Oseaan. Data verkry uit hierdie veldtog is gebruik om die dein-, rol- en stampbewegingsreaksies in onreëlmatige golwe te bepaal. Strookteorie is geïmplementeer om die bewegings-respons-amplitude-operateurs van die vaartuig te bepaal. Deur superposisie van die respons-amplitude-operateurs en die golfspektrum is die bewegingsreaksies in onreëlmatige golwe voorspel. 'n Vergelyking tussen gemete en voorspelde bewegings het getoon dat dein-en stampbeweging met redelike akkuraatheid voorspel kan word. Rolbeweging het verskillende afwykings getoon en toekomstige navorsing word aanbeveel om nie-lineêre effekte, soos roldemping, te bestudeer.

Numeriese vloeidinamika is geïdentifiseer as 'n noodsaaklike hulpmiddel om haar bewegingsreaksies en weerstand in kopgolwe te ondersoek. Tydens hierdie werk is drie snelhede geëvalueer, haar ontwerpspoed van 14 kn, 'n verlaagde spoed van 10 kn, en 'n verhoogde spoed van 18 kn. Oor die algemeen het die resultate getoon dat die maksimum dein- en stampbewegings na verwagting sal plaasvind wanneer die golfaantreffingsfrekwensie wissel tussen $0.124 - 0.143$ Hz. Vir al drie snelhede is die maksimum toegevoegde weerstand in golwe waargeneem wanneer groot amplitude beweging plaasvind. Daar is verder aangetoon dat 'n verlaging in spoed vanaf 14 kn tot 10 kn haar effektiewe drywing met 42 % kan verlaag. Verder is daar gevind dat, indien sy haar spoed verhoog met 4 kn vanaf 14 kn tot 18 kn kan dit lei tot 'n toename in effektiewe drywing van 87 %. Numeriese ondersoeke het verder getoon dat daar branderimpak kan plaasvind by die boeg van die SA Agulhas II, alhoewel sy nie in uiterste golftoestande vaar nie. Numeriese vloeidinamika toon duidelik potensiaal vir die bestudering van branderimpak by die boeg en agterskip van die SA Agulhas II.

Acknowledgements

I would like to express gratitude to the following people, who have generously offered up their time and knowledge to support this study.

Firstly, to my supervisor Prof Annie Bekker, thank you for your patience, invaluable guidance and vision throughout this study. Also, thank you for providing many learning opportunities throughout my postgraduate studies. Every meeting and discussion provided enthusiasm and kept the journey interesting and exciting. I would like to thank my co-supervisor, Prof Meyer, for providing excellent leadership and advice throughout this work. Since my undergraduate studies you have inspired me to gain further knowledge in fluid dynamics. I have enjoyed our meetings that involved discussions about aircraft, tanks and many other stories. To the support team at NUMECA International, thank you for providing assistance whenever it was required. I would like to extend thanks to the Department of Environment, Forestry and Fisheries, for providing information about their vessel. It has been an incredible privilege to form part of the SVRG. I have gained invaluable insight from each member throughout this project. Finally, to my family, thank you for kindling the spirit of adventure in me, and for selflessly offering up your time and finances to support me.

Dedications

This thesis is dedicated to my mom Lizette, dad Lauwerence and sister Tania for your unyielding support and encouragement.

Table of Contents

List of Figures

List of Tables

Nomenclature

Constants

g	$9.81\,\mathrm{m/s^2}$
j	$\sqrt{-1}$

Variables

A_3	Heave motion amplitude	[m/m]
A_5	Pitch motion amplitude	[deg /m]
γ_3	Heave phase	[deg]
γ_5	Pitch phase	[deg]
C_T	Total resistance coefficient	[−]
C_{aw}	Added wave resistance coefficient	[−]
f	Frequency	[Hz]
f_{n3}	Heave natural frequency	[Hz]
f_{n4}	Roll natural frequency	[Hz]
f_{n5}	Pitch natural frequency	[Hz]
Fn	Froude number	[ ]
F_x	Drag force	[N]
H	Wave height	[m]
k	Wave number	[$\mathrm{m^{-1}}$]
Re	Reynolds number	[ ]
S	Wetted surface area	[$\mathrm{m^2}$]
$S_{\zeta\zeta}$	Wave spectrum	[$\mathrm{m^2/Hz}$]
$S_{\xi\xi}$	Response spectrum	[$\mathrm{m^2/Hz}$]
T	Period	[s]
U	Ship speed	[m/s]
p	Pressure	[Pa]

Greek symobols

β	Flare angle
γ	Phase
ζ	Wave elevation
η	Mean wave direction
λ	Wavelength
μ	Dynamic Viscosity
ρ	Density
ϑ	Stem angle
φ	Unsteady time series
Φ	Potential function
χ	Wave encounter angle
ω	Circular frequency

Vectors and matrices

$\boldsymbol{a}$	Acceleration vector
$\boldsymbol{\alpha}$	Angular acceleration
$\boldsymbol{A}$	Added mass matrix
$\boldsymbol{B}$	Damping matrix
$\boldsymbol{C}$	Hydrostatic stiffness matrix
$\boldsymbol{\Theta}$	Euler angles
$\boldsymbol{F}$	State transition matrix
$\boldsymbol{\xi}$	Motion displacements
$\boldsymbol{K}_k$	Kalman gain
$\boldsymbol{M}$	Mass matrix
$\boldsymbol{P}_k$	Error covariance matrix
$\boldsymbol{q}$	Unit quaternions
$\boldsymbol{Q}$	System noise covariance matrix
$\boldsymbol{R}$	Measurement noise covariance matrix
$\boldsymbol{T}_\omega$	Quaternion transformation matrix
$\boldsymbol{v}$	Velocity vector
$\boldsymbol{x}_k$	State vector
$\boldsymbol{z}_k$	Measurement vector
$\boldsymbol{\omega}$	Angular velocity

Subscripts

e	Encounter

m	Mean
p	Peak
s	Significant
w	Wave
z	Zero-crossing

Abbreviations

BRICS Blended Reconstructed Interface Capturing Scheme
CFD Computational Fluid Dynamics
CFL Courant-Friedrichs-Lewy Fluid Dynamics
COG Centre of Gravity
DOF Degrees of freedom
DNS Direct Numerical Simulation
ECMWF European Centre for Medium-Range Weather Forecasts
EEOI Energy Efficiency Operational Index
DEFF Department of Environment, Forestry and Fisheries
DC Direct current
DP Dynamic positioning
EFD Experimental Fluid Dynamics
FVM Finite Volume Method
IMO International Maritime Organization
IMU Inertial Measurement Unit
IoT Internet of Things
IIR Infinite Impulse Response of Things
ITTC International Towing Tank Conference
MIZ Marginal Ice Zone
PDSTRIP Public Domain Strip Method
PSD Power Spectral Density
RANS Reynolds Averaged Navier-Stokes
RAO Response Amplitude Operator
SAM Six Accelerometer Method
SANAP South African National Antarctic Programme
SCALE Southern Ocean Seasonal Experiment
SDS Scientific Data System
SST Shear Stress Transport Data System
SVRG Sound and Vibration Research Group
SCADAS Supervisory Control and Data Acquisition Systems
V&V Verification and Validation

Chapter 1

Introduction

1.1 Background and motivation

The Southern Ocean is known for its extreme swells and turbulent waters (McCann, 2019). Nevertheless, regular research is conducted in this vast area of open ocean and Antarctica. South Africa has an advantageous geographical position and serves as a springboard for both African and global scientific research interests (Skelton, 2014). The South African National Antarctic Programme (SANAP) conducts annual research and logistical expeditions to Antarctica, Marion and Gough Island (Antarctic Legacy of South Africa, 2020). These expeditions are facilitated by the SA Agulhas II, a polar supply and research vessel (PSRV) owned by the Department of Environment, Forestry and Fisheries (DEFF), seen in Figure 1.1.

Figure 1.1: The SA Agulhas II. Photo courtesy of Alexander Oelofse.

The SA Agulhas II is the first vessel in her class built in compliance with SOLAS 2009 Passenger Ship Rules (Bekker, 2017). Therefore, a full-scale measurement campaign was initiated onboard the vessel in 2012 (Suominen *et al.*, 2013). To date, this campaign has been maintained by the Sound and Vibration Research Group (SVRG) at Stellenbosch University. This campaign aims to contribute to the scientific basis for the design of ice-going vessels by gaining insight into the relationship between wave- and ice-induced structural loads and vibration (Bekker, 2017). More recently, the research aim of the SVRG has shifted towards the development of decision support systems which will provide operational insight for navigational officers and stakeholders (Bekker, 2018).

During her annual expeditions, the SA Agulhas II must make long open ocean transits to and from her home port in Cape Town. For example, a relief voyage from Cape Town to Marion Island covers a distance of 1176 nm; from Cape Town to Gough Island she travels 1404 nm; and from Cape Town to the SANAP station in Antarctica she covers a distance of 2311 nm (Antarctic Legacy of South Africa, 2020). It is estimated that long open water transits account for up to 85 % of the total distance travelled during these expeditions.

To ensure safe and efficient operations, it is paramount for ship owners and designers to understand the seakeeping behaviour of a vessel (Castiglione *et al.*, 2011). In rough sea conditions, significant motions are induced on a vessel, which consequently increases the ship's resistance. This leads to increased fuel consumption and compromises the propulsive efficiency (Tezdogan *et al.*, 2015). The estimated operational cost per day at sea for the SA Agulhas II is approximately 400 000 ZAR (Devanunthan, 2019). Typically, for passenger ships, conventional cargo carriers and container vessels 30-54% of the total operating cost is dedicated to fuel cost (Bergqvist *et al.*, 2015). For larger container vessels, it may constitute more than 75 % (Ronen, 2011). In addition to economic concerns, intense pressure has been placed on the shipping industry to reduce its carbon footprint (Bialystocki and Konovessis, 2016). In 2009, the International Maritime Organization (IMO) introduced the Energy Efficiency Operational Index (EEOI) to monitor the operational performance of ships. The EEOI enables the assessment of ships based on their operational energy efficiency, which is expressed in terms of CO_2 per unit transport work (IMO, 2009).

In order to improve a ship's fuel efficiency, operational measures are implemented (Bialystocki and Konovessis, 2016). Speed reduction, more commonly termed slow steaming, has become a customary practise in the shipping industry (Maersk, n.d.). Reducing operating speed by 20 % could reduce daily consumption of fuel by 50 % (Ronen, 2011). However, this leads to an increase in transit time which increases time-related operating costs such as labour and inventory carrying costs (Durandt, 2020; Ronen, 2011). Also, since the SA Agulhas II partakes in scientific operations in the Southern Ocean, she regularly operates on a tight schedule, which occasionally requires her to operate at

maximum speed.

In addition to a ship's operational efficiency, wave-induced motion, loads and accelerations affect the well-being and safety of passengers and crew onboard a vessel at sea (Tezdogan *et al.*, 2014). Extreme wave conditions may lead to motion sickness and discomfort. Furthermore, operational tasks will take longer than they do in calm seas (Lloyd *et al.*, 1991).

1.2 Ship seakeeping

Seakeeping, in its broadest sense, can be defined as the performance of a ship in waves (Lloyd *et al.*, 1991). This includes aspects such as ship motion response, wave added resistance, slamming, human comfort, loss of speed and power output (Jiao *et al.*, 2017). Tools used to evaluate the seakeeping behaviour of ships include: model-scale tests, computations in the frequency and time domain and full-scale measurements at sea (Bertram, 2012).

Model-scale tests are primarily done during the design phase of ships to supply validation data for computational methods (Bertram, 2012). Usually, ship models are designed, built and tested in a controlled towing tank environment (ITTC, 2017*a*). These sgip models are also used to investigate non-linear seakeeping problems, e.g. roll motion, slamming and green water on deck (Bertram, 2012).

Frequency-domain methods are used to compute a ship's response amplitude operators (RAOs) over a range of wave lengths and directions (Bertram, 2012). These methods solve the equations of motion of a ship in the frequency domain, which is an analogy of a mass-spring-damper system with forced excitation (Journée and Massie, 2001). RAOs are defined as transfer functions describing the linear responses of a ship to harmonic waves. The standard frequency domain tool is strip theory or panel methods, which are based on potential flow theory (Bertram, 2012). These methods usually do not account for non-linear effects, such as viscosity and breaking waves (Simonsen *et al.*, 2013). However, they are still considered to be sufficiently accurate at lower computational costs (Castiglione *et al.*, 2011).

As accessibility to High Performance Computing (HPC) is increased and numerical schemes are improved, Computational Fluid Dynamics (CFD) techniques are becoming a promising tool used to investigate the seakeeping of ships (Kim, 2013). Full-scale CFD simulations are of particular interest since it can be used to investigate a vessel at or close to real loading conditions. Moreover, it can be used to determine the optimal operating conditions, such as speed and trim (Niklas and Pruszko, 2019). Furthermore, since CFD takes into account viscous effects, it is known to be more accurate than frequency domain methods at predicting motion responses, added resistance due to waves and other non-linear phenomena such as slamming (Tezdogan *et al.*, 2015; Oberhagemann *et al.*, 2010).

The final tool to investigate seakeeping is full-scale measurements of: ship motion responses, global and local loads, speed over ground, propeller speed and torque (Bertram, 2012). Measured responses at full-scale give invaluable insight into the behaviour of vessels in various realistic environments (Montazeri, 2016). One drawback of full-scale measurements is the difficulty of recording the seaway (Bertram, 2012). Therefore, considerable effort has been made to estimate the sea state from measured motion responses (Nielsen *et al.*, 2018).

1.3 Research aim

The aim of this study is to investigate the seakeeping behaviour of the SA Agulhas II. According to Lloyd *et al.* (1991), the ultimate goal of research in seakeeping is, or should be, to develop ship performance prediction techniques. This conforms to the larger vision of the SVRG, which involves the development of decision support systems for the SA Agulhas II (Bekker, 2018).

With particular regard to seakeeping, this study aims at investigating the motion responses of the vessel in a realistic environment, the added resistance in waves and the effect of operating speeds on the effective power. To this end, the objectives of this study have been defined as follows:

1. Conduct full-scale measurements onboard the SA Agulhas II during a cruise in the Southern Ocean to acquire data which can be used to determine the heave, roll and pitch motion in irregular waves. Furthermore, acquire information about the geometry and operational loading conditions of the vessel, as well as wave parameters from weather forecasts.

2. Calculate the ship's RAOs using strip theory and predict the heave, roll and pitch motion responses of the vessel in irregular waves. Evaluate the predicted motion responses by comparing it with measured motion responses.

3. Perform CFD simulations in wave conditions where large amplitude motions are expected. The following simulations will be performed in a stepwise manner:

   (a) Calm water simulations.

   (b) Simulation in head seas.

   (c) Compare results obtained from (a) and (b) to estimate the added resistance due to waves.

   (d) Evaluate the change in effective power when operating at various speeds.

1.4 Thesis outline

The methodology adopted to investigate the seakeeping behaviour of the SA Agulhas II is shown in Figure 1.2.

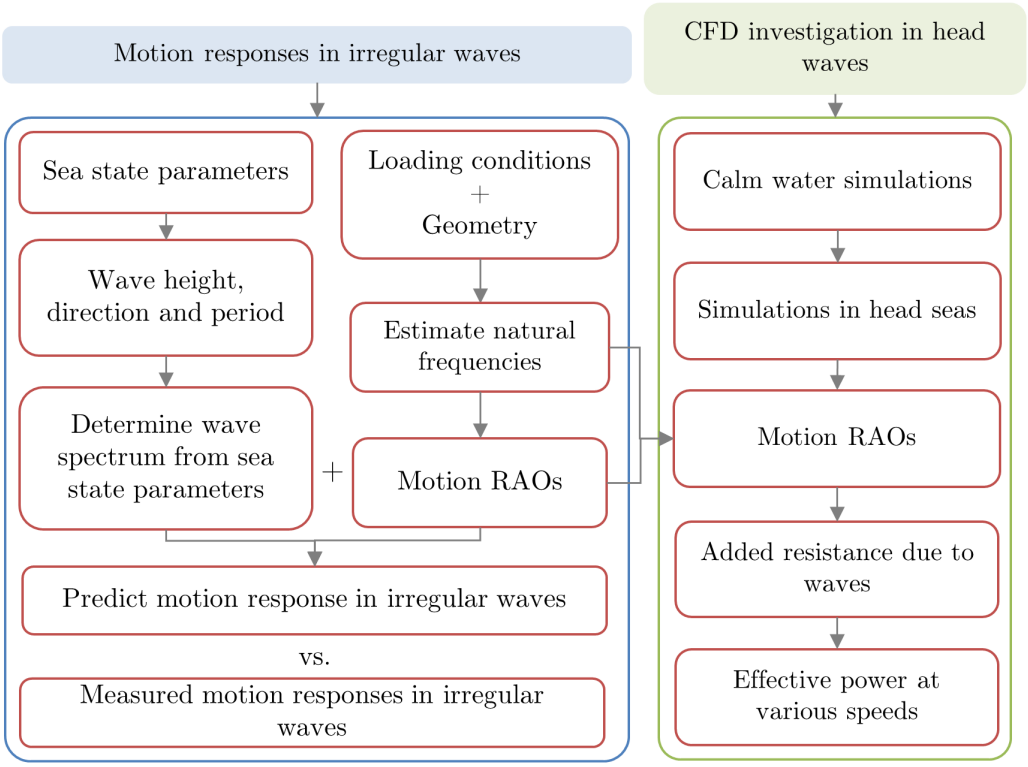

Figure 1.2: Methodology flow chart for the investigation of the seakeeping behaviour of the SA Agulhas II

This thesis is outlined as follows. Chapter 2 reviews literature on ocean waves, the dynamics of ships and methods used to address full-scale seakeeping problems. Chapter 3 discusses the vessel specifications and the description of full-scale measurements conducted during a cruise in the Southern Ocean. Chapter 4 presents full-scale measured responses and the prediction thereof using RAOs and the wave spectrum. In this chapter, the RAOs are calculated using the Public Domain Strip Method, PDSTRIP (Bertram *et al.*, 2006). Chapter 5 presents the CFD study using the software package FINE^{TM}/Marine, by NUMECA^{TM} International. Finally, the main findings are summarised in Chapter 6 and recommendations are made for future research.

Chapter 2

Literature review

2.1 Introduction

The aim of this study is to investigate the seakeeping behaviour of the SA Agulhas II, more specifically her motion response and added resistance due to waves. This chapter reviews important hydrodynamic concepts, ocean waves and ship dynamics. Furthermore, previous studies using similar approaches, i.e. full-scale measurements, strip theory and CFD, are reviewed.

2.2 Fundamental concepts of hydrodynamics

The study of ship hydrodynamics refers to the interaction of vessels with surrounding water (Birk, 2019). The purpose of this section is to discuss the governing equations which describe the fluid flow phenomena associated with waves and the motion of ships with reference to discussions in Fossen (2011) and Perez (2005). These equations lay the foundation for the formulations of waves, strip theory and CFD.

The governing equations of fluid dynamics considered are the continuity equation, which states that mass is conserved, and the conservation of momentum (i.e. Newton's second law) (Anderson, 1995).

The notations and terminologies used to describe the governing equations were adopted from Perez (2005). The derivation of these equations can be found in Versteeg and Malalasekera (2007), Bertram (2012) and Anderson (1995).

For the velocities involved in ship flows, water is regarded as an incompressible fluid, i.e. constant density ρ (Bertram, 2012). This leads to the continuity equation for incompressible flows:

$$\nabla \cdot \boldsymbol{v} = \frac{\partial u}{\partial x} + \frac{\partial v}{\partial y} + \frac{\partial w}{\partial z} = 0 \tag{2.1}$$

where $\boldsymbol{v} = [u\ v\ w]$ is the velocity vector.

The Navier-Stokes equations describe the conservation of momentum in the flow as follows:

$$\rho\left(\frac{\partial \boldsymbol{v}}{\partial t} + \boldsymbol{v}\cdot\nabla\boldsymbol{v}\right) = \rho\boldsymbol{F} - \nabla p + \mu\nabla^2\boldsymbol{v} \tag{2.2}$$

where $\boldsymbol{F} = [0 \;\; 0 \;\; -g]^T$ are accelerations due to volumetric forces, p is the pressure and μ is the viscosity coefficient of the fluid.

The continuity equation and the Navier-Stokes equations form a system of coupled, non-linear partial differential equations, which cannot be solved analytically. Due to the random fluctuations that are inherent to turbulent flows, Direct Numerical Simulation (DNS) is not yet feasible with the current computing power. An approximation consists of dividing the velocity vector and pressure, $\boldsymbol{v}$ and p, into a time-averaged part and a fluctuating part. This yields the Reynolds Averaged Navier-Stokes (RANS) equations, which can be solved numerically using CFD (Bertram, 2012). The RANS equations are discussed in more detail in Chapter 5.

Generally, viscosity is neglected in the study of ship hydrodynamics since it only plays a role in the boundary layer near the surface of a ship (Perez, 2005). Disregarding viscous forces in Equation 2.2 yields the Euler equation of fluid motion:

$$\rho\left(\frac{\partial \boldsymbol{v}}{\partial t} + \boldsymbol{v}\cdot\nabla\mathbf{v}\right) = \rho\boldsymbol{F} - \nabla p \tag{2.3}$$

Furthermore, the flow is assumed to be irrotational, i.e. $\nabla \times \boldsymbol{v} = 0$. The flow of irrotational and inviscid fluids are defined as potential flow. This assumption simplifies the mathematical treatment of the flow and introduces a scalar function called the potential function $\Phi(t, x, y, z)$ such that:

$$\boldsymbol{v} = \nabla\Phi \tag{2.4}$$

If the potential function is known the velocity components can be calculated as follows:

$$u = \frac{\partial\Phi}{\partial x}, \;\; v = \frac{\partial\Phi}{\partial y}, \;\; w = \frac{\partial\Phi}{\partial z} \tag{2.5}$$

A velocity potential function that satisfies the continuity equation regresses to the Laplace equation of the potential function:

$$\nabla^2\Phi = \frac{\partial^2\Phi}{\partial x^2} + \frac{\partial^2\Phi}{\partial y^2} + \frac{\partial^2\Phi}{\partial z^2} = 0 \tag{2.6}$$

The potential function can be determined by solving the Laplace equation subject to specified boundary conditions. The pressure of the fluid can be determined by integrating the Euler equation, Equation 2.3, which yields the Bernoulli equation:

$$p - p_0 = -\rho g z - \rho \frac{\partial \Phi}{\partial t} - \frac{1}{2}\rho \left(\nabla \Phi\right)^2 \tag{2.7}$$

where p_0 is the atmospheric pressure.

To summarize, the fluid velocity vector is described as the gradient of a potential, which does not have any physical meaning. The Laplace equation is used to solve the potential subject to the appropriate boundary conditions at the free surface, sea floor and ship's hull. Consequently, the velocities are solved and then the pressure is calculated using the Bernoulli's equation. Thereafter, the pressure is integrated over the wetted surface of the hull to determine the forces acting upon it (Fossen, 2011).

Potential flow theory is the basis of most hydrodynamic software, including PDSTRIP (Bertram *et al.*, 2006), and can be used to obtain sufficiently accurate results to most problems such as ship motion in waves (Perez, 2005). More complicated, non-linear problems such as propeller-rudder-hull interactions, slamming and manoeuvring are better solved when the effects of viscosity are accounted for (Bertram, 2012).

2.3 Ocean waves

Ocean waves are defined as vertical motions that travel across the surface of the ocean. Waves are generated by forces acting upon the water surface, e.g. from local wind, seismic oscillations during earthquakes and gravitational attraction between the Earth, Sun and Moon (Holthuijsen, 2007). This results in a variety of waves which are characterized by their wave length and associated period. A ship travelling in waves is primarily influenced by gravity waves, i.e. wind and swell waves. Gravity waves are characterised by a period of approximately 1 s and 25 s with wave lengths varying between about $1.5 - 900$ m (Toffoli and Bitner-Gregersen, 2017)

Wind waves typically occur in a developing sea, or storm, when the ocean surface is excited by local wind. These generally occur at high frequency ranges (i.e. they have lower wave periods). After wind waves leave the area where they are generated, they take on a long, regular crested appearance. The sea is then classified as a fully developed sea. The long regular waves are known as swell waves, which occur at low frequency ranges (Skandali, 2015; Fossen, 2011).

2.3.1 Regular waves in deep water

Regular waves or airy waves, are defined as periodic, unidirectional advancing wave trains with a single basic harmonic. The surface elevation $\zeta(x,t)$ is characterised by a sinusoidal profile with a constant amplitude, $\bar{\zeta}$, as follows (Perez, 2005):

$$\zeta(x,t) = \bar{\zeta}\sin(\omega t - kx + \gamma) \tag{2.8}$$

where ω is the circular wave frequency, k is the wave number and γ is the initial phase. The wave height is double the amplitude and is given by $H_w = 2\bar{\zeta}$. Regular waves are characterised by a length and time parameter. The length parameter is the wave length, λ, or wave number, k. The time parameter is the circular wave frequency, ω, or the wave period, T_w. k and ω is defined as follows (Bertram, 2012):

$$k = \frac{2\pi}{\lambda}; \quad \omega = \frac{2\pi}{T_w} \tag{2.9}$$

This study only considers deep water conditions. This implies that the water's depth, D, is greater than half the wave length, i.e. $D \geq \lambda/2$ (Perez, 2005). For deep water conditions the dispersion relation relates the wave number, k, to the wave frequency, ω, as follows (Lewandowski, 2004):

$$k = \frac{\omega^2}{g} \tag{2.10}$$

For ship seakeeping, the assumption is made that waves are dominated by gravity effects. Surface tension, water compressibility and viscosity are neglected (Bertram, 2012). Therefore, potential flow theory can be used to formulate the mathematical description of the fluid flow velocities and pressure distribution of a travelling wave (Perez, 2005).

The potential function of a travelling wave is denoted by Φ_w. As discussed in the previous section, the assumption is made that the Laplace equation is satisfied, i.e. $\nabla^2\Phi_w = 0$. By solving the Laplace equation, the velocity of the fluid is given by $\nabla\Phi_w$. Finally, the Bernoulli equation can be used to calculate the pressure in the fluid (Perez, 2005). The potential function of a travelling wave is subject to the following boundary conditions:

1. The kinematic free surface boundary condition assumes that fluid particles on the free surface remain on the free surface.

2. The dynamic free-surface condition makes the assumption that the water pressure on the free surface is equal to the atmospheric pressure.

3. The sea bed condition which determines that the flow velocity component normal to the sea bottom is zero.

For more information about the mathematical formulations of these boundary conditions, see discussions presented in Faltinsen (1990) and Perez (2005).

Under the boundary conditions discussed above, the velocity potential function of a wave propagating in the positive x-direction is expressed as follows (Perez, 2005):

$$\Phi_w = \frac{g\bar{\zeta}}{\omega} e^{kz} \cos(\omega t - kx + \gamma) \tag{2.11}$$

The wave descriptions discussed above form part of first-order Stokes wave theory. Higher-order Stokes waves account for non-linearities related to the wave amplitude. They have, for example, broader troughs and steeper crests (Bertram, 2012). Therefore, they resemble a real wave more accurately (Tezdogan *et al.*, 2015). For more theoretical detail on higher order waves, reference is made to discussions in Holthuijsen (2007).

2.3.2 Irregular seas and the wave spectrum

A combination of swell and wind waves of different amplitudes, periods, directions and phases can exist in the ocean. The resulting chaotic wave field is known as irregular seas (Skandali, 2015). Irregular seas are random in space and time, therefore the surface elevation of the sea is described by a wave spectrum, $S_{\zeta\zeta}(\omega)$. The wave spectrum is a Power Spectral Density (PSD) that describes the energy distribution of the free surface in the frequency domain (Perez, 2005). The theoretical derivation of the wave spectrum discussed below was obtained from discussions in Faltinsen (1990), Journée and Massie (2001) and Bertram (2012).

The expression of the wave spectrum starts by superimposing the harmonic wave components of irregular seas:

$$\zeta = \sum_{j=1}^{N} \bar{\zeta}_j \sin(\omega_j t - k_j x + \gamma_j) \tag{2.12}$$

Each harmonic wave component denoted by j, has its own amplitude and phase in the frequency domain. The wave spectrum can then be obtained as follows:

$$S_{\zeta\zeta}(\omega_j)\Delta\omega = \sum_{j=1}^{N} \frac{1}{2}\bar{\zeta}_j^2 \tag{2.13}$$

where $\Delta\omega$ is the difference between successive frequencies. A graphical interpretation of a wave spectrum and how it relates to the time domain can be seen in Figure 2.4.

It is noteworthy to mention that the description of the wave spectrum, and later the motion response spectra, are given as a function of circular frequency ω (in rad/s), following the methods presented in Perez (2005). However, in this study the spectra will be given as a function of frequency, f (in Hz). The axis transformation from ω to f is as follows:

$$f = \frac{\omega}{2\pi} \quad \text{and} \quad S_{\zeta\zeta}(f) = 2\pi S_{\zeta\zeta}(\omega) \tag{2.14}$$

2.3.3 Parametric description of the wave spectrum

The wave spectrum can calculated through wave ride buoys that measure surface elevation of the sea (Bertram, 2012). An example of this can be found in Ha and Gourlay (2018). If no data from wave-buoys are available, the wave spectrum can be described using standard, idealized formulae (Perez, 2005). These are theoretical formulations which describe the average shape of the PSD when the sea state parameters are known (Montazeri, 2016). The sea state parameters of interest include the significant wave height, H_s, and the peak period, T_p. H_s is defined as the average value of a the third of the highest waves. This means that 33 % of the largest waves were selected and averaged to determine H_s (Ramberg, 2017). T_p is related to the peak frequency of the spectrum, ω_p, through $T_p = 2\pi/\omega_p$.

Various idealized wave spectra have been developed since the 1950s and are presented in literature (Perez, 2005; Journée and Massie, 2001). The choice of wave spectrum depends on the type sea state, i.e. developing or fully-developed (Fossen, 2011). In order to predict the motion responses of vessels in the open ocean the International Towing Tank Conference (ITTC) recommend using the ITTC wave spectrum (ITTC, 2014*b*). This spectrum can be parametrized in terms of H_s and T_p as follows (Perez, 2005):

$$S_{\zeta\zeta}(\omega) = \frac{173 H_s^2}{(0.710 T_p)^4 \omega^5} \exp\left(\frac{-691}{\omega^4 (0.710 T_p)^4}\right) \tag{2.15}$$

An illustration of the ITTC wave spectrum at various significant wave heights and peak periods is given in Figures 2.1a and 2.1b.

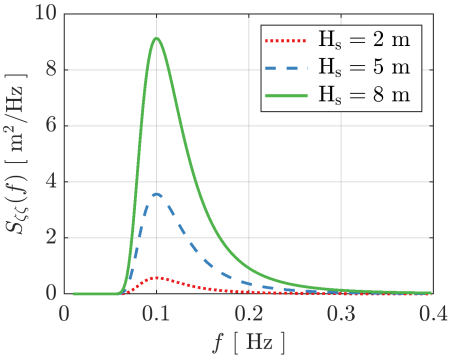

(a) Varying H_s with $T_p = 10s$

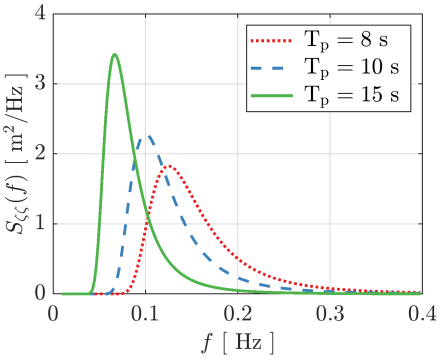

(b) Varying T_p with $H_s = 4m$

Figure 2.1: An example of the ITTC wave spectrum with various H_s and T_p.

2.3.4 Encounter frequency and encounter spectrum

The motion of a ship in waves is its response to the forces and moments due to a varying pressure distribution on the surface of the hull caused by waves. The motion and force responses are not only influenced by the wave amplitude and frequency, but also the ship speed and the encounter angle (Perez, 2005). Figure 2.2 shows a ship is advancing in waves at a speed, U, and experiencing waves at an encounter angle, χ. The encounter angle, χ, is defined as the angle of the wave relative to the heading of the ship and is used to describe the sailing conditions, e.g. head seas and beam seas (Perez, 2005).

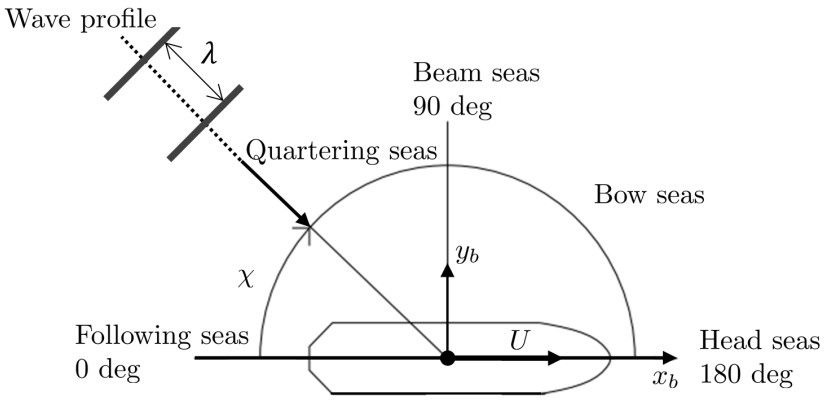

Figure 2.2: Definition of encounter angle (Perez, 2005). Figure adapted from Perez and Blanke (2002).

The frequency at which waves excite the ship is called the circular encounter frequency, ω_e, and is calculated as follows (Bertram, 2012):

$$\omega_e = \left| \omega - \frac{\omega^2 U}{g} \cos(\chi) \right| \tag{2.16}$$

The change in encounter frequency, which is known as the Doppler effect, also influences the wave spectrum experienced by the ship. This is called the wave encounter spectrum $S_{\zeta\zeta}(\omega_e)$ and is calculated through Equation 2.17 (Bertram, 2012).

$$S_{\zeta\zeta}(\omega_e) = \frac{S_{\zeta\zeta}(\omega)}{\left| \frac{d\omega}{d\omega_e} \right|} = \frac{S_{\zeta\zeta}(\omega)}{\left| 1 - \frac{2\omega U}{g} cos(\chi) \right|} \tag{2.17}$$

2.4 Ship dynamics

The dynamics of ship motion is divided into two main areas: kinematics and kinetics. The former describes the geometrical concepts of ship motion, while

the latter describes the forces and moments which induce ship motion (Schoop-Zipfel, 2016). In this study, a ship is defined as a rigid body, meaning it is "composed of a continuous distribution of particles having mutual distances that are inextensible" (Lewandowski, 2004).

This section discusses the dynamics of a ship in regular waves with reference to discussions in Perez (2005), Faltinsen (1990) and (Bertram, 2012). In addition, the determination of the responses of a ship in irregular seas is discussed in Section 2.4.4.

2.4.1 Ship motion

A ship travelling at sea moves in six degrees of freedom (DOF). The six motion components are: surge, sway heave, roll, pitch and yaw, see Figure 2.3.

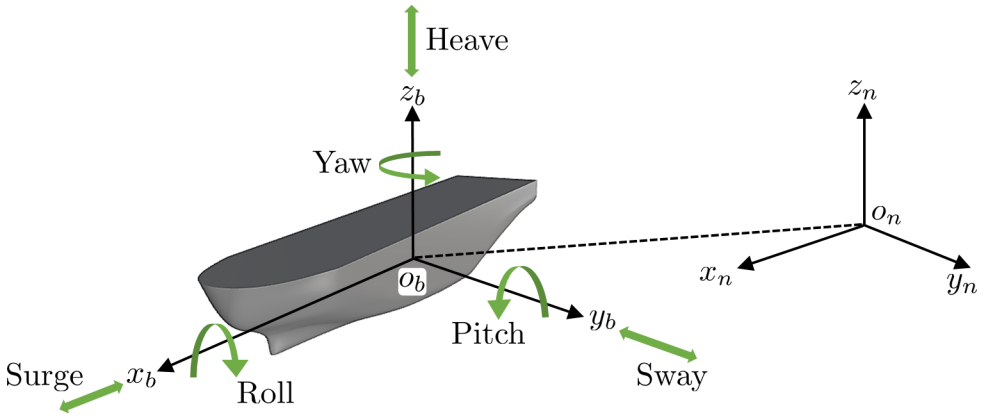

Figure 2.3: Coordinates used to define the 6 DOF motion.

In seakeeping theory, the following vector is used to the describe the motion of a ship (Perez, 2005):

$$\boldsymbol{\xi} = \begin{bmatrix} \xi_1 & \xi_2 & \xi_3 & \xi_4 & \xi_5 & \xi_6 \end{bmatrix}^T \tag{2.18}$$

where ξ_1, ξ_2, ξ_3 are the surge, sway and heave displacements, respectively. ξ_4, ξ_5, ξ_6 are the roll, pitch and yaw displacement angles. These are defined as Euler angles, $\boldsymbol{\Theta}$, which describe the orientation of a body with respect to a fixed reference frame (Lewandowski, 2004). For this reason, two orthogonal reference frames are defined, as shown in Figure 2.3. The body-fixed frame, b-frame, is fixed in relation to the average position of the ship and moves with the same speed. The positive z_b-axis points upwards through the centre of gravity (COG), while the origin of the x_b-y_b plane coincides with the undisturbed free surface (Faltinsen, 1990). The inertial reference frame, n-frame, is described by the North-West-Up reference frame, i.e. the x_n-axis is directed North, the y_n-axis is points West and the z_n-axis upwards normal to the earth's surface (Bieda and Jaskot, 2016).

In Appendix A, a further discussion of Euler angles and the transformation between the body-fixed and the earth-fixed reference frame is given. A discussion of unit quaternions is also presented. Unit quaternions are an alternative four parameter method used to represent the orientation of a body (Greenwood, 2003). The unit quaternions will be used to determine the orientation of the vessel from onboard acceleration and angular velocity measurements. This will be discussed in more detail in Chapter 4.

2.4.2 The equations of motion

The equations of motion for a ship are derived from Newton's second law and are given as follows (Perez, 2005):

$$\boldsymbol{M}\ddot{\boldsymbol{\xi}} = \boldsymbol{\tau}_w + \boldsymbol{\tau}_r + \boldsymbol{\tau}_v + \boldsymbol{\tau}_{hs} \tag{2.19}$$

where $\boldsymbol{M}$ refers to the mass matrix.

In Equation 2.19, $\boldsymbol{\tau}_w$, are wave-excitation forces, which can be decomposed into the Froude-Krylov and diffraction forces. The Froude-Krolov forces are forces due to the distribution of the pressure field in the undisturbed incident wave (Perez, 2005). The diffraction forces are contributions due to the disturbance of the wave by the ship (Bertram, 2012). The wave-excitation forces of regular waves can be expressed as follows (Faltinsen, 1990):

$$\boldsymbol{\tau_w} = \tilde{\boldsymbol{\tau}}_{\boldsymbol{w}} e^{-i\omega_e t} \tag{2.20}$$

where $\tilde{\boldsymbol{\tau}}_{\boldsymbol{w}}$ denotes the complex amplitude of the wave excitation force.

$\boldsymbol{\tau}_r$ are known as radiation forces. These forces occur when waves are radiated from a ship due to its oscillatory motion (Schoop-Zipfel, 2016) and take the form:

$$\boldsymbol{\tau}_r = -\boldsymbol{A}\ddot{\boldsymbol{\xi}} - \boldsymbol{B}\dot{\boldsymbol{\xi}} \tag{2.21}$$

where $\boldsymbol{A}$ is the added mass matrix and $\boldsymbol{B}$ is the damping matrix.

Viscous forces, $\boldsymbol{\tau}_v$, are non-linear frictional forces acting upon the surface of a submerged hull moving through water. Viscous forces give rise to flow separation, vortices and damping which removes energy from a body (de Jong, 2005). As mentioned before, potential theory neglects the effect of viscosity. This could pose some challenges, since in some cases, e.g. for resonant roll motion, the effects of viscosity are important (DNVGL, 2018).

Finally, the hydrostatic forces and moments, $\boldsymbol{\tau}_{hs}$, are defined as the restoring gravitational and buoyancy forces that tend to bring the ship to an upright equilibrium (Perez, 2005). These forces and moments can be written as follows:

$$\boldsymbol{\tau}_{hs} = -\boldsymbol{C}\boldsymbol{\xi} \tag{2.22}$$

where $\boldsymbol{C}$ is called the hydrostatic stiffness matrix.

By substituting the aforementioned components, except for the viscous force components, into Equation 2.19 it follows that the equations of motion can be expanded as follows (Faltinsen, 1990):

$$(\boldsymbol{M}+\boldsymbol{A})\ddot{\boldsymbol{\xi}}+\boldsymbol{B}\dot{\boldsymbol{\xi}}+\boldsymbol{C}\boldsymbol{\xi}=\boldsymbol{\tau_w}. \tag{2.23}$$

This study is only concerned with the heave, roll and pitch motions. Heave and pitch motions are considered to be symmetric motions (Journée and Massie, 2001). On the other hand, roll is an asymmetric motion. This implies that the phase angles of the roll response will differ for waves entering from the starboard side and port side of a ship (Montazeri, 2016). Symmetric and asymmetric motions are uncoupled. For example, if a vertical force is applied at the COG of the vessel, it will cause heave and pitch motion, but will not result in roll motion (Journée and Massie, 2001). Therefore, the equations of motion for coupled heave and pitch motion are given as (Seif *et al.*, 2014):

$$(m+A_{33})\ddot{\xi}_3+\ B_{33}\dot{\xi}_3+\ C_{33}\xi_3+\ A_{35}\ddot{\xi}_5+\ B_{35}\dot{\xi}_5+\ C_{35}\xi_5=\ F_z \tag{2.24}$$

$$(I_{55}+A_{55})\ddot{\xi}_5+\ B_{55}\dot{\xi}_5+\ C_{55}\xi_5+\ A_{53}\ddot{\xi}_3+\ B_{53}\dot{\xi}_3+\ C_{53}\xi_3=\ M_y \tag{2.25}$$

The equation of motion for roll is (Bergdahl, 2008):

$$(I_{44}+A_{44})\ddot{\xi}_4+B_{44}\dot{\xi}_4+C_{44}\xi_4=M_x \tag{2.26}$$

In Equations 2.24−2.26, m is the the mass of the ship and I_{jk} are the moments of inertia and A_{jk}, B_{jk} and C_{jk} are the coefficients of the added mass, damping and restoring forces. F_z, M_x and M_y are known as the heave excitation force, and roll and pitch excitation moments, respectively.

The equations of motions are usually solved numerically for a discrete set of wave frequencies to determine the RAOs of a vessel (de Carvalho Ribeiro Belga, 2017). In CFD, the temporal evolution of equations of motion are solved and take into account non-linear effects such as viscosity (Centrale Nantes, 2020*a*). Strip theory solves the equations of motion in the frequency domain (Bertram *et al.*, 2006).

2.4.3 Response amplitude operators

Transforming Equation 2.23 into the frequency domain yields the following expression (Perez, 2005):

$$-\omega_e^2(\boldsymbol{M}+\boldsymbol{A})\tilde{\boldsymbol{\xi}}+j\omega_e\boldsymbol{B}\tilde{\boldsymbol{\xi}}+\boldsymbol{C}\tilde{\boldsymbol{\xi}}=\tilde{\boldsymbol{\tau}}_{\boldsymbol{w}} \tag{2.27}$$

where $\tilde{\boldsymbol{\xi}}$ denotes the complex amplitude of the motion response, which can be calculated as follows:

$$\tilde{\boldsymbol{\xi}}=\frac{\tilde{\boldsymbol{\tau}}_{\boldsymbol{w}}}{[-\omega_e^2(\boldsymbol{M}+\boldsymbol{A})+j\omega_e\boldsymbol{B}+\boldsymbol{C}]} \tag{2.28}$$

The wave elevation at the origin of the b-frame can be given by (Perez, 2005):

$$\zeta(t) = \overline{\zeta}\cos(\omega_e t + \gamma) \tag{2.29}$$

Response amplitude operators (RAOs) are defined as the transfer functions that describe the ratio of the complex amplitude of the motion response to the complex amplitude of the wave amplitude, $\tilde{\zeta}$ (Journée and Massie, 2001). The RAOs, denoted by $H_i(\omega_e, \chi)$, can be calculated as follows (Perez, 2005):

$$H_i(\omega_e, \chi) = \frac{\tilde{\xi}_i(\omega_e, \chi)}{\tilde{\zeta}} \quad \text{for} \quad i = 1, 2, ...6. \tag{2.30}$$

The amplitude and phase, A_{ξ_i} and γ_{ξ_i}, of the complex RAO can be calculated through:

$$A_i = |H_i(\omega_e, \chi)|\,; \quad \gamma_i = \tan^{-1}\left(\frac{\mathrm{Im}[\tilde{\xi}_i]}{\mathrm{Re}[\tilde{\xi}_i]}\right) \tag{2.31}$$

The amplitude, A_i, is defined as the ratio of the amplitude of a response to amplitude of an incident wave, and the phase, γ_i, indicates the phase relationship between the response and wave (Montazeri, 2016).

2.4.4 Ship motion response in irregular seas

The motion response of a ship in irregular seas can be calculated based on principles of superposition between the RAOs and the wave spectrum (St. Denis and Pierson, 1953). The ship is defined as a 'black box', or filter, that receives waves as an input and outputs the ship motion. The black box is defined by the transfer functions discussed above (Lloyd *et al.*, 1991). It follows that the motion response spectra, $S_{\xi\xi_i}(\omega_e)$, is given by (Perez, 2005):

$$S_{\xi\xi_i}(\omega_e) = |H_i(\omega_e, \chi)|^2\, S_{\zeta\zeta}(\omega_e) \quad \text{for} \quad i = 1, 2, ...6. \tag{2.32}$$

A graphical illustration of the transformation between the wave spectrum and the motion response spectrum is shown in Figure 2.4. Furthermore, the motion response spectrum can be determined from onboard measurements using spectral analysis routines in MATLAB®, e.g. `pwelch.m` (Nielsen, 2005).
In theory, it is possible to apply similar principles to other responses, e.g. vertical bending moment at amidships, if the transfer functions are available (Nielsen *et al.*, 2018).

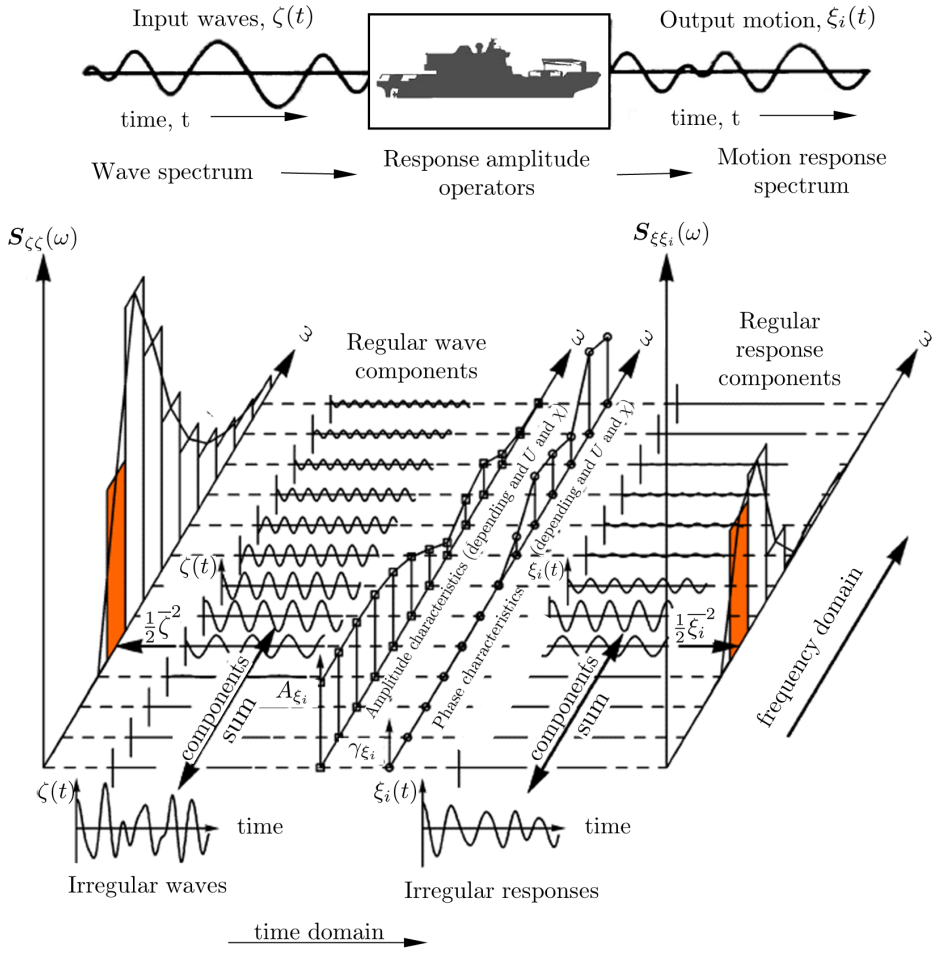

Figure 2.4: Principle of transferring wave spectrum to response spectrum, adapted from Journée and Massie (2001).

2.5 Full-scale measurements of ship motion

Full-scale measurements of ship motion responses are useful to gain insight into the behaviour of a ship in a realistic environment (Montazeri, 2016). For this work, measured motion responses are of interest to evaluate the prediction of it in irregular seas using hydrodynamic software. Generally speaking, heave, roll and pitch motions are included during when comparisons are made between measured and predicted motion responses (Ha and Gourlay, 2018). Heave and pitch motion responses are known to be predicted more reliably by hydrodynamic software, while roll motion is usually included due to its asymmetric characteristics, as discussed in Section 2.4.2. An example of this may be found in the work presented by Montazeri (2016), where roll was included to estimate the encounter direction of the sea state.

Commercial sensors available on the market output the DOF of interest, eliminating the requirement for extensive signal processing (Koning, n.d.).

However, these sensors tend to be expensive (Auestad *et al.*, 2013). Therefore, the Internet of Things (IoT) seek to develop low-cost measurement units which incorporate, Inertial Measurement Unit (IMU) sensors and micro- controllers, e.g. Raspberry Pi's (Abankwa *et al.*, 2015). These IMU sensors usually consist of accelerometers which measure acceleration; gyroscopes which measure angular velocity; and magnetometers which measure the Earth's magnetic field (Bieda and Jaskot, 2016; Fossen, 2011).

Luus (2019) designed and tested a measurement unit for use onboard the SA Agulhas II. This unit consisted of an Arduino microcontroller, IMU sensors and a barometer. Data obtained from the accelerometers and gyroscopes were combined in a Kalman filter algorithm to determine the roll and pitch motion of the ship. The heave motion was determined through a barometer, which measures atmospheric pressure.

Boulle (2016) presented an additional method, the Six Accelerometer Method (SAM), to determine the angular velocity of the SA Agulhas II. In addition, the SAM has also been utilized in studies presented by Haward *et al.* (2009) and Pisula *et al.* (2012) to investigate motion sickness onboard various ships. This method calculates the angular acceleration of a body from measured linear accelerations, based on well-known kinematic principles (Padgaonkar *et al.*, 1975). The angular acceleration can then integrated to determine the angular velocity of the body.

For this study, the SAM is chosen to calculate the angular velocity of the SA Agulhas II. Further elaboration on this method is given in Appendix B.

2.6 Strip theory

Strip theory is a linear frequency-domain method based on potential flow theory that is used to compute the motion RAOs in regular waves (Bertram, 2012). Three-dimensional problems are reduced to two-dimensional problems by dividing a ship's hull into a series of transverse slices, as shown in Figure 2.5. Each slice is then treated as a long floating cylinder (Journée and Massie, 2001). The assumption is made that the waves caused by the ship propagate in the transverse direction only. The hydrodynamics for each strip is computed and then integrated over the length of a ship to yield the three-dimensional solution (Schoop-Zipfel, 2016).

RAOs obtained from strip theory and other hydrodynamic software are often validated by comparing it with results obtained from towing tank experiments. A benchmark study was conducted by Gourlay *et al.* (2015) on three cargo model-scale ships. The heave and pitch RAOs were determined using a variety of hydrodynamic software codes. Overall, good agreement was found between the numerical predictions and the experimental data for head and beam seas at various forward speeds.

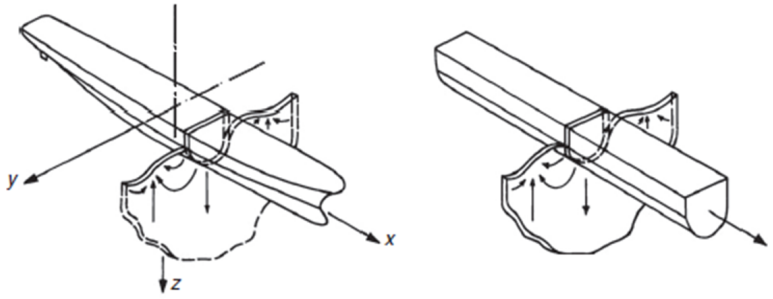

Figure 2.5: Principle of Strip theory (Bertram, 2012).

The motion response of a full-scale vessel in irregular seas can be predicted using RAOs obtained from strip theory. Ha and Gourlay (2018) conducted full-scale heave, roll and pitch measurements onboard container ships entering and leaving the Port of Fremantle in Western Australia. In-situ wave measurements were conducted by a wave-buoy from which the wave spectrum was determined for each transit. Strip theory was used to calculate the RAOs of the vessel, which was used to predict the motion response of the vessels. The heave and pitch response was predicted with reasonable accuracy. Some discrepancies were found between the predicted and measured roll motion due to factors such as roll damping. A similar study was conducted by Ntamba Ntamba *et al.* (2019) onboard the SA Agulhas II while she was on a cruise in the Southern Ocean in 2017. Wave parameters were obtained from weather forecasts. These parameters were used to calculate the wave spectrum, formulated by a Bretschneider spectrum. The predicted and measured responses for surge, heave and pitch were in fair agreement, but roll was over predicted.

Several studies have presented the use of RAOs and full-scale measured motion response to successfully predict the sea state in which a ship is travelling (Nielsen, 2005; Montazeri *et al.*, 2016).

2.7 Computational fluid dynamics

The use of strip theory to investigate seakeeping aspects of ships is limited since it does not take into account non-linear effects, e.g. breaking waves, turbulence or viscosity (Simonsen *et al.*, 2013). These limitations can be overcome by incorporating CFD methods, such as RANS equation solvers (Tezdogan *et al.*, 2015). The focus of CFD simulations has been placed on investigating the heave, pitch and resistance of ships travelling in calm water and in regular head waves, since these responses are fairly well predicted (Simonsen *et al.*, 2013).

Castiglione *et al.* (2011) investigated the heave, pitch and resistance of a high-speed catamaran in head waves by means of CFD and strip theory. The study showed that CFD predicts the motion response with higher accu-

racy. Similarly, Simonsen *et al.* (2013) investigated the resistance of the Kriso Container Ship (KCS). This evaluation was done through three methods: Experimental Fluid Dynamics (EFD) (i.e. towing tank experiments), CFD and potential flow theory. The results obtained using CFD showed better agreement with EFD compared to potential flow theory. Both studies presented by, Castiglione *et al.* (2011) and Simonsen *et al.* (2013), observed that the resistance increases close to resonance, i.e. when large amplitude motion responses occur.

The majority of CFD simulations have been performed at model-scale in order to validate it with EFD data. However, due to scale effects, e.g. the effect of the boundary layer, flow separation, vortex formation and wave breaking, discrepancies can exist between model-scale and full-scale CFD simulations (Hochkirch and Mallol, 2013). Therefore, Tezdogan *et al.* (2015) investigated the heave and pitch motion response and added wave resistance of the full-scale KCS in head waves. Two speeds were considered, the vessel's design speed and a slow steaming speed. Full-scale CFD simulations were in good agreement with model-scale EFD data presented by Simonsen *et al.* (2013). The investigation found that slow steaming can reduce the effective power by 52 %.

2.8 Conclusion

The literature review outlined the governing equations of hydrodynamic software used in investigating the seakeeping behaviour of ships in waves. Furthermore, background information has been provided on the means to investigate the seakeeping behaviour of full-scale ships.

A full-scale measurement campaign onboard the SA Agulhas II will provide valuable insight into the heave, roll and pitch motion responses in irregular seas. During this campaign, it is essential to acquire sea state parameters. Thereafter, using RAOs obtained from strip theory and the wave spectrum, the motion response in irregular seas can be predicted. In order to validate the predicted responses, they can be compared to measured responses.

The evaluation of added resistance in waves is a key issue in seakeeping studies. The maximum added resistance is expected to occur when the relative motion between the ship and the incident wave is high, i.e. close to the ship's natural heave and pitch frequencies (Castiglione *et al.*, 2011).

A CFD investigation will be undertaken to evaluate the heave and pitch response, as well as the added resistance of the SA Agulhas II in head waves. Her seakeeping performance will be evaluated at three speeds, her design speed of 14 kn, a reduced speed of 10 kn and a maximum speed of 18 kn.

Chapter 3

Full-scale measurements

Full-scale measurements were performed onboard the SA Agulhas II during the 2019 Southern Ocean Seasonal Experiment (SCALE) Winter Cruise. The aim of this campaign was to acquire data which can be used to determine the motion response of the vessel in irregular seas. This chapter presents the characteristics of the vessel and a description of the SCALE Winter Cruise. Furthermore, the measurement equipment, setup, consortium measurements and data processing are discussed.

3.1 The SA Agulhas II

The SA Agulhas II is a monohull ship which serves as a PSRV (DNV GL, 2012). She is built to Polar Class PC 5, hence she has the capability to operate for year-round operations in medium first year ice with a thickness of $0.7 - 1.2$ m, which may contain old ice inclusions (Omer and Bekker, 2018). Her propulsion system includes four 3 MW Wärtsilä 6L32 diesel generators which power two Conver Team electric motors. Each motor is connected via a shaft to a 4.5 m four-bladed variable pitch propeller. This propulsion system allows her to travel at a service speed of 14 kn and a maximum speed of 18 kn. At her service speed she has an operating range of approximately 15,000 nm (Lucas, 2012).

The main characteristics of the vessel are shown in Table 3.1. The values for the roll and pitch radii of gyration were chosen in accordance with suggestions by Fossen (2011) for offshore vessels. Additionally, the wetted surface area, waterplane area and the longitudinal metacentric height were obtained from the Domhydro plug-in included in the FINE^{TM}/Marine package. The metacentric height and the position of the centre of gravity were obtained from the loading conditions supplied by the vessel owner. All other parameters were acquired from DNV GL (2012).

Table 3.1: Main characteristics of the SA Agulhas II.

Details	Value	Units
Length overall, L_{OA}	134	m
Length of waterline, L_{WL}	126	m
Length between perpendiculars, L_{PP}	122	m
Beam at waterline, B_{WL}	22	m
Design draft, T_{WL}	7.65	m
Depth, D	10.6	m
Wetted surface area, S	3620	m^2
Waterplane area, A_{WP}	2455	m^2
Displacement, ∇	13687	m^3
Block coefficient, $C_B = \nabla/(L_{pp}B_{WL}T)$	0.67	
Longitudinal centre of gravity from the aft peak, LCG	57.9	m
Vertical centre of gravity from keel, KG	8.81	m
Metacentric height from keel, GM_t	2.36	m
Free surface metacentric height corrected, GM_f	1.63	m
Longitudinal metacentric height, GM_L	93.5	m
Roll radius of gyration, k_{44}	$0.37B$	m
Pitch radius of gyration, k_{55}	$0.25L_{pp}$	m

3.1.1 Hull geometry

The lines plan drawing of the SA Agulhas II, shown in Figure 3.1, were provided by the vessel owner. The lines plan drawing describes how the complex shape of a ship varies in length, breadth and height (Van Dokkum, 2014).

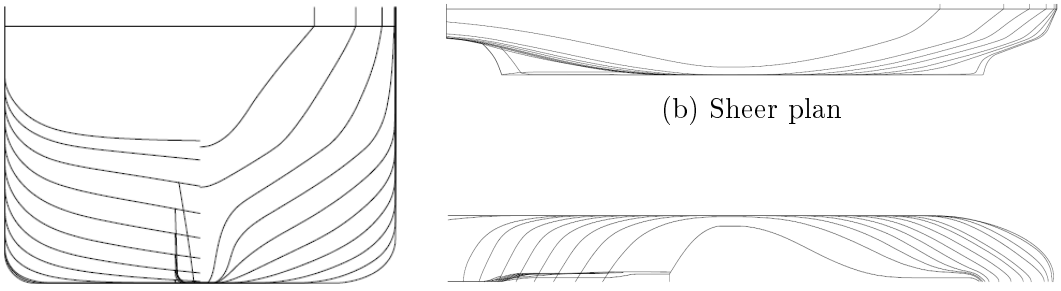

(a) Body plan

(b) Sheer plan

(c) Half-breadth plan

Figure 3.1: Lines plan drawing of the SA Agulhas II.

The hull characteristics of the SA Agulhas II are in many ways equivalent to other ice-going vessels (Moton, 1991). It consists of a thick rounded stem specifically designed to break ice. The stem angle, ϑ, is quite small, approximately 30°. The smaller stem angles results in increased bending moments

applied to the ice at the stem, while maintaining a small horizontal force component (Riska, 2010). The flare angle, β, is nearly 45°. Figure 3.2 gives an illustration of the stem and flare angles. The station of maximum beam is well forward of amidships. Subsequently, the fore body of the vessel is rather full and the longitudinal centre of buoyancy is relatively far forward. Instinctively, these characteristics improve her performance in ice, but may lead to sharp increases in open-water resistance and affect other seakeeping aspects (Moton, 1991). More specifically, the spoon-shaped bow makes her prone to slamming (Omer, 2016*b*).

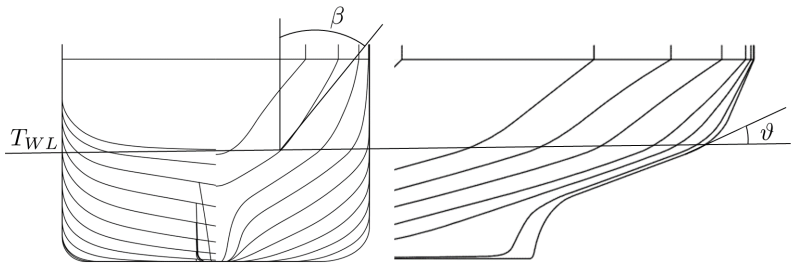

Figure 3.2: Bow flare and stem angle of the SA Agulhas II.

A 3D model of the SA Agulhas II hull was developed from the lines plan drawing in Rhinoceros® Version 6.0. The resultant model is shown in Figure 3.3.

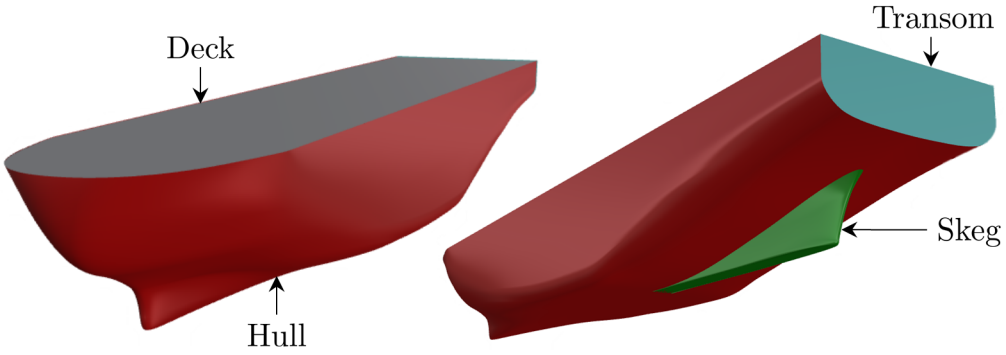

Figure 3.3: The 3D geometry of the SA Agulhas II hull.

3.1.2 Estimation of natural frequencies

The natural frequencies of the heave, roll and pitch motions are estimated in Table 3.2. The equations used to estimate them are derived from the homogenous solution, i.e. no excitation forces, of the uncoupled equations of motions, see Equations 2.24−2.26. The assumptions made for the added mass parameters are in accordance with Simonsen *et al.* (2013) and (Bergdahl, 2008).

Table 3.2: Estimated natural frequencies of the SA Agulhas II.

DOF	Moments of inertia	Added mass	Hydrostatic stiffness	Natural frequency
Heave		$A_{33} \approx m$	$C_{33} = \rho g \nabla A_{WP}$	$f_{n_3} \approx \frac{1}{2\pi}\sqrt{\frac{C_{33}}{m + A_{33}}} \approx 0.149\,\text{Hz}$
Roll	$I_{44} = mk_{44}^2$	$A_{44} \approx 0.15 I_{44}$	$C_{44} = \rho g \nabla G M_f$	$f_{n_4} \approx \frac{1}{2\pi}\sqrt{\frac{C_{44}}{I_{44} + A_{44}}} \approx 0.067\,\text{Hz}$
Pitch	$I_{55} = mk_{55}^2$	$A_{55} \approx I_{55}$	$C_{55} = \rho g \nabla G M_L$	$f_{n_5} \approx \frac{1}{2\pi}\sqrt{\frac{C_{55}}{I_{55} + A_{55}}} \approx 0.112\,\text{Hz}$

In theory, the resonances are expected to occur around these frequencies (Journée and Massie, 2001). These properties will be evaluated further when the RAOs of the vessel are calculated.

3.2 SCALE Winter Cruise

SCALE is a novel interdisciplinary research program which investigates the ecosystem and other oceanographic topics of the South East Atlantic sector in the Southern Ocean (SCALE, 2019). The navigational track of the SCALE Winter Cruise is shown in Figure 3.4.

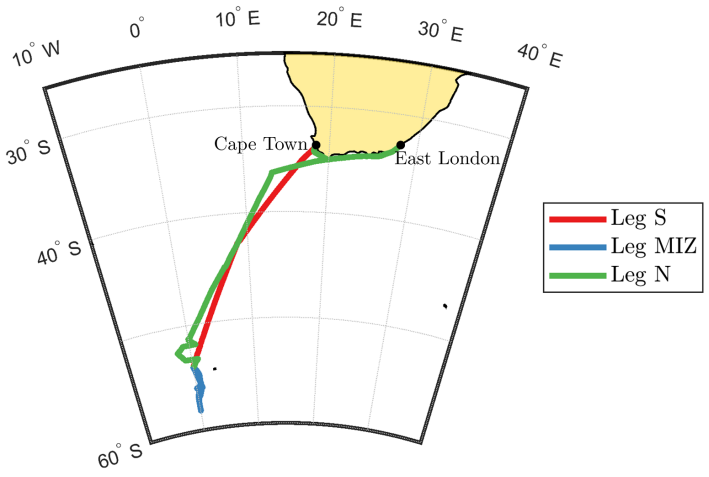

Figure 3.4: The SCALE Winter Cruise navigational track.

The SA Agulhas II departed from Cape Town harbour on the 18 of July and sailed south along the Good Hope line towards the marginal ice zone (MIZ), Leg S. The first sea ice was seen on the 26th of July, after which three days were spent in the MIZ, leg MIZ. Thereafter, she sailed northwards to East London, Leg N. She arrived in the East London harbour on the 7th of

August where an open day was held on the vessel for the stakeholders and public. The open day provided an opportunity for individuals to view the vessel and various scientific experiments that are conducted onboard. Thereafter, she departed from East London, sailed along the coast and arrived in Cape Town harbour on the 12th of August. During the 21 days cruise various oceanographic research activities were conducted. Amongst many others, this included strength tests of sea ice, the measurements of ocean water Conductivity, Temperature and Depth (CTD), as well as the the sampling of trace metals, plastics and phytoplankton.

3.3 Measurement equipment and setup

The measurement equipment used to investigate the heave, roll and pitch motion response of the vessel is presented in Table 3.3.

Table 3.3: Measurement equipment.

1 x 16 channel LMS SCADAS
1 x 12 channel LMS SCADAS
1 x 8 channel LMS SCADAS
BNC and coaxial cables
10 x DC signal conditioners
10 x 3711 Series 12 V DC PCB accelerometers
LMS Test.Lab 11A Turbine Testing software

The vessel was instrumented with ten PCB accelerometers, which were placed at four locations in the hull and the superstructure of the vessel. The configuration of the accelerometers are shown in Figure 3.5.

The accelerometers were placed such that the angular acceleration and angular velocity of the vessel can be calculated using the Six Accelerometer Method (SAM). The SAM methodology is discussed in Appendix B. It consists of a triaxial accelerometer placed at Point 0, located in the port side steering gear room. Point 1 was placed co-planar to Point 0 in the starboard side and measured vertical acceleration. A triaxial accelerometer was placed at Point 2, in the bridge beneath the ship's wheel. Additional vertical and lateral accelerometers were placed at Points $3-5$ in the chain locker. These are not used in the SAM, but are used to validate the calculation of angular acceleration and velocity.

The triaxial accelerometer consisted of three accelerometers mounted on an aluminium block (see Figure 3.6b). This block, as well as the other accelerometers were mounted to the rigid structural members of the ship using superglue, as shown in Figure 3.6c. The accelerometers were connected to noise-cancelling coaxial teflon cables, which then connect to permanently installed

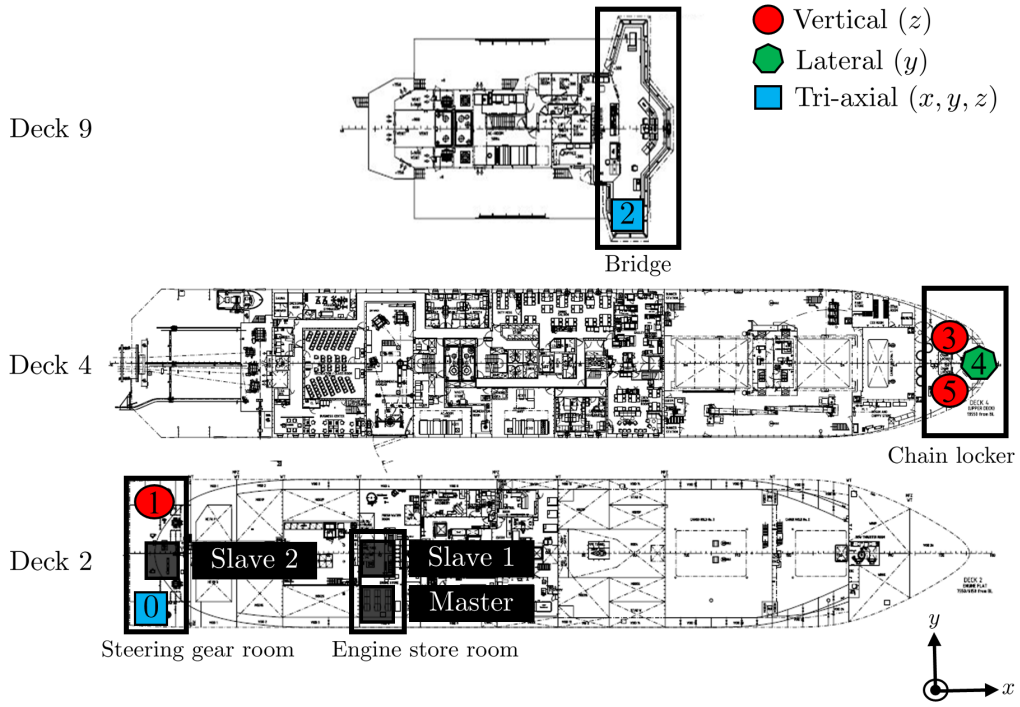

Figure 3.5: Measurement location during the SCALE Winter Cruise.

BNC cables. These BNC cables were connected to three LMS Supervisory Control and Data Acquisition Systems (SCADAS), which were distributed on the ship in a master-slave configuration, as depicted in Figure 3.5. The master SCADAS was connected via an ethernet cable to a measurement computer on which LMS Test.Lab Turbine Testing software is used to control and record acceleration data. The slave SCADAS, slave 1 and slave 2 connect to the master with fibre optic cables. The accelerometers in the chain locker and the bridge were connected to the master and slave 1 SCADAS, while those in the steering gear room were connected to slave 2. Figure 3.6a shows a photograph of the measurement laptop, master and slave 1 SCADAS.

Acceleration data were sampled continuously during the 21 day cruise at a sample rate of 2048 Hz and saved onto the measurement laptop every 5 minutes. In total 0.63 TB of data were sampled. In order to ensure correct measurement system functionality and that reliable data were sampled, daily veracity checks were conducted using an in-house MATLAB® code (Van Zijl, 2020).

(a)

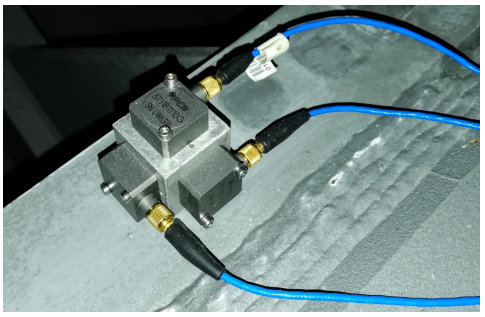

(b)

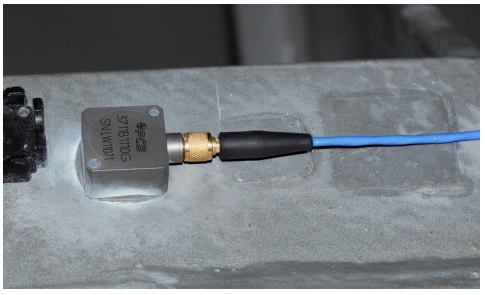

(c)

Figure 3.6: Photographs of the measurement equipment showing (a) the measurement laptop computer, master and slave 1 SCADAS, (b) a triaxial accelerometer in the port side steering gear room and (c) the accelerometer in the starboard side mounted with superglue.

3.4 Consortium measurements

The consortium measurements taken during the SCALE Winter Cruise are shown in Table 3.4. The Scientific Data System (SDS) forms part of the vessel and provides relevant voyage information for scientists. Members of the SVRG were tasked to conduct visual observations of the sea state every ten minutes to gain insight into the sea state conditions. The seaway was described using the Beaufort Wind Force Scale, an empirical scale that relates wind speed to observed conditions at sea (Journée and Massie, 2001). Finally, GoPro video footage of the sea state was taken when possible.

Visual observations of the sea state are common practice, but discrepancies tend to exist between the observed and actual seaway (Bertram, 2012). Therefore, sea state parameters of interest were acquired from the European Centre for Medium-Range Weather Forecasts (ECMWF) ERA5 database (Copernicus Climate Change Service, 2017). These include the significant wave height (H_s), peak wave period (T_p), mean wave period (T_m) and mean wave direction (η). They were obtained with an hourly temporal resolution and a spatial grid resolution of 31 km or 0.28125°. In addition, the data is encoded in NetCDF format, which was analysed using MATLAB®. An example plot can be seen

in Figure E.3 in Appendix E.

Table 3.4: Consortium Measurements during SCALE Winter Cruise.

Scientific Data System (SDS)
1. Longitude and Latitude 2. Speed over ground (SOG) 3. Ship heading 4. Wind speed and direction 5. Water depth
Visual observations of the sea state
1. Beaufort number 2. Direction of the main wave train relative to the ship 3. Significant wave height 4. Ratio of the wave length relative to the ship length 5. Period of encounter

3.5 Data processing

A graphical representation of the data processing to determine the heave, roll and pitch motion response of the SA Agulhas II is shown in Figure 3.7. Data processing was done using MATLAB®.

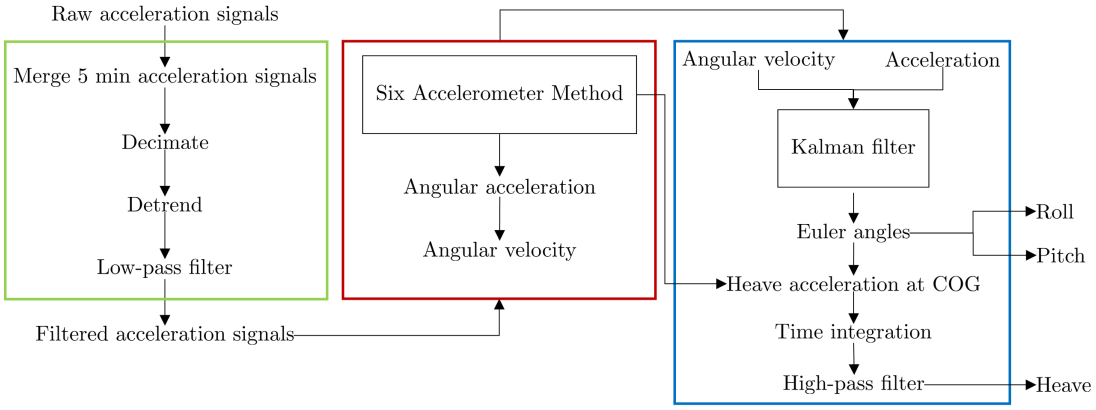

Figure 3.7: Data processing procedure to determine the motion response.

The process was divided into three steps. Firstly, 5 minute data recordings were merged into one file. Thereafter, the data was downsampled from a sample rate of 2048 Hz to 32 Hz using the `decimate.m` function. Next, the `detrend.m` function was used to remove any linear trend in the recorded data.

A low-pass filter is applied to the acceleration signal to remove high frequency content.

A low-pass filter is a digital filter used in signal processing to reduce the bandwidth of a time signal prior to performing frequency analysis (Brandt, 2010). In short, it reduces the amount of noise in relation to the frequency range of interest (Nielsen, 2005). For theoretical and mathematical formulation of digital filters, reference is made to Brandt (2010).

Based on disussions in Nielsen (2005) and Gourlay *et al.* (2015), it is expected that the wave-induced motion will occur within an frequency range of 0.033–0.3 Hz. Therefore, an 8^{th} order low-pass Butterworth Infinite Impulse Response (IIR) filter was applied to the data with a cut-off frequency, f_c, and the pass-band frequency, f_p, of 1 Hz and 1.5 Hz, respectively. This filter was designed using the built-in Signal Processing Toolbox available in MATLAB®. Figure 3.8 gives an illustration of the frequency response of the filter.

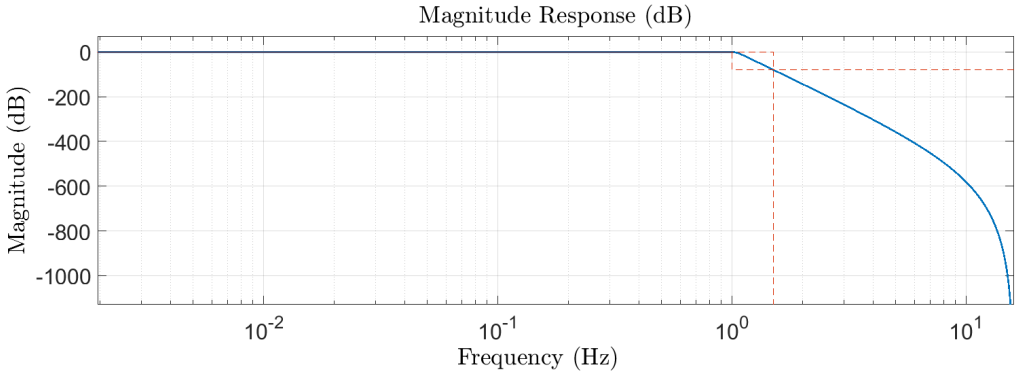

Figure 3.8: Low-pass filter with $f_c = 1$ Hz and $f_p = 1.5$ Hz.

During the next step angular accelerations and velocities are calculated using the SAM, presented in Appendix B. Thereafter, a Kalman filter algorithm combines acceleration data and angular velocity data to determine roll and pitch motion. Finally, the heave displacement is calculated by integrating the heave acceleration. The integration was done in the time domain using the `timeint.m` function available in the ABRAVIBE toolbox, developed by Brandt (2018). This function uses a 1st order high-pass IIR Butterworth filter with a cut-off frequency of 0.02 Hz. Therefore, any low-frequency drift during the integration process is removed (Brandt, 2010).

Chapter 4

Motion response in irregular seas

4.1 Introduction

Having successfully performed full-scale measurements onboard the SA Agulhas II, high quality acceleration data were obtained and used in the Six Accelerometer Method (SAM) to determine her angular velocity. This chapter presents the measured heave, roll and pitch responses in irregular seas and the prediction thereof based on the relationship between the RAOs and wave spectrum. Figure 4.1 shows the methodology flowchart to obtain the measured and predicted responses. In this chapter, the Public Domain Strip Method (PDSTRIP) (Bertram *et al.*, 2006) is used to calculate the RAOs of the SA Agulhas II.

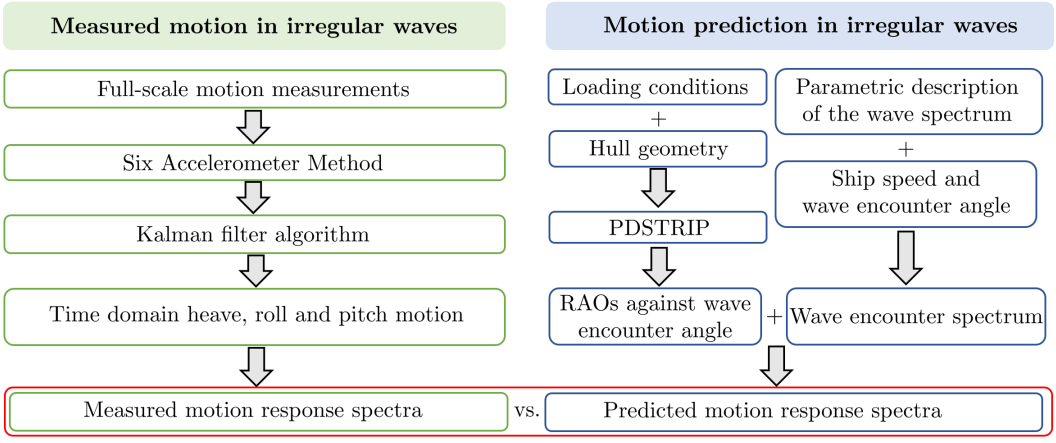

Figure 4.1: Methodology flowchart for the measurement and prediction of ship motion response.

4.2 Description of case studies

Six case studies were identified to investigate the motion responses. The operational conditions of these case studies are given in Table 4.1.

Table 4.1: Operational conditions during six case studies.

Case	Date	Time	Location	Speed [kn]
A	20/07/2019	08:00 - 10:00	38° 20′ S 13° 20′ E	14.9
B	30/07/2019	12:00 - 14:00	53° 21′ S 00° 52′ W	8.7
C	03/08/2019	14:00 - 16:00	42° 40′ S 08° 50′ E	16.5
D	24/07/2019	07:50 - 8:20	54° 00′ S 00° 00′ E	0
E	24/07/2019	08:20 - 08:50	54° 00′ S 00° 00′ E	0
F	21/07/2019	11:30 - 14:00	43° 01′ S 08° 28′ E	11

The selection of these case studies were based on the sea state parameters, the encounter angle and the ship's speed. Additional criteria applied include a constant average speed and heading. Furthermore, the duration of each case had to be at least 10 minutes long to include statistically significant motion measurements (Ha and Gourlay, 2018).

Information about the encountered sea states (obtained from the ECMWF ERA5 database) is given in Table 4.2. Figure 4.2 depicts the ITTC wave spectrum for each case study. The encounter angle measured in degrees, χ, was calculated as follows (Montazeri, 2016):

$$\chi = 180° - (\overline{\psi} - \eta) \tag{4.1}$$

where $\overline{\psi}$ is the ship heading, which is measured in a clockwise direction relative to North in degrees and η is the mean wave direction in degrees.

Table 4.2: Wave state parameters for six case studies obtained from the ECMWF ERA5 data base.

Case	Beaufort scale	$\overline{\psi}$ [deg]	H_s [m]	T_m [s]	T_p [s]	η [deg]	χ [deg]
A	2	220	2.29	9.2	10.7	207	167
B	8	310	4.68	9.52	11.03	271	141
C	4	25	3.5	7.72	7.73	313	108
D	5	160	3.14	9.4	9.13	306	326
E	5	115	3.14	9.4	9.13	306	349
F	7	210	5.13	9.6	11.46	284	254

A summary based on visual observations during the case studies is given as follows:

- Case A: The ocean was calm with few small breaking wave crests.
- Case B: The seaway was harsh with frequent wave slamming. Some observers stated that they felt uncomfortable due to roll motion of the vessel. Additional figures for this case are presented in Appendix E.
- Case C: The vessel was moving through small waves at 16 kn experiencing a few wave slams.
- Case D: The ship was at a CTD station in dynamic positioning (DP) with moderate waves approaching from astern.
- Case E: The ship still in DP at the CTD station, but positioned so that it was experiencing stern quartering waves.
- Case F: The sea state was confused with stern quartering swell waves and head wind waves.

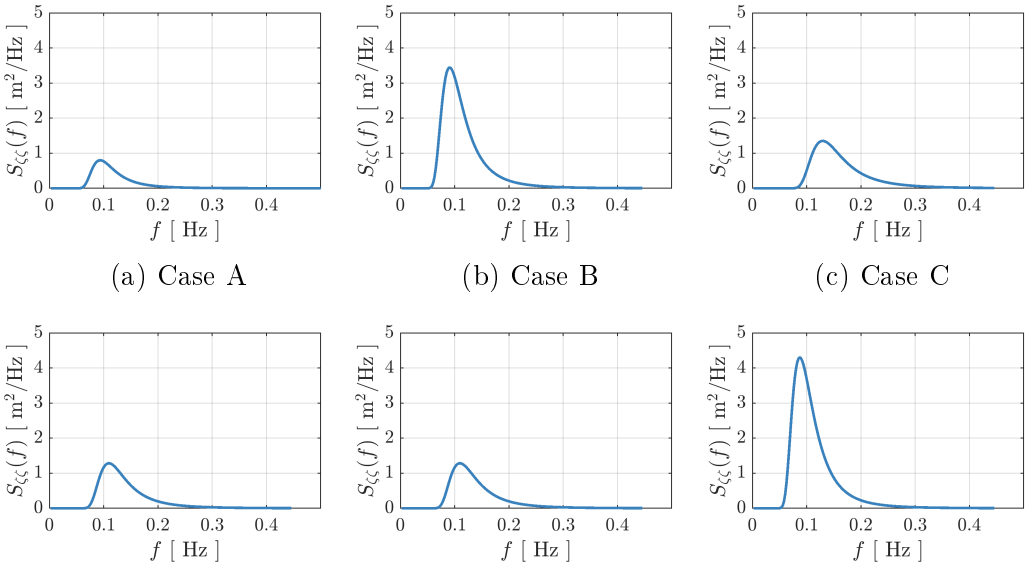

(a) Case A (b) Case B (c) Case C

(d) Case D (e) Case E (f) Case F

Figure 4.2: Wave spectra for case studies calculated using parameters obtained from the ECMWF ERA5 database.

4.3 Determination of measured motion responses

This section discusses the determination of the heave, roll and pitch response (ξ_3, ξ_4 and ξ_5) of the SA Agulhas II from onboard measurements. The Six Accelerometer Method (SAM), which relies on fundamental kinematic principles, was used to obtain the angular velocity of the vessel. The SAM is discussed in more detail in Appendix B.

The roll and pitch motion of a vessel cannot be obtained by integrating angular velocity measurements since the angular velocities are not the rate of change of Euler angles (Lewandowski, 2004). Additionally, the integration of angular velocity does not have any physical interpretation (Fossen, 2011). Instead, a Kalman filter algorithm is recommended (Kim, 2011).

A Kalman filter algorithm (Kalman, 1960), also known as the least-quadratic estimator, is a mathematical tool used to calculate the state of a dynamic system from noisy measurements and an observation model (Fossen, 2011). The system state in question is the orientation of the SA Agulhas II, more specifically roll and pitch. The Kalman filter algorithm is used to determine her orientation by combining acceleration data obtained from a triaxial accelerometer located at Point 0, and angular velocities obtained from the SAM. This process is commonly known as sensor fusion (Kim, 2011).

Appendix A gives a review of Euler angles and unit quaternions. Furthermore, reference is made to Appendix A.5 which outlines the determination of the Euler angles by means of angular velocity and linear acceleration data.

For the purpose of this section roll, pitch and yaw angles (ξ_4, ξ_5 and ξ_6) are defined as ϕ, θ and ψ.

The following section describes the calculation of the roll and pitch motion through a Kalman filter algorithm using the process outlined by Kim (2011).

4.3.1 Kalman filter algorithm

Acceleration and angular velocity data are available at discrete points in time. Therefore, a system model is described by discrete equation of state changes (i.e. the process equation) and output equations (i.e. the measurement equation) (Bieda and Jaskot, 2016). The system is described in the discrete time format as follows (Titterton and Weston, 2004):

$$\begin{aligned} \boldsymbol{x}_{k+1} &= \boldsymbol{F}\boldsymbol{x}_k + \boldsymbol{v}_k \\ \boldsymbol{z}_k &= \boldsymbol{H}\boldsymbol{x}_{k+1} + \boldsymbol{w}_k \end{aligned} \tag{4.2}$$

where $\boldsymbol{x}_{k+1}$ is the state of the model at time t_{k+1}; $\boldsymbol{x}_k$ is the state of the model at time t_k; $\boldsymbol{F}$ is the state transition matrix that relates the state vector of the current state, $\boldsymbol{x}_k$, to the next state, $\boldsymbol{x}_{k+1}$; $\boldsymbol{v}_k$ is the system noise; $\boldsymbol{w}_k$ is the

measurement noise; $\boldsymbol{z}_k$ is the measurement vector; and $\boldsymbol{H}$ is the measurement matrix.

The system and measurement noise, $\boldsymbol{w}_k$ and $\boldsymbol{v}_k$, are characterized by a system noise covariance matrix ($\boldsymbol{Q}$) and a measurement noise covariance matrix ($\boldsymbol{R}$). The Kalman filter algorithm is divided into two stages, the prediction and the correction stage. The prediction stage is concerned with the prediction of the state of the system based on a previous estimation. The correction stage updates the predicted estimate by combining the prediction with a new measurement (Titterton and Weston, 2004). The flow diagram of the Kalman filter algorithm to determine roll and pitch is shown in Figure 4.3.

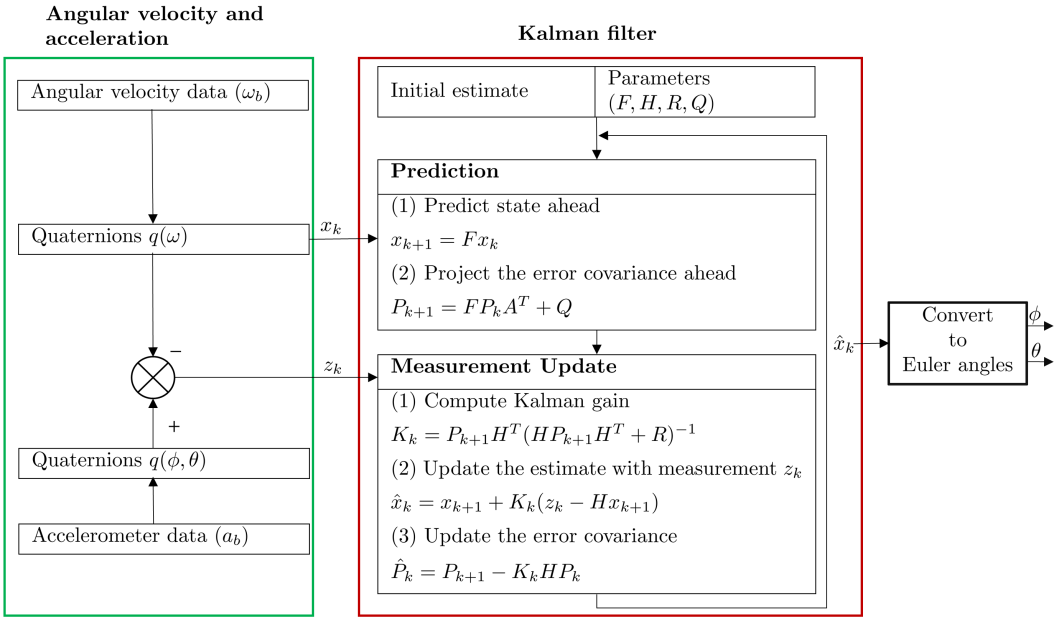

Figure 4.3: Flow diagram of the Kalman filter algorithm

4.3.1.1 The prediction process

During the prediction step, the current state of the process model, $\boldsymbol{x}_{k+1}$, is predicted by relating it to the previous state, $\boldsymbol{x}_k$, with matrix $\boldsymbol{F}$ (Kim, 2011):

$$\boldsymbol{x}_{k+1} = \boldsymbol{F}\boldsymbol{x}_k \tag{4.3}$$

The state vector chosen is the unit quaternions, which are an alternative four parameter method used to describe the orientation of a body, as discussed in Section A.3. Therefore, the state vector is given by:

$$\boldsymbol{x}_k = \begin{bmatrix} q_0 & q_1 & q_2 & q_3 \end{bmatrix}_k^T \tag{4.4}$$

The matrix $\boldsymbol{F}$ is determined by expressing the relationship between the angular velocity and the rate of change in quaternions, i.e. Equation A.10, in discrete form:

$$\boldsymbol{F} = \boldsymbol{I} + \frac{\Delta t}{2}\begin{bmatrix} 0 & -\omega_x & -\omega_y & -\omega_z \\ \omega_x & 0 & \omega_z & -\omega_y \\ \omega_y & -\omega_z & 0 & \omega_x \\ \omega_z & \omega_y & -\omega_x & 0 \end{bmatrix} \tag{4.5}$$

where ω_x, ω_y and ω_z are the roll, pitch and yaw rates obtained from the SAM. Thereafter, the error covariance matrix for the current state, $\boldsymbol{P}_{k+1}$, is determined:

$$\boldsymbol{P}_{k+1} = \boldsymbol{F}\boldsymbol{P}_k\boldsymbol{F}^T + \boldsymbol{Q} \tag{4.6}$$

4.3.1.2 The measurement update

In the correction part, the model is corrected by combining the predicted state and actual measurements. The measurement vector, $\boldsymbol{z}_k$, is obtained from the attitude determined by a triaxial accelerometer, as discussed in Section A.5.2. It follows that, $\boldsymbol{z}_k$, may be expressed as (Kim, 2011):

$$\boldsymbol{z}_k = \begin{bmatrix} q_0 \\ q_1 \\ q_2 \\ q_2 \end{bmatrix}_k = \begin{bmatrix} \cos\frac{\phi}{2}\cos\frac{\theta}{2}\cos\frac{\psi}{2} + \sin\frac{\phi}{2}\sin\frac{\theta}{2}\sin\frac{\psi}{2} \\ \sin\frac{\phi}{2}\cos\frac{\theta}{2}\cos\frac{\psi}{2} - \cos\frac{\phi}{2}\sin\frac{\theta}{2}\sin\frac{\psi}{2} \\ \cos\frac{\phi}{2}\sin\frac{\theta}{2}\cos\frac{\psi}{2} + \sin\frac{\phi}{2}\cos\frac{\theta}{2}\sin\frac{\psi}{2} \\ \cos\frac{\phi}{2}\cos\frac{\theta}{2}\sin\frac{\psi}{2} - \sin\frac{\phi}{2}\sin\frac{\theta}{2}\cos\frac{\psi}{2} \end{bmatrix}_k \tag{4.7}$$

The model prediction is updated with a prior estimate from the actual measurements ($\boldsymbol{z}_k - \boldsymbol{H}\boldsymbol{x}_{k+1}$):

$$\hat{\boldsymbol{x}}_k = \boldsymbol{x}_{k+1} + \boldsymbol{K}_k(\boldsymbol{z}_k - \boldsymbol{H}\boldsymbol{x}_{k+1}) \tag{4.8}$$

where $\hat{\boldsymbol{x}}_k$ is the updated state vector and $\boldsymbol{K}_k$ is the Kalman gain matrix, used to correct the estimated state vector (Titterton and Weston, 2004). The Kalman gain matrix, $\boldsymbol{K}_k$, is calculated using the following equation:

$$\boldsymbol{K}_k = \frac{\boldsymbol{P}_{k+1}\boldsymbol{H}^T}{(\boldsymbol{H}\boldsymbol{P}_{k+1}\boldsymbol{H}^T + \boldsymbol{R})} \tag{4.9}$$

Finally, the error covariance matrix, $\boldsymbol{P}_k$, is updated as follows:

$$\hat{\boldsymbol{P}}_k = \boldsymbol{P}_{k+1} - \boldsymbol{K}_k\boldsymbol{H}\boldsymbol{P}_k \tag{4.10}$$

In the above equations $\boldsymbol{H}$ is an identity matrix, $\boldsymbol{I}_{4\times4}$. The system and measurement noise matrices, $\boldsymbol{Q}$ and $\boldsymbol{R}$, are considered to be the design factor of the Kalman filter algorithm estimated through trial and error (Kim, 2011; Perez, 2005). The measurement noise matrix, $\boldsymbol{R}$, is chosen based on confidence in the measurement vector. Generally speaking, larger values for $\boldsymbol{R}$ indicate more confidence in the measurement stage and less in the prediction (Salmony, 2018). For this study, $\boldsymbol{Q}$ and $\boldsymbol{R}$ was chosen as follows:

$$\boldsymbol{Q} = 10^{-5}\boldsymbol{I}_{4\times4} \tag{4.11}$$

$$\boldsymbol{R} = \text{diag}([\sigma_{q_0}^2, \ \cdots \ , \sigma_{q_3}^2]) \tag{4.12}$$

where $\sigma_{q_n}^2$ is defined as the variance of the measurement vector. Notice that the square root of the variance is the standard deviation, σ_{q_n}, of the measurement vector (Labbe, 2020).

To summarize, the Kalman filter algorithm presented above yields the quaternions, which are determined through a combination of angular velocity and acceleration measurements. As illustrated in Section A.4, the quaternions can be converted to Euler angles as follows (Kim, 2011):

$$\phi = \text{atan2}\left(\frac{2(q_2q_3 + q_1q_0)}{1 - 2(q_1^2 + q_2^2)}\right) \tag{4.13}$$

$$\theta = -\arcsin\left(2(q_1q_3 - q_2q_0)\right) \tag{4.14}$$

4.3.2 Heave displacement

In theory, the heave motion of a vessel can be obtained by integration of acceleration measurements twice (Küchler *et al.*, 2011; Ntamba Ntamba *et al.*, 2019). However, when a DC accelerometer is mounted perpendicular to the Earth's surface, it measures an acceleration of $+1g$ along the vertical axis away from the Earth. In order to remove the gravity component, it is required to rotate the acceleration measurements in the body-fixed frame, (b-frame) to the inertial reference frame (n-frame) (Bender *et al.*, 2010). Following the methods presented by Bender *et al.* (2010), the acceleration in the b-frame can be expressed in the n-frame as follows:

$$\begin{bmatrix} a_{n,x} \\ a_{n,y} \\ a_{n,z} \end{bmatrix} = \boldsymbol{R}(\boldsymbol{\Theta}) \begin{bmatrix} a_{b,x} \\ a_{b,y} \\ a_{b,z} \end{bmatrix} - \begin{bmatrix} 0 \\ 0 \\ g \end{bmatrix} \tag{4.15}$$

where $\boldsymbol{R}(\boldsymbol{\Theta})$ is a rotation matrix used to rotate from the b-frame to the n-frame, which is discussed in Appendix A.2. For ease of reference it follows that the heave acceleration $a_{n,z}$ in the n-frame is calculated as follows (Bender *et al.*, 2010):

$$a_{n,z} = (-a_{b,x}\sin\theta + a_{b,y}\cos\theta\sin\phi + a_{b,z}\cos\theta\cos\phi) - g \tag{4.16}$$

The heave displacement, ξ_3, can then be determined by integrating $a_{n,z}$ twice using the `timeint.m` function, as discussed in Section 3.5.

It should be noted that the methodology presented above was applied to the heave acceleration at the COG of the vessel which can be determined through the kinematic principles of a rigid body, shown in Equation B.2.

4.4 Response Amplitude Operators

It is necessary to have sufficient resolution of the RAOs to predict the motion response in irregular seas (Montazeri, 2016). Therefore, PDSTRIP is used to calculate the RAOs responses of the SA Agulhas II. It is based on two-dimensional potential flow theory and solves the equations of motion in the frequency domain. This yields the complex transfer functions of the motion responses, i.e. the RAOs.

Gourlay *et al.* (2015) conducted a systematic study using PDSTRIP and various other commercial hydrodynamic software packages. The authors documented that the results obtained from PDSTRIP were in good agreement with the model-scale experiments and other software packages. Similar results were presented by Ntamba Ntamba *et al.* (2019), who calculated the RAOs of the SA Agulhas II using PDSTRIP and commercial software OCTUPUS SEAWAY. Another benefit of using PDSTRIP is that the forward speed of the vessel can be included, although it is more suitable to low speeds (Schoop-Zipfel, 2016). At higher speeds, it might be limited due to the simplistic manner in which strip theories account for forward speed (Tezdogan *et al.*, 2015). Further limitations include the linearity between the motion response and an incident wave. This implies that it might not be applicable to high sea states with lots of slamming (Faltinsen, 1990). Nevertheless, it provides a quick simulation time at a sufficient level of accuracy (Schoop-Zipfel, 2016).

The hull geometry input for PDSTRIP consists of 40 equally spaced station curves, which are shown in Figure E.2 in Appendix E.2. The mass distribution data used is similar to that obtained from the loading conditions observed during the 2019 SCALE Winter Cruise. The relevant input parameters are given in Table 4.3.

Table 4.3: Input parameters obtained from loading conditions.

Δ [m^3]	T [m]	LCG [m]	KG [m]	GM_f [m]	k_{44} [m]	k_{55} [m]	k_{66} [m]
11,914	6.9	57.85	8.81	1.63	$0.37B$	$0.25L_{pp}$	$0.25L_{pp}$

Additional input parameters include the wave encounter direction, χ, which was calculated in 10° intervals from 0° to 180°. The RAOS were calculated over a wave frequency range from 0.06 rad/s to 1.8 rad/s, similar to the frequency range presented by Montazeri (2016). Finally, the ship speed was specified from 0 kn to 16 kn with 1 kn increments.

4.5 Response spectra generation

Similar to ocean waves, the motion of a ship in irregular seas will vary in space and time (Perez, 2005). Therefore, a Power Spectral Density (PSD) is calculated to represent the energy distribution of the motion response in the frequency domain. For this study, Welch's method was used to compute the the motion response spectra, $S_{\xi\xi_i}$. For this, the `pwelch.m` function in MATLAB® was implemented. For theoretical background about Welch's method, reference is made to Brandt (2010).

For calculation of the motion response spectra, the following parameters were specified: decimated sampling frequency, f_s, of 2^8 Hz , Hanning window with 50% overlap and a block size of 2^{13} NFFT points. For the sake of consistency, the frequency increment of the PSDs is the same for all cases. The frequency increment is calculated as follows:

$$\Delta f = \frac{f_s}{\text{NFFT}} \tag{4.17}$$

This results in a constant Δf of 3.9×10^{-3} Hz for all cases, which is common practice according to literature (Ha and Gourlay, 2018; Sirigu *et al.*, 2018).

Furthermore, since the time signals are random, the assumption is usually made that they are statistically stationary (Brandt, 2010). This implies that statistical parameters, such as root-means-square (RMS) and standard deviation, remains constant over the measurement period. This was evaluated by means of the `framestat.m` function, which is available in the ABRAVIBE toolbox (Brandt, 2018).

For prediction of the motion response spectra from the RAOs and the wave spectrum, reference is made to Section 2.4.4. In order to compare the predicted and measured response spectra, it is required that both provide information over similar frequency ranges and at similar discrete frequency points (Skandali, 2015). Therefore, the predicted motion response spectra are linearly interpolated over a frequency range similar to the measured response spectra.

4.5.1 Statistics of motion responses

Spectral moments are defined as follows (Perez, 2005):

$$m_{\xi_i}^n = \int_0^\infty S_{\xi\xi_i}(f) f^n df \tag{4.18}$$

where n denotes the order of the spectral moment. The square root of the 0^{th}-order moment corresponds to the RMS value of the response. The square roots of the 2^{nd}-and 4^{th}-order moments correspond to the RMS value of the velocity and acceleration of the responses, respectively (Tezdogan *et al.*, 2014). Spectral moments are used to define the statistical characteristics of the motion response (Ha and Gourlay, 2018). Furthermore, they are useful to evaluate the differences which exist between the measured and predicted motion responses (Montazeri, 2016).

The significant amplitude, $\xi_{i,1/3}$, is defined as the average of the one-third of the highest motion amplitudes and is determined from the 0^{th}-order moment as follows (Ha and Gourlay, 2018):

$$\xi_{i,1/3} = 2\sqrt{m_{\xi,i}^0} \tag{4.19}$$

The mean period, T_m, is the period between two crests, which can be calculated as follows:

$$T_m = \frac{m_{\xi_i}^0}{m_{\xi_i}^1} \tag{4.20}$$

The zero-crossing period, T_z, is the period between two up-crossings of the zero level in a specific response (DNVGL, 2018). It is determined as follows:

$$T_z = \sqrt{\frac{m_{\xi_i}^0}{m_{\xi_i}^1}} \tag{4.21}$$

The peak period, T_p, is the period of the response with the most energy in the response spectrum and the most probable response in the short term. It is calculated from the peak frequency f_p, which is read from the PSD as follows (DNVGL, 2018):

$$T_p = \frac{1}{f_p} \tag{4.22}$$

4.6 Results

4.6.1 Measured heave, roll and pitch responses

Figures 4.4 and 4.5 show the time domain results and the calculated PSDs, respectively. The largest amplitude motion is seen for Case B, when the vessel was traversing in a Beaufort 8 sea state. Heave response showed broad-banded spectra with significant peaks occurring within a frequency range of 0.08 –

0.14 Hz. The measured roll response spectra show peak frequencies between $0.06 - 0.09$ Hz and are fairly narrow-banded. This is expected when the roll motion is near the resonance roll frequency, as discussed by Ha and Gourlay (2018). Furthermore, roll motion is slightly larger than pitch motion. This could be ascribed to the thick rounded keel of the vessel with no protuberances for stability. This is expected to result in heavy rolling, even in calm seas (Soal, 2014). In addition to this, it was observed that the vessel is steered to encounter bow-quartering waves in order to avoid slamming at the stern. This subsequently leads to increased roll motion. Pitch motion response spectra showed broad-banded responses with significant peaks at frequencies between $0.09-0.17$ Hz. This suggests that pitch motion is predominately affected by wind waves, which are expected to occur between $0.1 - 0.4$ Hz (Montazeri, 2016). Double peaks are seen in Case F. Interestingly, visual observations stated that the sea state was confused and the vessel was experiencing stern quartering and head waves.

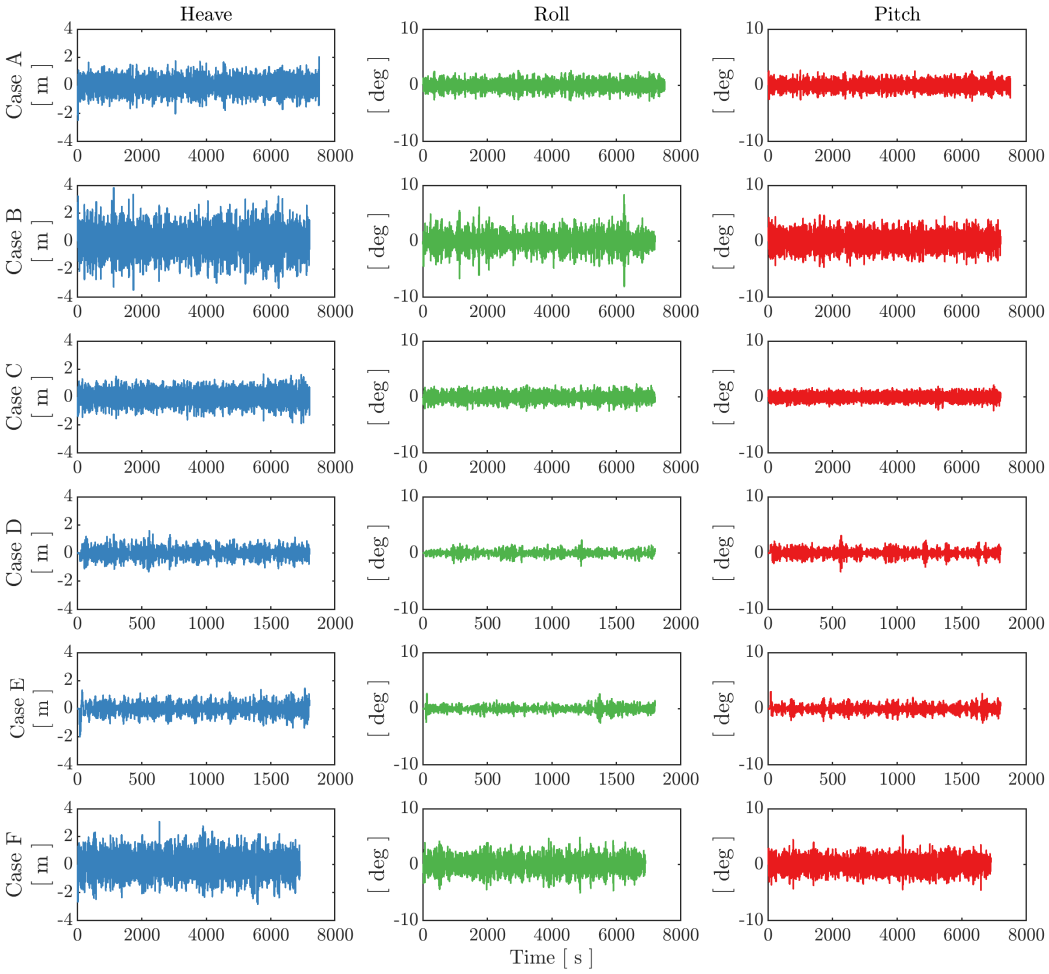

Figure 4.4: Time domain results.

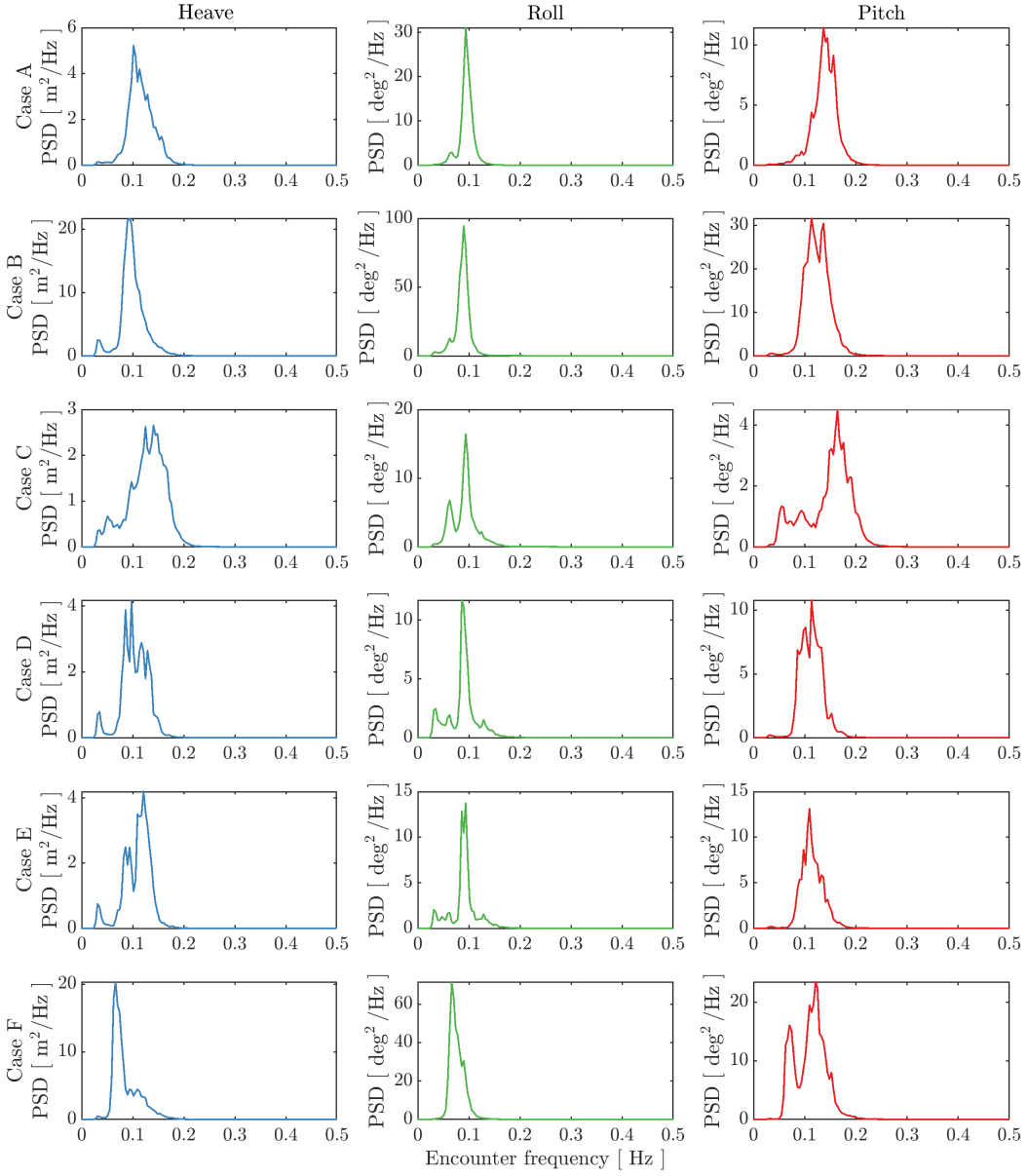

Figure 4.5: Measured motion response spectra.

Table 4.4 summarizes the statistical parameters of the measured responses. The maximum amplitude was obtained from the time series results. A comparison of the maximum and significant amplitudes for each case is shown in Figure 4.6a. In addition, the ratio of the maximum to the significant amplitude ($\xi_{max}/\xi_{1/3}$) is shown in Figure 4.6b. Generally, the ratio ranges between $1.5-2$ in most case studies, but the maximum exceeds twice the significant amplitude on a few occasions. Ha and Gourlay (2018) found that the maximum amplitude did not exceed twice the significant amplitude. However, it was noticed that the significant wave height presented in their study was smaller (ranging

between $0.43-0.92$ m). In addition, their study was conducted using container ships which are much larger than the SA Agulhas II.

Table 4.4: Measured maximum ($\xi_{3,max}$) and significant amplitudes ($\xi_{3,1/3}$) and peak (T_p), mean (T_1) and zero-crossing period (T_z)

		Case					
		A	B	C	D	E	F
Heave							
$\xi_{3,max}$	[m]	2.42	3.95	1.64	1.52	2.01	2.79
$\xi_{3,1/3}$	[m]	0.97	1.83	0.89	0.87	0.87	1.57
T_p	[s]	9.85	10.67	7.12	10.24	8.26	15.06
T_m	[s]	8.65	10.06	7.89	9.58	9.19	11.73
T_z	[s]	8.45	9.77	7.57	9.29	8.92	11.2
Roll							
$\xi_{4,max}$	[deg]	2.66	8.33	2.34	2.32	2.68	4.89
$\xi_{4,1/3}$	[deg]	1.59	2.91	1.38	1.11	1.14	2.68
T_p	[s]	10.67	11.14	10.67	11.64	10.67	15.06
T_m	[s]	10.49	11.42	10.85	11.37	11.11	13.01
T_z	[s]	10.34	11.2	10.36	10.8	10.65	12.74
Pitch							
$\xi_{5,max}$	[deg]	2.81	4.72	2.15	3.13	2.79	5.24
$\xi_{5,1/3}$	[deg]	1.42	2.6	1.06	1.39	1.39	2.28
T_p	[s]	7.32	8.83	6.1	8.83	9.15	8.26
T_m	[s]	7.19	8.03	6.85	8.83	8.73	9.02
T_z	[s]	7.08	7.88	6.55	8.66	8.58	8.7

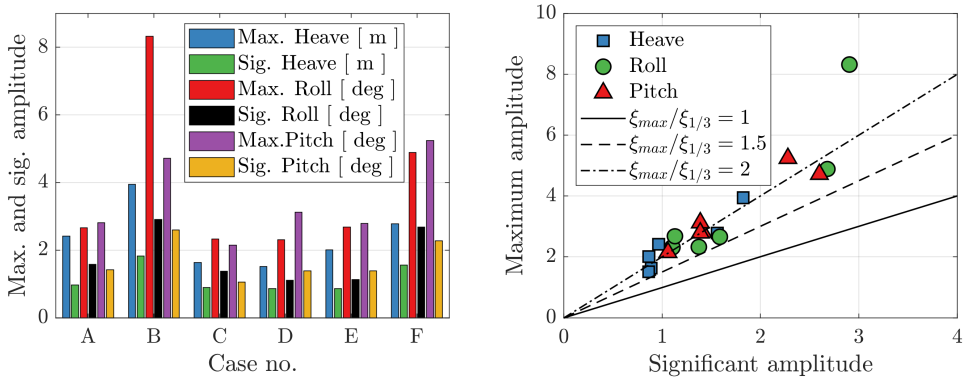

(a) (b)

Figure 4.6: (a) Comparison of maximum and significant amplitudes; and (b) ratio of maximum to significant amplitudes.

4.6.2 Response Amplitude Operators

The amplitudes of the RAOs, A_i, for the SA Agulhas II at 0 kn are shown in Figure 4.7.

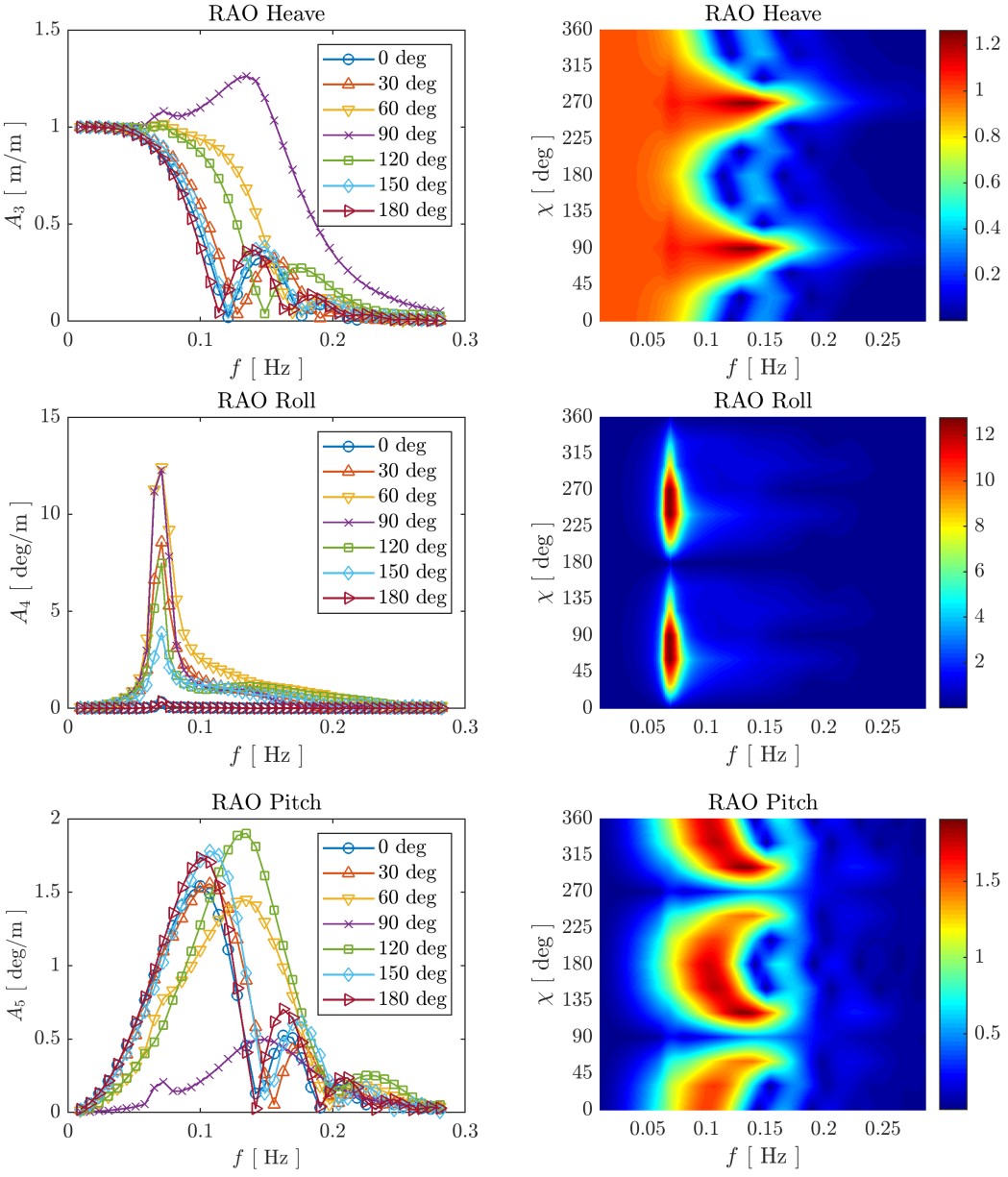

Figure 4.7: Amplitudes of RAOs the SA Agulhas II at 0 kn.

The amplitude of heave RAO has a shape similar to that of a low-pass filter (see Figure 3.8). Interestingly, peak amplitudes are observed at approximately 0.14 Hz, which is close to $f_{n3} \approx 0.149$ Hz. The maximum heave amplitude is seen in beam seas. Furthermore, at higher frequencies (above 0.25 Hz) the

beam of the ship is close to or greater than the wave length. As a result, the excitation forces acting upon the vessel is smaller and therefore the motion response is reduced (Höfler and Höfler, 2017).

The amplitude of the roll RAOs show a narrow-banded response with peaks at 0.071 Hz, which is significantly close to $f_{n4} \approx 0.067$ Hz. Interestingly, this is also similar to a rolling period of 13.63 s (0.073 Hz) depicted on the loading conditions. Furthermore, the absolute maximum roll motion amplitudes are seen for stern quartering to beam seas ($\chi = 60 - 90\,\text{deg}$), which decreases significantly for following and head waves.

The amplitude of the pitch RAOs show relatively broad-banded responses with the lowest amplitudes seen for beam seas. Peaks occur at various frequencies ranging from $0.10 - 0.13$ Hz, depending on the encountered wave direction. This corresponds to the estimated natural frequency, $f_{n5} \approx 0.112$ Hz.

In Chapter 5, the RAOs in head waves are further evaluated, along with the added resistance using CFD. The following section presents the predicted motion response spectra.

4.6.3 Predicted response spectra

Comparisons of the predicted and measured response spectra are given in Figure 4.8 and statistical parameters obtained from the predicted response spectra are shown in Table 4.5. Furthermore, the percentage difference between the measured and predicted statistical parameters are presented in Figure 4.9.

Heave and pitch responses are predicted with reasonably accuracy, with the exceptions being Cases C and F. With regards to Case C, it is noticed that the vessel was travelling at a substantial speed of 16.5 kn and in high frequency waves with short wave lengths. As mentioned before, strip theory is more suitable for lower speeds (Schoop-Zipfel, 2016). In addition to high speed, the application thereof in shorter waves could also be limited (Bertram, 2012). In Case F, multiple peaks are observed from the measured response spectra, especially pitch. This suggests that the vessel could have been experiencing a multi-directional sea state, which consists of swell waves and locally generated waves. The prediction of the motion response in such a sea state, or vice versa, is rather complicated (Montazeri, 2016). Other software, such as

When analysing roll motion, it is noted that various discrepancies exist between the predicted and measured spectra, which are evident for all cases except Cases B and E. The roll motion of ships are known to have a number of non-linear effects. Ha and Gourlay (2018) documented two aspects which could affect the roll response. The first aspect discussed is roll damping, which is defined as the physical process when energy is dissipated from roll motion (Saad, 2014). The SA Agulhas II is equipped with anti-rolling tanks, which are partially filled tanks that transfer liquid from side-to-side to reduce the vessel's rolling motion (Fossen, 2011).

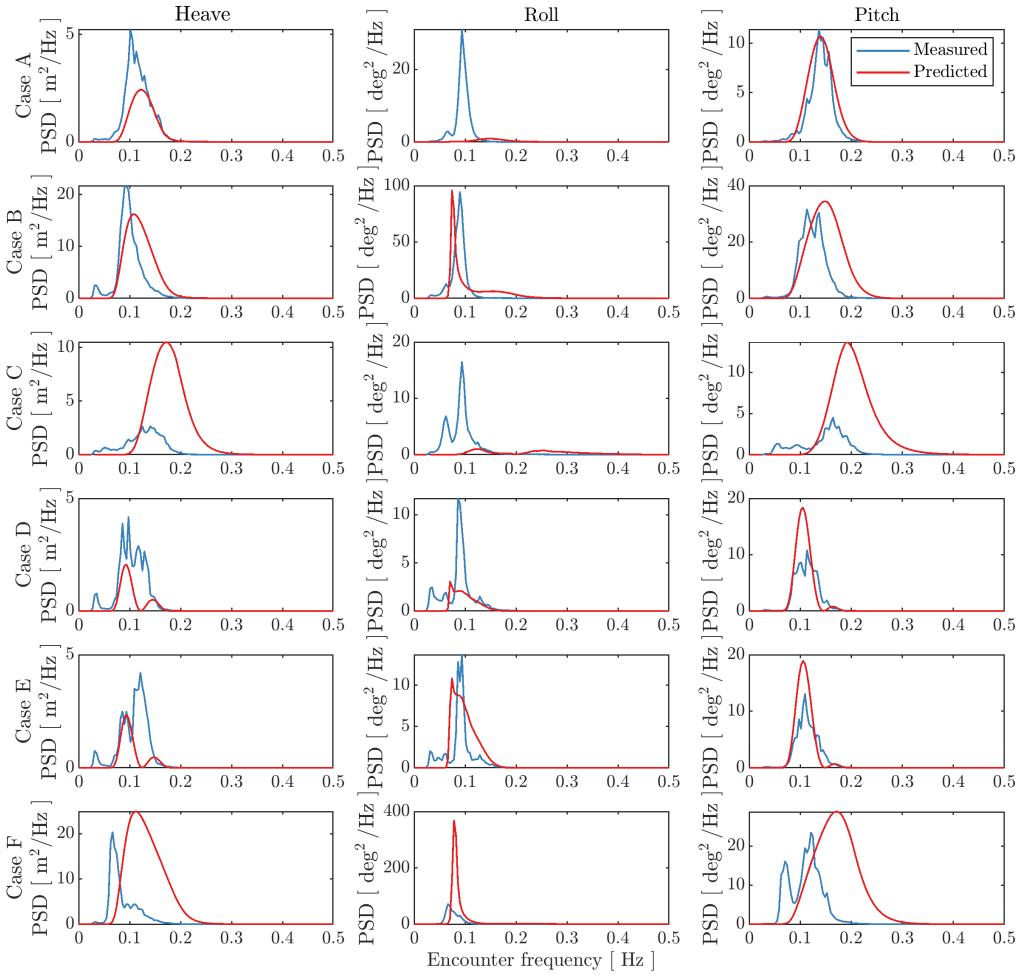

Figure 4.8: Predicted vs. measured response spectra

In PDSTRIP, only potential damping is included to model the effect of roll damping (Gourlay *et al.*, 2015). It is possible to model additional roll damping using semi-empirical methods, such as the Ikeda method (Ikeda *et al.*, 1978). The Ikeda method is included in the commercial software package Octopus Seaway, which was used in the studies presented by Ha and Gourlay (2018) and Ntamba Ntamba *et al.* (2019). In these studies, the authors documented that Octopus Seaway is able model roll damping by adding viscous correction using the Ikeda method. However, this method was developed and validated using towing tank tests. Its validation with full-scale measurement data is not easily obtained and has not been published in open literature (Ha and Gourlay, 2018). Furthermore, the authors found that various discrepancies existed between full-scale measured and predicted roll response even the inclusion of additional roll damping. Ha and Gourlay (2018) stated that "Professor Söding (personal communication, October 6, 2014) recommended no additional viscous damping for ships at substantial forward speeds when using the software PDSTRIP,

which includes hull lift effects on the roll damping." Therefore, care should be taken when additional roll damping is applied. It is recommended that future studies investigate the effects of roll damping using commercial software. Such a study could contribute towards the validation of empirical roll damping methods applied to full-scale ships.

The second aspect discussed by the authors, is a phenomenon known as second-order roll motion. This typically occurs when the natural roll period of a vessel is far from the wave period of 5 - 20 s (Liu, 2003). As a result, second-order difference-frequency wave loads occur close to the natural frequency of the roll motion. These wave loads excite the low-frequency resonant roll response of a vessel. For example, this may have occurred in Case C when the peak wave period was 7.73 s, while the natural period of roll was approximately 14.3 s. These second-order effects are highly non-linear and cannot be calculated with linear strip theory (Ha and Gourlay, 2018). Further investigation is required to study these second-order motion effects.

Despite strip theory's shortcomings, it may be considered sufficiently accurate to predict the motion response of a vessel in waves. This is evident in Cases A, B, D and E. Furthermore, it is worth highlighting that the parametric formulation of the wave spectrum represents an idealised representation thereof, which has been developed using long term statistics since 1955 (Montazeri, 2016). On the other hand, the measured response spectra are based on short term measurements varying between 30 minutes to 2 hours. Therefore, some differences are expected. It would be interesting to investigate various other wave spectra, for example the Joint North Sea Wave Observation Project (JONSWAP) spectrum (Journée and Massie, 2001).

Table 4.5: Predicted significant amplitudes ($\xi_{3,1/3}$) and peak (T_p), mean (T_1) and zero-crossing period (T_z).

		Case					
		A	B	C	D	E	F
Heave							
$\xi_{3,1/3}$	[m]	0.75	2.06	1.84	0.53	0.56	2.88
T_p	[s]	8.26	9.15	5.82	10.67	10.67	8.83
T_m	[s]	7.9	8.33	5.66	9.62	9.67	7.59
T_z	[s]	7.77	8.13	5.56	9.37	9.43	7.35
Roll							
$\xi_{4,1/3}$	[deg]	0.53	2.77	0.73	0.7	1.38	4.55
T_p	[s]	6.74	13.48	8	14.23	13.48	12.8
T_m	[s]	6.47	9.32	4.33	10.19	10.15	11.12
T_z	[s]	6.28	8.61	4.03	9.94	9.91	10.5
Pitch							
$\xi_{5,1/3}$	[deg]	1.63	3.38	2.18	1.6	1.66	3.42
T_p	[s]	7.12	6.74	5.23	9.49	9.49	5.82
T_m	[s]	7.05	6.66	4.88	9.34	9.25	5.84
T_z	[s]	6.95	6.51	4.79	9.24	9.15	5.69

4.7 Sensitivity analysis

As highlighted, the prediction of ship motion responses in irregular seas is complicated and there are many influencing parameters. It was therefore deemed worthwhile to conduct a sensitivity analysis to investigate the various influential parameters. Furthermore, the sensitivity analysis could also assist in future work, for example, using the full-scale motion measurements to estimate the sea state through which the SA Agulhas II is travelling.

The methodology and results of this sensitivity analysis are presented in Appendix C. It was primarily concerned with the predicted significant amplitude and peak period of the motion response. Figure 4.10 depicts the effect of changing various parameters on the significant amplitude of the response. The magnitude of the significant amplitude of each response is primarily influenced by the significant wave height, peak wave period, and the wave encounter direction.

Figure 4.11 depicts the results of the sensitivity analysis on the peak period for each response. The heave and pitch responses are primarily influenced by the peak wave period, the wave encounter direction and the ship speed. The roll response is significantly influenced by the peak wave period, the roll radii of gyration, the wave encounter direction and the transverse metacentric height.

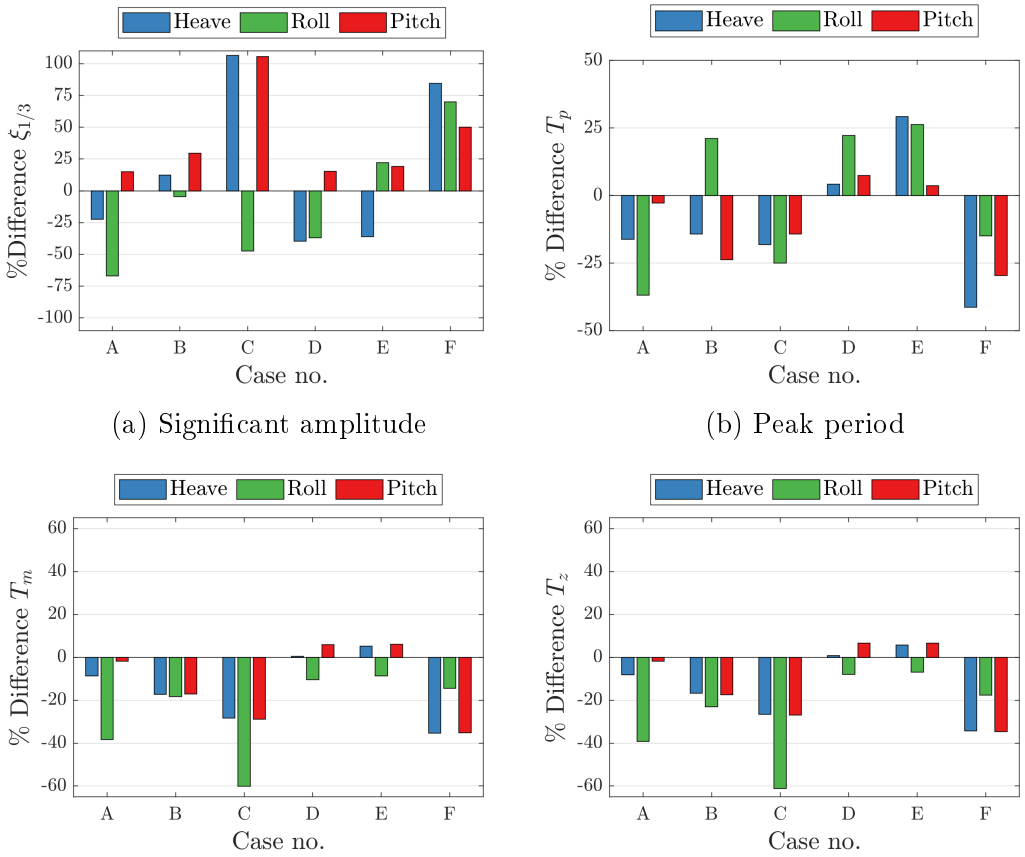

(a) Significant amplitude (b) Peak period

(c) Mean period (d) Zero-crossing period

Figure 4.9: Percentage difference between predicted and measured statistical parameters.

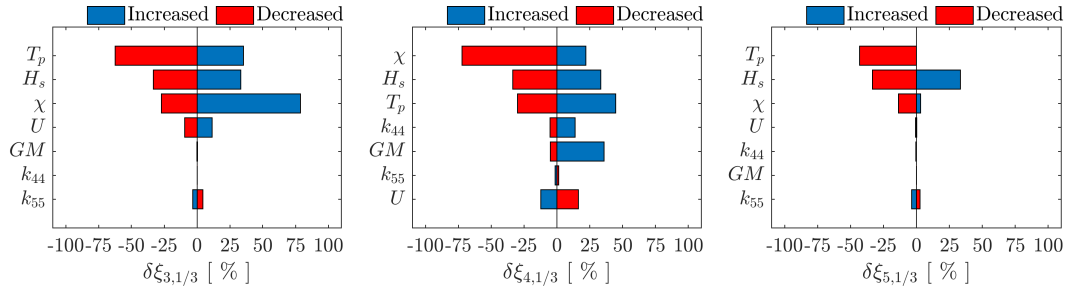

(a) Heave (b) Roll (c) Pitch

Figure 4.10: Significant amplitude sensitivity analysis results

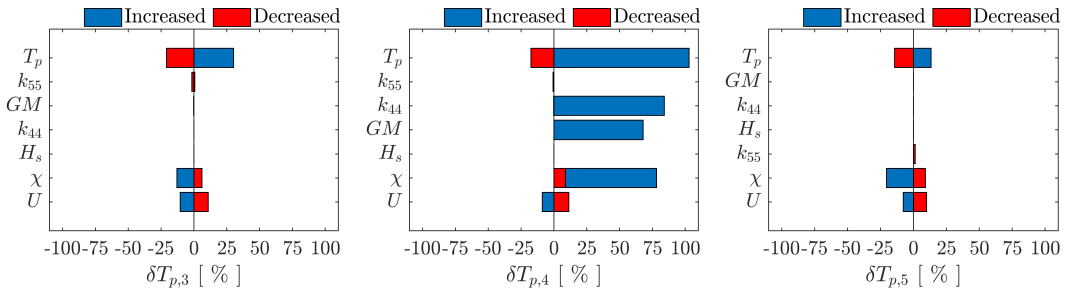

(a) Heave (b) Roll (c) Pitch

Figure 4.11: Peak period sensitivity analysis results

4.8 Conclusion

In this chapter, the measured motion responses of the SA Agulhas II and the prediction thereof in irregular seas were investigated. The results showed that heave and pitch can be predicted with reasonable accuracy using strip theory and the ITTC wave spectrum. However, some differences were highlighted in short waves with high frequencies and confused seas. Generally speaking, various discrepancies were observed for the roll response. It is recommended for future studies to investigate the effect of additional roll damping using semi-empirical methods, such as the Ikeda method.

Chapter 5

CFD investigation in head waves

5.1 Introduction

CFD has been identified as an effective tool to investigate seakeeping aspects of the SA Agulhas II. This technique will be used to investigate calm water and regular head wave conditions. More specifically, the heave, pitch motion and added resistance due to waves will be evaluated.

The CFD software package FINE^{TM}/Marine Version 8.2, by NUMECA^{TM} International, was used to conduct the CFD study. Three software packages are included within the FINE^{TM}/Marine package: the HEXPRESS^{TM} mesh generator, ISIS-CFD flow solver and CFView^{TM} flow visualizer.

All simulations presented in this study were performed using the University of Stellenbosch HPC1 (Rhasatsha, 2020).

5.2 Investigated conditions

For this research, the flow is considered to be turbulent with the Reynolds number, Re, of the order 10^8 for full-scale simulations (ITTC, 2014*a*). As it is customary practise in the CFD analysis of ships, the Froude number, Fn, is used to express the speed of the vessel. Re and Fn are defined as follows ITTC (2014*a*):

$$Re = \frac{\rho U L_{PP}}{\mu}; \quad Fn = \frac{U}{\sqrt{g L_{PP}}} \tag{5.1}$$

CFD simulations were performed using the 3D geometry described in Section 3.1.1 and at the design conditions of the vessel (see Table 3.1).

The present study did not have access to calm water resistance, sinkage and trim results of the SA Agulhas II. It was deemed worthwhile to investigate these responses to establish a benchmark of the ship's performance, i.e the calm water resistance, sinkage and trim curves (Ahmad and Adnan, 2014). In addition, calm water resistance is required to give insight into the added

resistance of the vessel due to waves (Tezdogan *et al.*, 2015). The calm water responses were investigated at seven different speeds ranging from 6 kn to 18 kn (Fn ranging from 0.09 to 0.27) with speed increments of 2 kn.

Seakeeping simulations were performed at fifteen different wave conditions, as listed in Table 5.1. These conditions were chosen based on the ratio of the wave to ship length (i.e. λ/L_{PP}), which ranged between 0.67 and 2. The wave steepness, which is defined as the ratio of wave height to length (H_w/λ), was chosen as 1/60. This corresponds to the values presented by Tezdogan *et al.* (2015) and Simonsen *et al.* (2013). Furthermore, three speeds were investigated: a reduced speed of 10 kn, the service speed of 14 kn, and a maximum speed of 18 kn.

Resonance is expected to occur when the encounter frequency, f_e, is close to the natural frequency of the ship motion, f_n (Tezdogan *et al.*, 2015). The estimated heave and pitch natural frequencies, presented in Chapter 3, are $f_{n3} \approx 0.149$ Hz and $f_{n5} \approx 0.112$ Hz, respectively. The estimated natural frequencies were also in fair agreement with the RAOs calculated using strip theory. Therefore, the largest amplitude motions are expected to occur when $\lambda/L_{PP} = 1.33$ to 1.67.

Table 5.1: Summary of the wave conditions for CFD seakeeping study.

Case no.	U [kn]	Fn	H_w [m]	λ [m]	f_e [Hz]	T_e [s]	λ/L_{PP}
1.1	10	0.15	1.34	80.7	0.203	4.93	0.67
1.2			2.01	121	0.156	6.41	1.00
1.3			2.69	162	0.130	7.69	1.33
1.4			3.36	202	0.113	8.85	1.67
1.5			4.03	242	0.102	9.80	2.00
2.1	14	0.21	1.34	80.7	0.228	4.39	0.67
2.2			2.01	121	0.173	5.78	1.00
2.3			2.69	161	0.143	6.99	1.33
2.4			3.36	202	0.124	8.07	1.67
2.5			4.03	242	0.110	9.09	2.00
3.1	18	0.27	1.34	80.7	0.254	3.94	0.67
3.2			2.01	121	0.190	5.26	1.00
3.3			2.69	162	0.156	6.41	1.33
3.4			3.36	202	0.134	7.46	1.67
3.5			4.03	242	0.119	8.40	2.00

5.3 Numerical modelling

The following section discusses the governing equations solved by the ISIS-CFD flow solver, free-surface and turbulence modelling, as well as the discretisation methods of the RANS equations.

5.3.1 Governing equations

As discussed in Section 2.2, the Navier-Stokes equations cannot be solved analytically and DNS requires significant computational effort. Therefore, CFD methods solve the unsteady RANS equations numerically.

The equations for continuity, momentum and the volume fraction conservation for incompressible flow of a viscous fluid under isothermal conditions are expressed in the generalized form of Gauss' theorem according to Centrale Nantes (2020*a*) as follows:

$$\frac{\partial}{\partial t}\int_V \rho dV + \int_S \rho(\boldsymbol{v}-\boldsymbol{v}_d)\cdot\mathbf{n}dS = 0 \tag{5.2}$$

$$\frac{\partial}{\partial t}\int_V \rho\boldsymbol{v}_i dV + \int_S \rho v_i(\boldsymbol{v}-\boldsymbol{v}_d)\cdot\mathbf{n}dS = \int_S(\tau_{ij}I_j - pI_i)\cdot\mathbf{n}dS + \int_V \rho g_i dV \tag{5.3}$$

$$\frac{\partial}{\partial t}\int_V c_i dV + \int_S c_i(\boldsymbol{v}-\boldsymbol{v}_d)\cdot\mathbf{n}dS = 0 \tag{5.4}$$

where V is the control volume bounded by a closed surface S with a normal vector $\mathbf{n}$ directed outward. The velocity normal to S is denoted by $\boldsymbol{v}_d$, while velocity and pressure fields are represented by $\boldsymbol{v}$ and p, respectively; v_i is the average velocity on the x_i axis direction. τ_{ij} and g_i are components of the viscous stress tensor and gravity vector, respectively. I_i and I_j are direction vectors. c_i is the volume fraction for a fluid i where $c_i = 1$ and $c_i = 0$ indicates the presence or the absence of i^{th} fluid, respectively. The volume fraction between 0 and 1 indicates the presence of fluid mixture, where $c_i = 0.5$ describe the interface between air and water, also known as the free surface.

5.3.2 Free surface modelling

For multi-fluid flow, the free surface is modelled numerically by the Volume of Fluid approach. This approach considers air and water as a single fluid which is calculated at the same time (Chen *et al.*, 2015). The physical properties of viscosity, μ, and density, ρ, of the effective flow are obtained from the constituent fluids, i.e. μ_i, and density, ρ_i, and are calculated using c_i as follows:

$$\rho = \sum_i c_i\rho_i \qquad \mu = \sum_i c_i\mu_i \qquad \sum_i c_i = 1 \tag{5.5}$$

Therefore, Equation 5.4 can be solved for one fluid instead of two fluids (Guilmineau *et al.*, 2012), which increases numerical efficiency (Tezdogan *et al.*, 2015). A depiction of the free surface on the hull surface of the SA Agulhas II is given in Figure 5.1. A mass fraction value of 0.5 represents the free surface, i.e. 50 % air and 50 % water. The properties for water and air at 15 °C are used in all simulations and are given in Table 5.2.

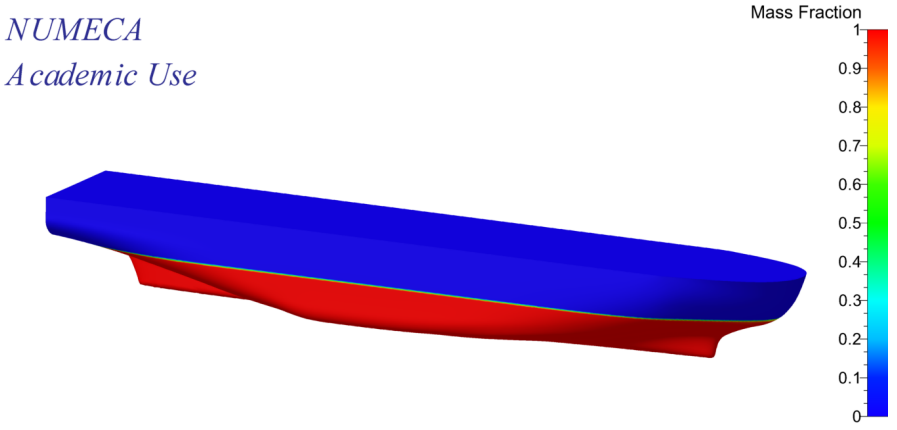

Figure 5.1: Free surface representation on the SA Agulhas II hull during a calm water simulation at 6 kn.

Table 5.2: Properties of air and water at 15 °C.

Fluid	Density [kg/m^3] ρ	Dynamic viscosity [Pa ·s] μ
Water	999.1	$1.137{\cdot}10^{-3}$
Air	1.2	$1.185{\cdot}10^{-6}$

5.3.3 Turbulence modelling

Turbulent flow is defined as the random and chaotic flow state that occurs in a fluid when the Reynolds number, Re, is above Re_{crit} (Versteeg and Malalasekera, 2007). To solve the RANS equations, the Reynolds stress tensor, τ_{ij}, is approximated by turbulence models (Schobeiri, 2010).

In this study turbulent flow is modelled by the Shear-Stress Transport (SST) $k-\omega$ turbulence model, where k is the turbulent kinetic energy per unit mass and ω is the specific dissipation rate.

This turbulence model has been used in many other marine CFD studies (Lagemann, 2019; Jin *et al.*, 2017; Bekhit and Lungu, 2019) and is the model

recommended by Centrale Nantes (2020*b*) for calm water and seakeeping applications. One drawback is that it increases the required CPU time by nearly 25 %, when compared to the $k-\epsilon$ turbulence model (Tezdogan *et al.*, 2015).

5.3.4 Discretisation methods

The unsteady RANS equations are solved numerically through the discretisation of the governing equations (Anderson, 1995). The ISIS-CFD solver uses the Finite Volume Method (FVM) to build the spatial discretisation of the transport equations (Centrale Nantes, 2020*a*).

Discretisation of the momentum and turbulence equations is through the AVLSMART scheme. This method is based on the third-order QUICK scheme (Vogt *et al.*, 2016). A higher order discretisation scheme is recommended to possibly capture the gradient of vorticity, which would disappear if lower order methods are used (Boonstra, 2019). Additionally, Andrun *et al.* (2018) conducted a comparative study of the influence that various discretisation schemes had on the calculated resistance of the Wigley hull. The authors documented that the results obtained using the AVLSMART scheme were in good agreement with EFD data.

The free surface in the multi-fluid domain is discretised by the Blended Reconstructed Interface Capturing Scheme (BRICS). This scheme is recommended by Centrale Nantes (2020*b*) to model multi-fluid flows.

Pressure-velocity coupling is achieved through the Rhie-Chow-SIMPLE-type method. This implies that in each time step the velocity field updates are calculated using the momentum conservation equation, Equation 5.3, while the pressure is calculated from the continuity equation, Equation 5.2, which is transformed into a pressure-correction equation. The water volume fraction, c_i, is calculated by the discretisation of the linear convection equation, Equation 5.4. It is calculated at each time step and is decoupled from the pressure and velocity updates (Guilmineau *et al.*, 2012).

The implicit scheme is applied for temporal discretisation. The second order three-level time scheme is utilized for time-accurate unsteady simulations (Deng *et al.*, 2010).

5.4 Computational setup

FINE^{TM}/Marine C-Wizard was used to establish a rapid computational setup according to the guidelines presented by Centrale Nantes (2020*b*). A description of the computational setup is given in the sections that follow.

5.4.1 Computational domain and boundary conditions

The 3D geometry of the SA Agulhas II was imported into a rectangular prism, which is referred to as the computational domain. Two computational domains were generated, a calm water and a seakeeping domain.

The seakeeping domain and its boundary conditions are shown in Figure 5.2. It is generated in terms of the reference length, L_{ref}, which is defined as $L_{ref} = \max(L_{PP}, \lambda)$. The resultant domain size is $7L_{ref} \times 2L_{ref} \times 6L_{ref}$. The calm domain size is defined in terms of the L_{OA} of the vessel, with an overall domain size $5.5L_{OA} \times 2L_{OA} \times 2.5L_{OA}$, which is applicable for calm water simulations when Fn is less than 1 (Centrale Nantes, 2020*b*). The locations of the boundary conditions for each domain are shown in Table 5.3.

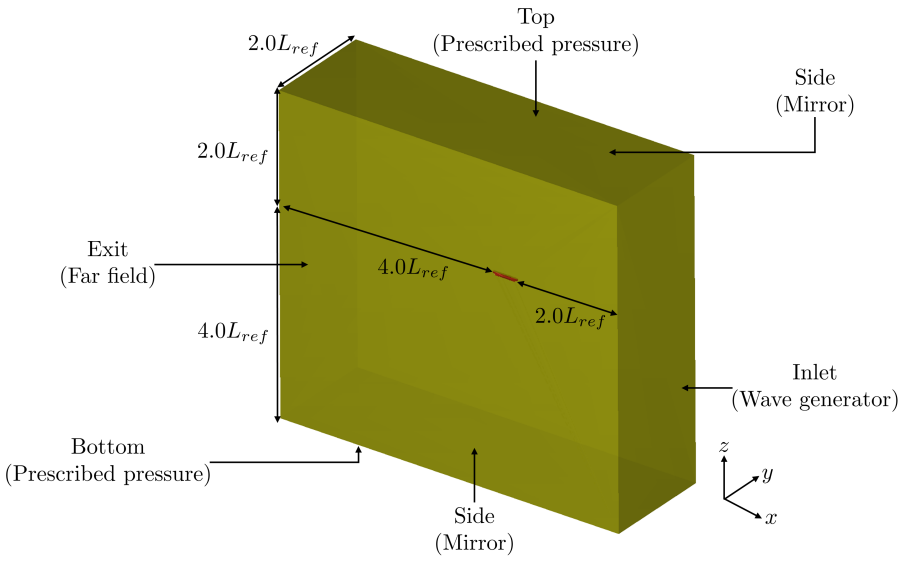

Figure 5.2: Domain for seakeeping simulations

Table 5.3: Location of boundary conditions.

Domain	Directions				
	Upstream	Downstream	Top	Bottom	Side
Calm water	$1.5L_{OA}$	$2L_{OA}$	$1L_{OA}$	$1.5L_{OA}$	$2L_{OA}$
Seakeeping	$2L_{ref}$	$4L_{ref}$	$2L_{ref}$	$4L_{ref}$	$2L_{ref}$

For both calm water and seakeeping simulations, half-body simulations are used. Therefore, the side boundary condition at $y = 0$ is set as a mirror boundary condition. This implies that the geometry and the flow is symmetric to the mirror plane. This method reduces the number of required cells and

computational cost. The inlet, outlet and side at $y = 2L_{OA}$ boundary conditions for calm water boundary conditions is set as far field with a constant zero velocity.

For seakeeping simulations, the mirror boundary condition is also applied at the side of $y = 2L_{ref}$ to eliminate numerical wave reflection (Bekhit and Lungu, 2019). The inlet boundary condition is set as wave generator, with it's direction of propagation in the x-direction towards the ship. Prescribed pressure with updated hydrostatic pressure is applied for the top and bottom boundary conditions. Therefore, the pressure values at these boundaries are set as $-\rho g(z(t)-z_0)$, which implies that it's magnitude will change according to the free surface position (Centrale Nantes, 2020*b*). Finally, for solid patches, i.e. the hull, skeg and transom surfaces, wall function boundary conditions were applied to capture the flow within the boundary layer. Shear stresses on the deck due to air flow are considered to be negligibly small compared to the other surfaces in water. Therefore, the slip boundary condition is applied to deck surface.

5.4.2 Mesh generation

An unstructured hexahedral mesh is generated using the automatic mesh generator, HEXPRESS^{TM} (NUMECA International, 2020*b*). The mesh generation process follows a top-down approach which is divided into five steps, as depicted in Figure5.3.

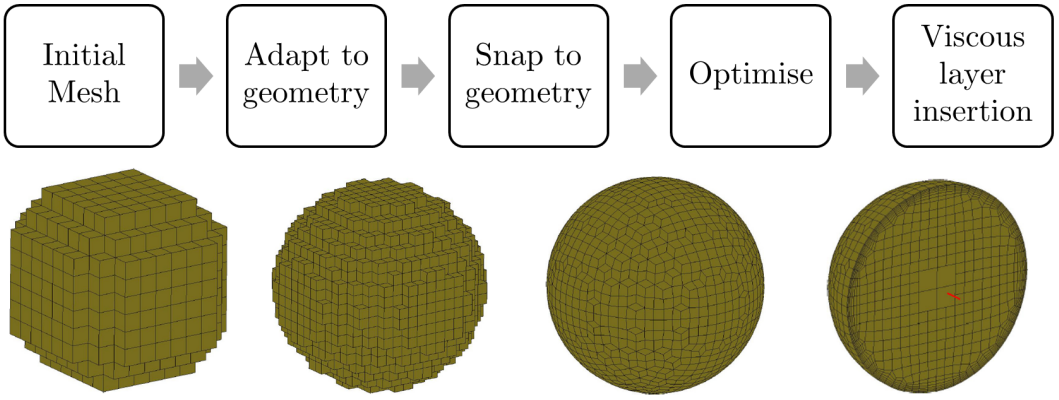

Figure 5.3: Mesh generation steps, adapted from NUMECA International (2020*b*).

First an initial cartesian mesh is generated by subdividing the computational domain into rectangular cells.

Thereafter, the mesh is adapted to the geometry of the vessel. During this step, the initial mesh is refined to more accurately represent the geometry of the vessel. Successive refinements are applied to curves, surfaces and boxes

surrounding the solid patches of the vessel and the free surface. Additional refinements are inserted at the transom region to ensure that detached flow is accurately captured. Surface refinements are applied to the hull, skeg, transom and deck surfaces. A trimming step is included to remove cells intersecting or located outside of the geometry.

For seakeeping simulations, two refinement boxes are created around the free-surface. The first box refines the free surface upstream and $1L_{ref}$ downstream of the vessel. The ITTC (2011) recommends at least 40 grid points per wave length. Therefore, the cell sizes are specified as: $\Delta x = \lambda/50$, $\Delta y = 4\Delta x$ and $\Delta z = H_w/10$. The box refinement in the z-direction extends by $1.5H_w$ above and below the free surface. The second refinement box extends $3L_{ref}$ downstream and refines a numerical wave damping zone. These cells are slightly coarser in the x-and y-direction, but has a similar depth in the z-direction.

The next step in the mesh generation process is snapping the mesh to the geometry of the vessel. During this step the mesh is projected to the surface of the geometry. Afterwards, an optimisation step is included to remove any concave, negative and non-orthogonal cells. This step ensures that a high quality mesh is generated.

The final step in the mesh generation process is the insertion of refined cells in order to model the viscous layer at the solid walls of the vessel. When turbulent flow is modelled, it is required to place the first grid point, y_{wall}, within a certain range from a solid wall. The velocity of the fluid at the wall is zero. Therefore, a boundary layer develops close to the wall which contains high velocity gradients in the direction normal to the wall. A sufficient number of grid points should be included inside the boundary layer to properly capture the high gradients. The value of y_{wall} is based on the dimensionless distance from the wall, y^+. For the $k-\omega$ SST turbulence model the recommended value of y^+ is between 30 and 300 (Centrale Nantes, 2020*b*). Therefore, the first grid point is inserted based on a y^+ value of 60 with an expansion ratio of 1.2. Figure 5.4 depicts an example of the y^+ contours on the vessel when the bow is submerged in a wave crest during Case 2.3.

Two different computational meshes were generated for calm water resistance and seakeeping simulations. The mesh generation process for calm water simulations followed a similar approach, except that refinement boxes are not added to refine the free surface. Instead, an internal free surface is generated which is refined to reach a target cell size of $L_{OA}/1000$ in the z-direction and an expansion ratio of 128 in the x- and y-directions (Centrale Nantes, 2020*b*).

The resultant mesh characteristics are listed in Table 5.4. It should be noted that the exact number of cells for the seakeeping conditions are shown for the wave condition in Case 4. The number of cells varied between 2 to 3.9 million for the different wave simulations. For reference, the resultant seakeeping mesh is shown in Figure 5.5.

Table 5.4: Mesh characteristics for calm water and seakeeping conditions

Mesh characteristics	Calm water conditions	Seakeeping conditions
Number of cells mesh	1 167 431	2 331 220

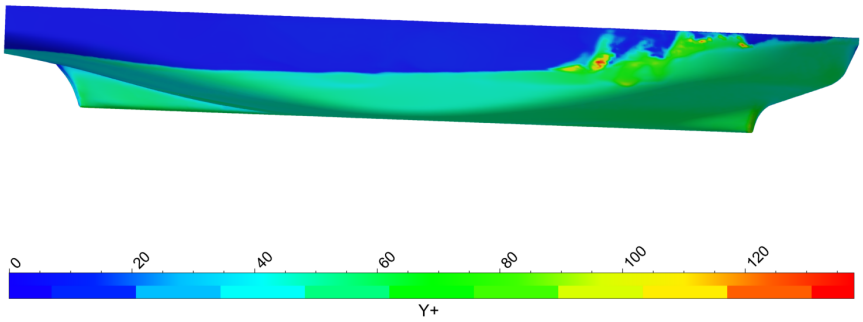

Figure 5.4: y^+ contours on the surface of the ship during Case 2.3.

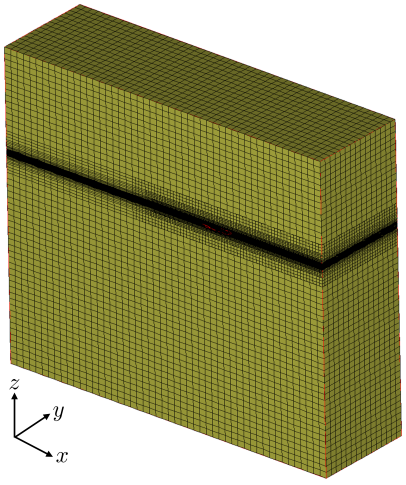

(a) A general 3D view

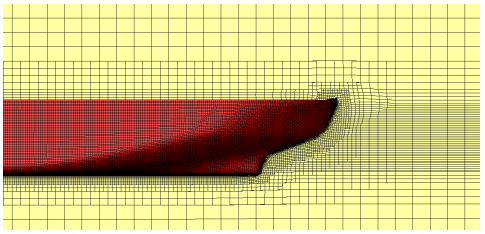

(b) Detailed view of the bow area

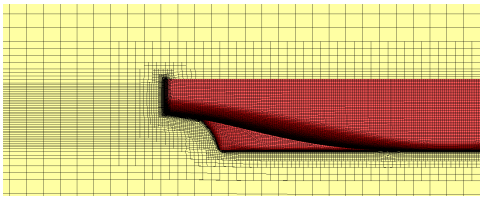

(c) Detailed view of the stern area

Figure 5.5: Computational mesh

5.4.3 Wave generation and damping zones

As discussed previously, the inlet boundary condition is set as a wave generator. The generated waves can be regular or irregular. However, the recommended simulation period for irregular seas is half an hour to an hour for full-scale simulations (Centrale Nantes, 2020*b*). This results in significant computational cost and time (Storsul, 2019). Therefore, this study considers regular waves.

The generation of regular waves is based on Stokes wave theory (Centrale Nantes, 2020*b*). First-order Stokes waves are regular Airy waves. Second- and third-order Stokes waves are defined as non-linear waves. Higher-order

waves are expected to resemble a real wave more closely than first-order waves (Tezdogan *et al.*, 2015). Therefore, third-order waves are chosen for all the seakeeping simulations.

The amplitude of the incident wave was measured by a numerical wave probe 1λ upstream of the vessel, as shown in Figure 5.6. Based on the recommendations in Centrale Nantes (2020*b*), a numerical damping region is inserted $1L_{ref}$ downstream of the vessel and extends $3L_{ref}$ to the outlet of the domain. This wave damping region acts as a sponge layer that damps free surface waves to avoid undesired wave reflection (Bekhit and Lungu, 2019).

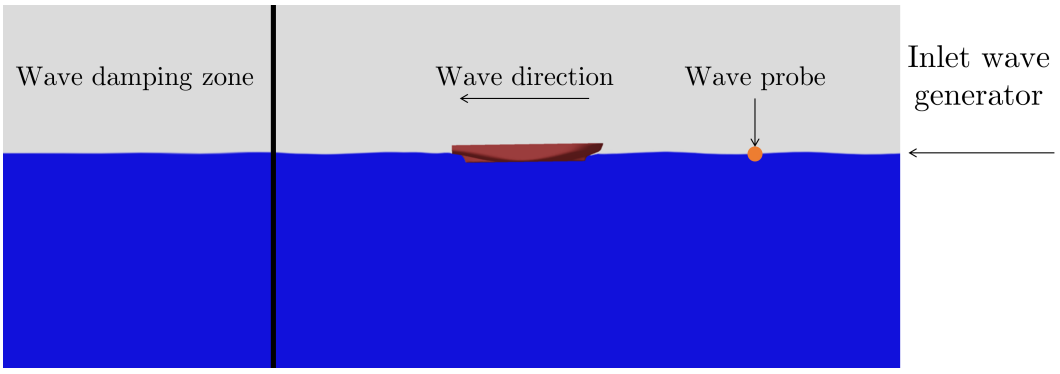

Figure 5.6: Side view of wave probe and wave damping zone.

5.4.4 Ship motion

The Galilean reference frame is used by FINE^{TM}/Marine to define the motion of the vessel, as discussed in Section 2.4.1. The motion of a ship is solved through Newton's equation of motion (D'Aure *et al.*, 2015).

For the present study, the heave and pitch motion of the vessel are solved, while sway, roll and yaw motion are restricted. The surge motion is imposed with a half-sinusoidal ramp function. This entails that the vessel will accelerate in 1 s from an initial velocity of 0 m/s to a target velocity with a linear ramp. Thereafter, the speed remains constant. The half-sinusoidal ramp function, $\alpha(t)$, is expressed as follows (Chen *et al.*, 2015):

$$\alpha(t) = \begin{cases} 0.5\left[1 - 0.5\cos\left(\frac{t}{T}\pi\right)\right] & t \leq T \\ 1 & t > 0.T \end{cases} \tag{5.6}$$

where T represents the ramp interval.

5.4.5 Choice of time step

The Courant-Friedrichs-Lewy (CFL) number is defined as the ratio of the physical time step (Δt) to the mesh convection time scale and it relates the

mesh cell size (Δx) to the mesh flow speed (U) as follows (Tezdogan *et al.*, 2015):

$$CFL = \frac{U\Delta t}{\Delta x} \tag{5.7}$$

In order to ensure numerical stability, it is recommended that the CFL number be less than or equal to 1 (Tezdogan *et al.*, 2015). However, this criteria is less demanding for implicit solvers, where the CFL can increase to approximately 10 without stability issues (Boonstra, 2019).

For calm water resistance simulations, a time step size equal to $\Delta t = 0.005(L_{OA}/V_{ref})$ was chosen. During each time step, five non-linear iterations were performed, as recommended by Centrale Nantes (2020*b*).

For seakeeping simulations in waves, the ITTC (2014*a*) recommends at least 100 time steps per wave encounter period, while Centrale Nantes (2020*b*) recommends 200. Therefore, 200 time steps per wave encounter period with 18 non-linear iterations per time step was specified. Furthermore, a convergence criteria of four orders of magnitude was specified and simulations were performed until the vessel encountered 15 wave periods.

5.5 Post-processing formulations

This section describes the post processing formulations used to evaluate the unsteady time series following methods presented by Tezdogan *et al.* (2015) and Jin *et al.* (2017).

The unsteady time series, $\varphi(t)$, of the forces and motion due to waves were analysed with a Fourier Series (FS) which is represented as follows:

$$\varphi(t) = \varphi_0 + \sum_{n=1}^{N} \varphi_n \cdot \cos(2\pi f_e n t + \gamma_n),\ n = 1, 2, 3... \tag{5.8}$$

where φ_n is the n^{th} harmonic and γ_n is the corresponding phase which are calculated as follows:

$$\varphi_n = \sqrt{a_n^2 + b_n^2} \tag{5.9}$$

$$\gamma_n = \arctan(\frac{b_n}{a_n}) \tag{5.10}$$

in which,

$$a_n = \frac{2}{T}\int_0^T \varphi(t)\cos(2\pi f_e n t)dt \tag{5.11}$$

$$b_n = -\frac{2}{T}\int_0^T \varphi(t)\sin(2\pi f_e n t)dt \tag{5.12}$$

In Equations 5.11 and 5.12, T is defined as the wave encounter period. The 0^{th} harmonic amplitude, φ_0, is the average value of the time series $\varphi(t)$, which is expressed as follows:

$$\varphi_0 = \frac{1}{T}\int_0^T \varphi(t)dt \tag{5.13}$$

The 1^{st} harmonic, φ_1, refers to the linear term of the time series. The 0^{th} and 1^{st} order harmonics are of particular interest, since these quantities are used to calculate the RAOs and the added resistance. However, for resistance in waves, it is worth noting that 2^{nd} and 3^{rd} order components may make up to 50 % and 15 % of the 1^{st} order component (Simonsen *et al.*, 2013).

Simonsen *et al.* (2013) approximated the resistance force, motions and wave elevation with a 3^{rd} order FS. In this study, the FS is calculated using the `fit.m` function in MATLAB®. This function applies an 8th order approximation to a given time-series, from which the coefficients, a_n and b_n, can be obtained (Lagemann, 2019). The FS was used to analyse the last 10 encountered waves, as recommended by the ITTC (2014*a*).

The total resistance is expressed in dimensionless form by the total resistance coefficient, C_T, as follows:

$$C_T = \frac{F_{x0}}{(1/2)\rho U^2 S} \tag{5.14}$$

where, F_{x0} is the 0^{th} harmonic of the drag force in the x-direction and S is the wetted surface area of the vessel.

The added wave resistance coefficient, C_{aw}, is calculated by subtracting the calm water resistance force, $F_{x,calm}$, from the 0^{th} harmonic amplitude of the resistance force in waves, $F_{x,waves}$, at the same ship speed as follows:

$$C_{aw} = \frac{(F_{x,waves} - F_{x,calm})}{\rho g \zeta_{I1}^2 B_{WL}/Lpp} \tag{5.15}$$

The 1^{st} harmonic amplitude of the FS is used to calculate the amplitude of the heave and pitch RAOs (Jin *et al.*, 2017):

$$A_i = \frac{\xi_{i1}}{\zeta_{I1}} \tag{5.16}$$

where ξ_{i1} $(i = 3, 5)$ is the 1^{st} harmonic amplitude heave and pitch motion components, and ζ_{I1} represents the 1^{st} harmonic amplitude of the incident wave. The phase difference between the incident wave and the motion is calculated by means of (Simonsen *et al.*, 2013):

$$\gamma_{LCG} = \gamma_{\zeta_{I1}} - 2\pi\frac{D}{\lambda} \tag{5.17}$$

where $\gamma_{\zeta_{I1}}$ is the phase of the 1^{st} harmonic amplitude of the incident wave and D is the distance between the LCG of the vessel and the numerical wave probe.

Thereafter, the phase relation between the motion and wave is calculated as follows:

$$\gamma_i = \gamma_{LCG} - \gamma_{\xi_{I1}} \tag{5.18}$$

where $\gamma_{\xi_{I1}}$ is the phase of the 1st harmonic amplitude of the motion response.

5.6 Verification and Validation study

A Verification and Validation (V&V) study was conducted using the KCS. The methodology and results of the V&V are presented in Appendix D. A brief summary of the results obtained are discussed below.

The verification study consisted of a grid size and time step size dependency study to evaluate the numerical and simulation uncertainties. The CFD simulations were validated by comparing CFD results of heave, pitch and resistance with experimental data presented by (Simonsen *et al.*, 2013). The validation uncertainty levels for the heave and pitch RAOs, and the total resistance coefficient were calculated as 7.88 %, 6.99 % and 6.09 %, respectively. Furthermore, the comparative errors, E, between the experimental data and CFD simulation results are presented. For heave and pitch RAOs, E ranged from 0.45 % to 9.93 %. For the 0th harmonic amplitude of resistance coefficient, the calculated E ranged from -3.66 % to 9.70 %. Finally, for the added wave resistance coefficient, E ranged from -8.03 % to 14.34 %. Overall, the results were in good agreement with experimental data and consistent with CFD results presented in various other studies. Therefore, confidence is achieved in the simulation results.

5.7 Calm water results

In order to evaluate the added resistance of the SA Agulhas II, it is first required to calculate the calm water resistance. As mentioned before, the calm water simulations were performed at seven different speeds ranging from $Fn =$ 0.09 to 0.27. It should be noted that the resistance results obtained for $Fn = 0.15, 0.21$ and 0.27 are of particular interest, since these results are used to evaluate the added resistance in waves.

The results obtained from the CFD simulations are presented in Table 5.5 and Figure 5.7. Notice that a negative sinkage refers to the lowering of the ship's position in water (Pérez-Rojas *et al.*, 2019), while a negative trim is defined as bow down (Castiglione *et al.*, 2011).

In Figure 5.7a, it is clear that the resistance force, F_x, increases exponentially as the ship speed, U, increases. It is observed that the resistance coefficient curve, shown in Figure 5.7b, is slightly flatter, especially between

$Fn = 0.09$ and 0.15. Thereafter, it is seen that the magnitude increases significantly. Both sinkage and trim, $\xi_{3,0}$ and $\xi_{5,0}$, shown in Figures 5.7c and 5.7d, decrease as ship speed increases.

Table 5.5: Calm water simulation results of the SA Agulhas II

Fn	Re	$F_{x,T}$ [N]	S [m^2]	$C_T \times 10^{-3}$	$\xi_{3,0}$ [m]	$\xi_{5,0}$ [deg]
0.09	2.97×10^8	44402	3638	2.56	-0.03	-0.011
0.12	3.95×10^8	77615	3660	2.52	-0.05	-0.021
0.15	4.94×10^8	122418	3680	2.55	-0.08	-0.036
0.18	5.93×10^8	186797	3698	2.69	-0.11	-0.053
0.21	6.92×10^8	277624	3719	2.95	-0.16	-0.071
0.24	7.91×10^8	405006	3745	3.29	-0.21	-0.086
0.27	8.90×10^8	602451	3775	3.87	-0.27	-0.104

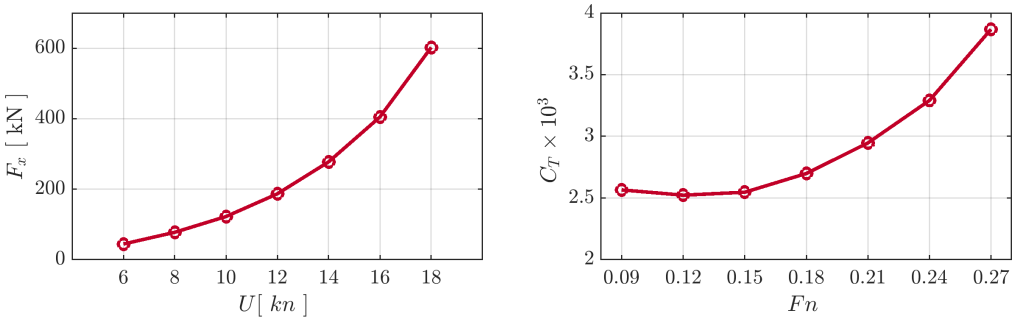

(a) Drag resistance

(b) Resistance coefficient

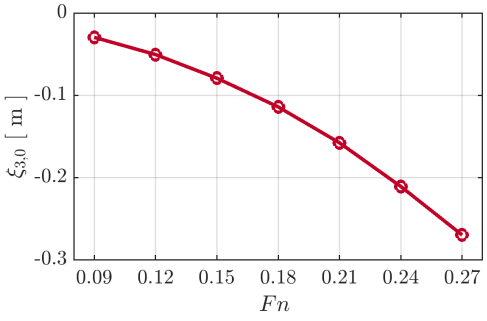

(c) Sinkage

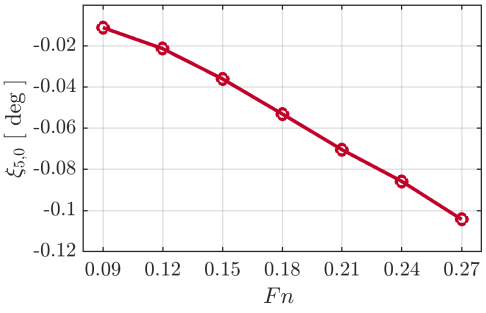

(d) Trim

Figure 5.7: CFD simulation results for the SA Agulhas II in calm water

Figure 5.8 represents the Kelvin wave pattern generated by the hull, as well as the hydrodynamic pressure on the hull for $Fn = 0.15$ and 0.27. These illustrations give valuable insight to gain better understanding of the relationship between the resistance, sinkage and trim curves. At $Fn = 0.27$, when the

resistance, sinkage and trim is the largest, noticeable crests and troughs can be observed to the sides of the ship. As a result of the ship's speeds, a negative hydrodynamic pressure acts upon the hull surface, as shown in Figure 5.8d. This subsequently leads to wave troughs on the free surface, which is presented in Figure 5.8b. Castiglione *et al.* (2011) refers to this negative pressure as suction pressure. The high suction pressures lead to negative hydrodynamics forces acting on the COG of the vessel, which increases the resistance and sinkage. Although it is not particularly evident, the trim motion arises from the net pressure difference between the bow and stern. For a more significant example of this, see Castiglione *et al.* (2011) who investigated a high-speed catamaran. At $Fn = 0.15$, the wave pattern observed is much smaller, and the suction pressure decreases. Therefore, the resistance, sinkage and trim is smaller compared to $Fn = 0.27$.

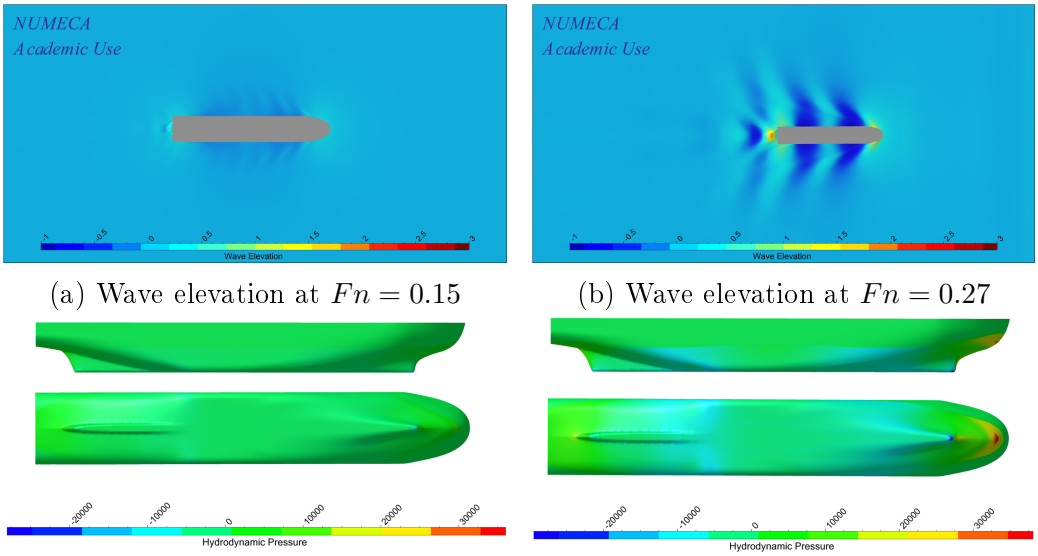

(a) Wave elevation at $Fn = 0.15$ (b) Wave elevation at $Fn = 0.27$

(c) Hydrodynamic pressure at $Fn = 0.15$ (d) Hydrodynamic pressure at $Fn = 0.27$

Figure 5.8: Wave elevation and hydrodynamic pressure distribution on the hull surface in calm water conditions

5.8 Seakeeping results

5.8.1 Discussion of time series motion and forces

In order to gain insight into the seakeeping behaviour of the SA Agulhas II in regular head waves, time series simulation results of the incident wave elevation, the wave-induced motion and drag forces for Cases 1.2, 2.3 and 3.5 are presented in this section. In addition to time series results, the free surface

coloured with wave elevation for four quarter periods are presented for visualisation purposes. These illustrations are also helpful to gain insight into the wave pattern around the ship.

As mentioned before, an 8^{th} order FS was used to analyse the last 10 wave encounters of the unsteady time series results obtained from CFD. An example of the FS approximation can be seen in Figure E.1 in Appendix E.1.

The incoming wave elevation was measured by a numerical wave probe. The specified and measured amplitudes for the three cases are shown in Table 5.6. The measured amplitude differs slightly from the specified amplitude. It was noticed that Tezdogan *et al.* (2015) applied fifth-order Stokes waves and found a difference of -3.20 % between the specified and measured amplitude. Therefore, the slight increase for the present study may be considered acceptable with the current mesh and time step size. For consistency, it was decided to use the specified wave amplitude to calculate the RAO amplitudes and added wave resistance coefficient.

Table 5.6: Specified and measured wave amplitudes

	Case 1.2	Case 2.3	Case 3.5
Specified	1.019	1.347	2.021
Measured	1.030	1.354	2.023
% Difference	1.079	0.520	0.099

In Case 1.2, shown in Figure 5.9−5.10, the wave length is equal to the ship length. At $t/T_e = 0$, the wave crest is slightly behind the LCG of the vessel, while the heave motion is at a peak. This implies that the heave motion is out of phase with the incoming wave elevation. It is also observed that the amplitude of the heave motion is smaller than that of the wave elevation. In short wave lengths and at high encounter frequencies, the motion of the ship is limited (Judge, 2019). Consequently this leads to reduced added resistance. As the waves move along the hull, the pitch motion increases, i.e. the vessel starts inclining downwards. At $t/T_e = 0.5$, the peak pitch motion occurs. At this time, the vessel's bow starts encountering the next wave and slightly dips into the water. Hence, the drag force shows non-linear behaviour. At $t/T_e = 0.75$, the vessel starts pitching upwards, the heave motion increases and the vessel starts travelling up the next wave.

Figures 5.11−5.12 show the results obtained for Case 2.3. In this case, it is observed that the encounter frequency, $f_e = 0.143$, of the vessel is close to its estimated heave and pitch natural frequencies, f_{n3} and f_{n5}. This implies that the relative motion between the ship and the wave is large, which causes an increase in added resistance (Castiglione *et al.*, 2011). The fact that the bow motion is opposite to the wave amplitude also leads to an increase in added resistance (Seo *et al.*, 2017). At $t/T_e = 0$, both the stern and the

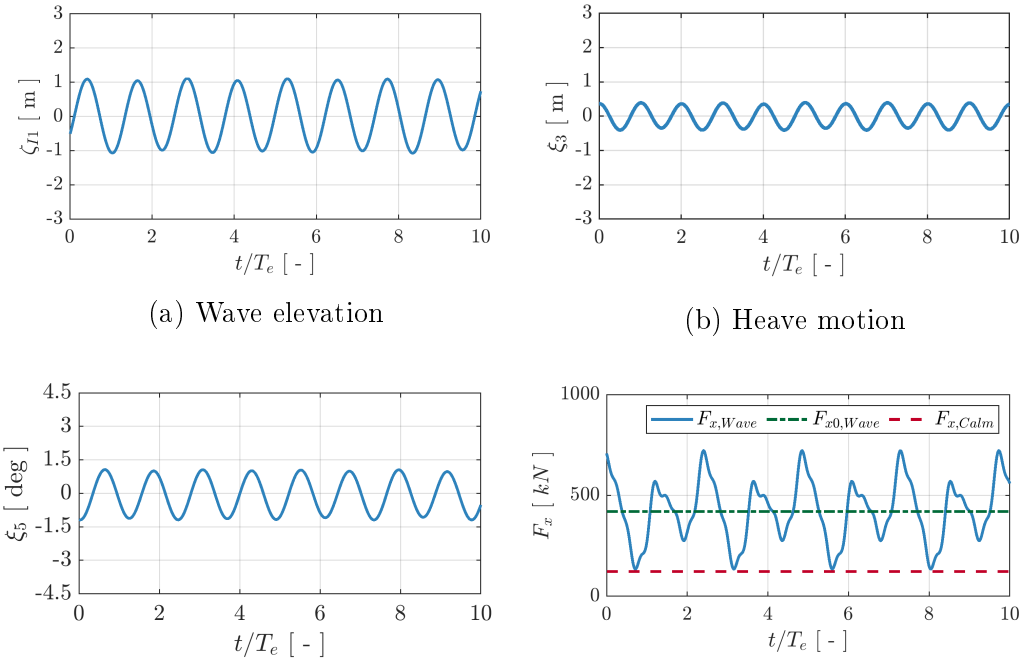

(a) Wave elevation

(b) Heave motion

(c) Pitch motion

(d) Drag force

Figure 5.9: Time series results for Case 1.2

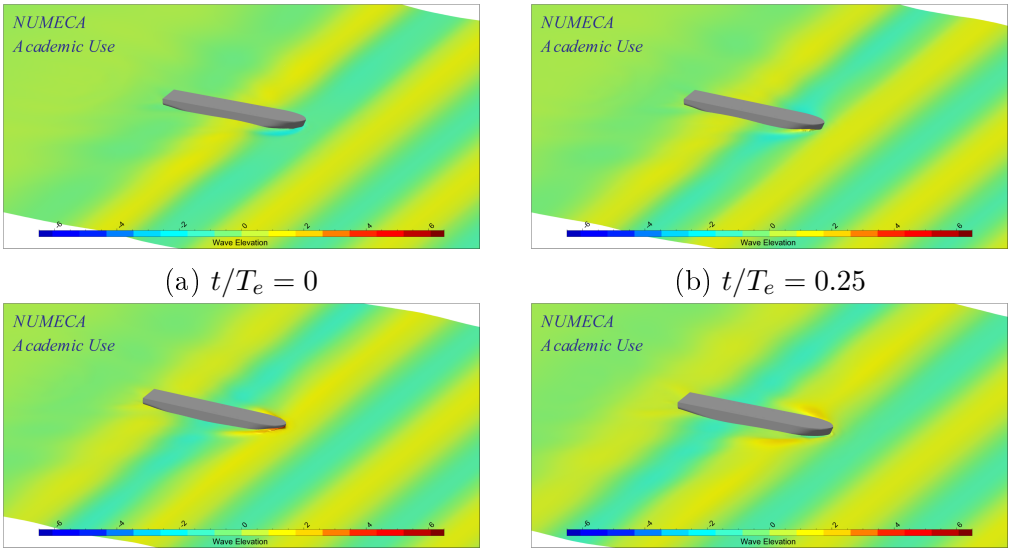

(a) $t/T_e = 0$

(b) $t/T_e = 0.25$

(c) $t/T_e = 0.5$

(d) $t/T_e = 0.75$

Figure 5.10: Free surface coloured with wave elevation for Case 1.2

bow of the vessel are on a wave crest and the midship "hangs" in the wave through. The vessel's pitch motion is at a peak, which causes the bow of the vessel to be deeply submerged in the incoming wave. This subsequently

causes the bow flare of the ship to generate waves on the incoming wave. This was also observed by Simonsen *et al.* (2013) for the resonance condition of the KCS. The bow emerges from the water at $t/T_e = 0.25$ and the vessel starts travelling up the incoming wave. In addition, it is also observed that heave motion is out of phase with the wave elevation. When $t/T_e = 0.5$, the wave crest is approximately at the LCG of the vessel, and the bow is almost completely emerged out of the water. Thereafter, at $t/T_e = 0.75$, the ship starts pitching downwards and dives into the through which generates waves at the bow shoulder region.

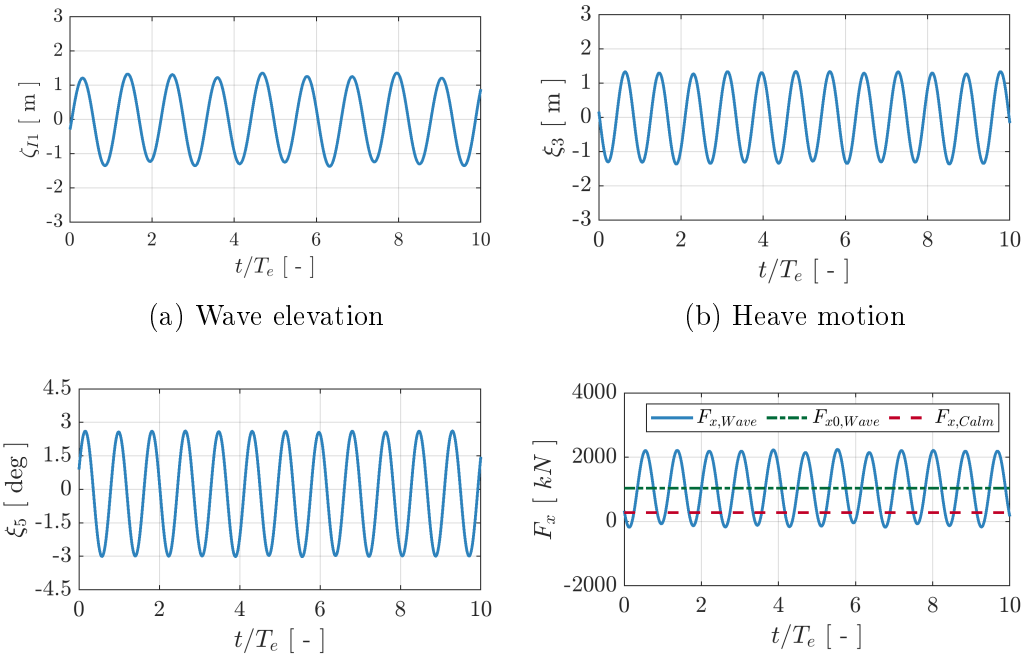

(a) Wave elevation

(b) Heave motion

(c) Pitch motion

(d) Drag force

Figure 5.11: Time series results for Case 2.3

In Case 3.5, shown in Figures 5.13−5.14, the vessel is travelling in relatively long waves. The drag force shows harmonic behaviour and the heave motion and wave elevation are almost synchronised. The peak pitch motion occurs approximately one quarter period after the wave crest has passed the LCG of the vessel. This implies that the pitch motion has a phase lead over the wave elevation, of approximately 90 degrees. Notice that the added resistance is less than that observed for Case 2.3. This is expected since the relative motion between the hull and waves is negligible (Castiglione *et al.*, 2011).

Generally speaking, it is observed that the phase difference between the drag force and heave motion is approximately 90 degrees. This means that the drag force increases as the vessel is travelling up the wave, or vice versa. It

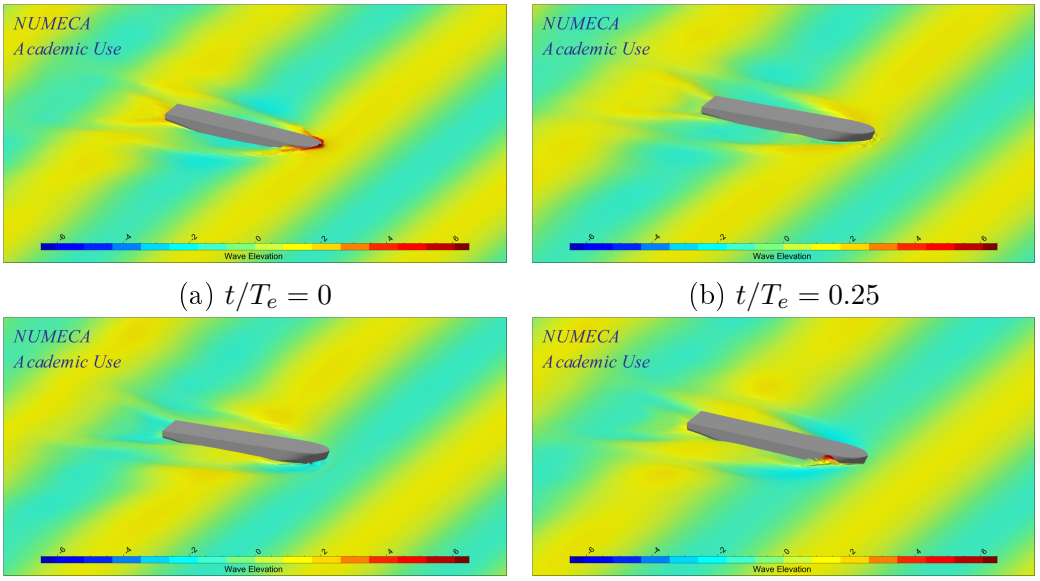

(a) $t/T_e = 0$ (b) $t/T_e = 0.25$

(c) $t/T_e = 0.5$ (d) $t/T_e = 0.75$

Figure 5.12: Free surface coloured with wave elevation for Case 2.3

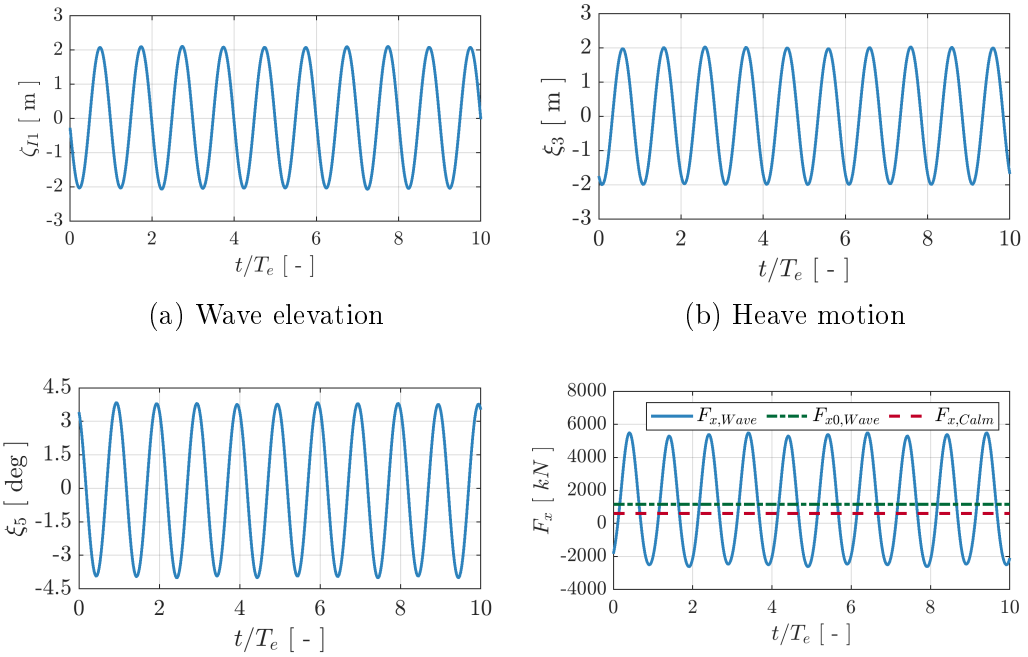

(a) Wave elevation (b) Heave motion

(c) Pitch motion (d) Drag force

Figure 5.13: Time series results for Case 3.5

is also seen that the phase difference decreases as the ratio of wave length to ship length increases. Similar results were presented by Chen *et al.* (2020).

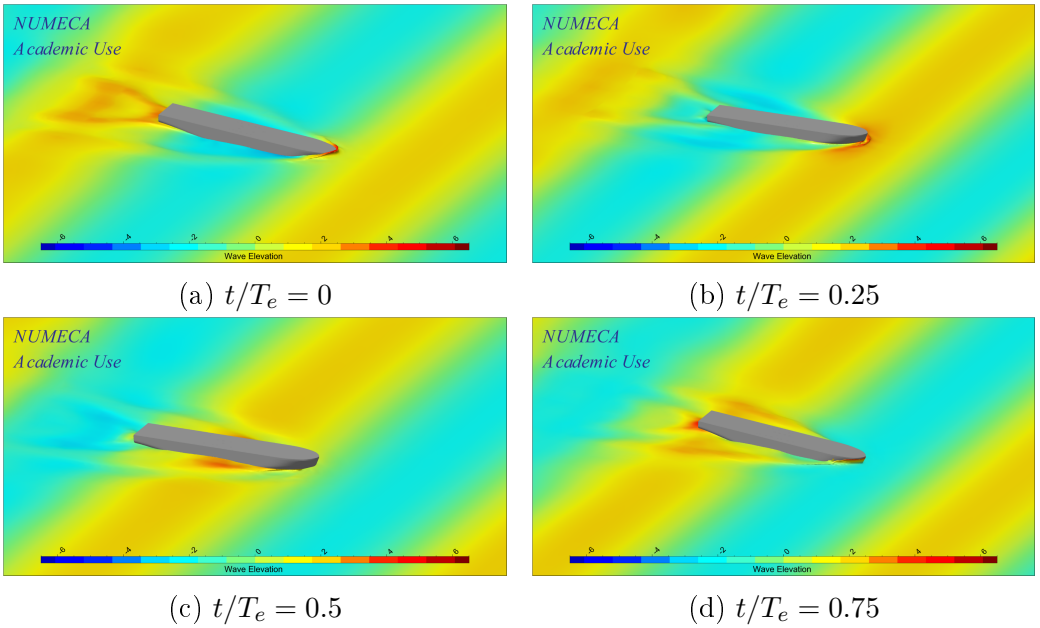

(a) $t/T_e = 0$ (b) $t/T_e = 0.25$

(c) $t/T_e = 0.5$ (d) $t/T_e = 0.75$

Figure 5.14: Free surface coloured with wave elevation for Case 3.5

5.8.2 Response Amplitude Operators

In this section, the RAO results obtained from the CFD program FINE^{TM}/Marine are presented and compared with results obtained from the strip theory program, PDSTRIP.

Figure 5.15 shows the amplitude and phase of the heave RAOs. The amplitudes of the heave motion, A_3, are fairly small in short waves and increase towards unity as the wave length increase. At $Fn = 0.21$, the maximum heave response occurs when $\lambda/L_{PP} = 1.33$. The absolute maximum heave response is seen at the highest speed, $Fn = 0.27$, when $\lambda/L_{PP} = 1.67$. It is interesting to observe that for both these cases, the maximum response occurs when the encounter frequency, f_e, is close to the estimated heave natural frequency, $f_{n3} \approx 0.149\,\text{Hz}$. This implies that the heave response is dependent on the wave length and the encounter frequency. This concurs with Simonsen *et al.* (2013), who investigated the response of the KCS at $Fn = 0.26$, 0.33 and 0.40 for wave lengths ranging from $\lambda/L_{PP} = 0.5$ to 2. Their results showed that the maximum heave response occurred at the highest speed and at a wave length longer than $\lambda/L_{PP} = 1.33$.

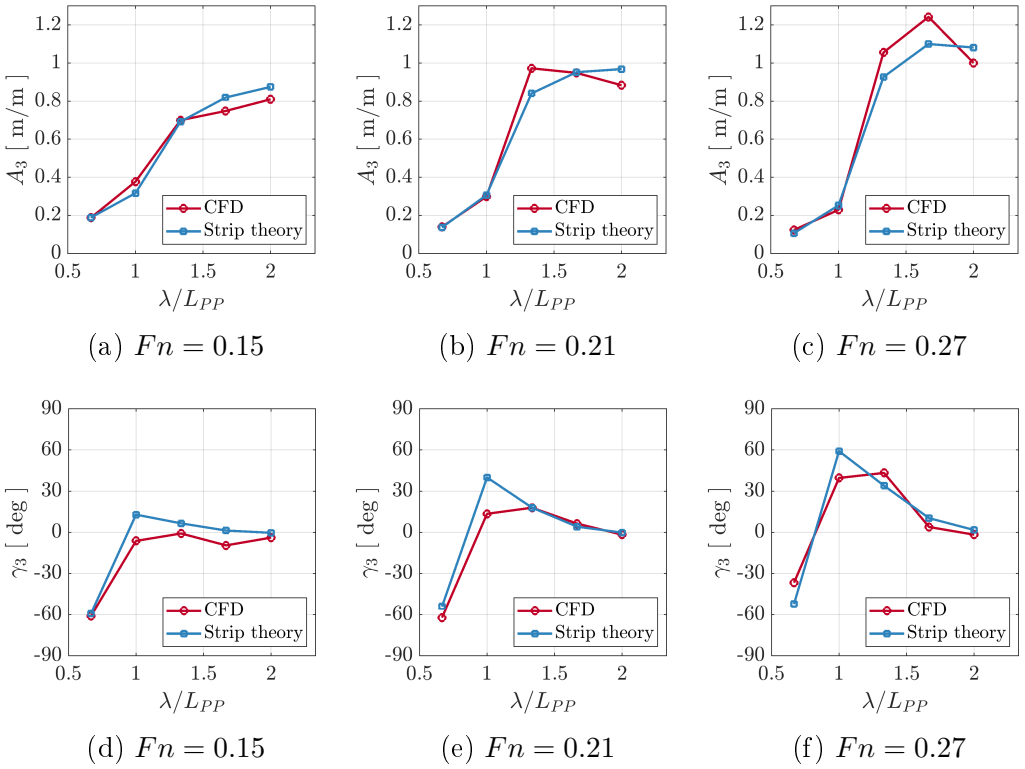

(a) $Fn = 0.15$ (b) $Fn = 0.21$ (c) $Fn = 0.27$

(d) $Fn = 0.15$ (e) $Fn = 0.21$ (f) $Fn = 0.27$

Figure 5.15: Heave RAO results: (a)-(c) amplitudes and (d)-(f) phases.

The calculated heave phase, γ_3, shows a typical trend observed in literature (Simonsen *et al.*, 2013; Castiglione *et al.*, 2011). As the ratio of the wave-to-ship length increases, the phase lag between the heave response and wave decreases towards zero. This is expected since the heave motion becomes synchronized with the incident wave in long waves (Castiglione *et al.*, 2011).

The pitch motion amplitude and phases are shown in Figures 5.16. Similar to heave motion, it is observed that amplitude of the pitch, A_5, is dependent on the wave length and the encounter frequency. For $Fn = 0.15$, the maximum pitch response is observed when $\lambda/L_{PP} = 1.33$. For the medium and high speed, $Fn = 0.21$ and 0.27, the maximum response is observed when $\lambda/L_{PP} = 1.67$. The maximum responses seem to occur at encounter frequencies, f_e, ranging between 0.124 to 0.134, which is slightly higher than the calculated pitch natural frequency, $f_{n5} \approx 0.112\,\text{Hz}$.

The pitch motion phases, γ_5, tends to go towards 90 degrees. This means that the maximum pitch motion response occurs one quarter period after the wave crest has passed the midship of the vessel. Once again this seems to be consistent with discussions in Simonsen *et al.* (2013) and Castiglione *et al.* (2011).

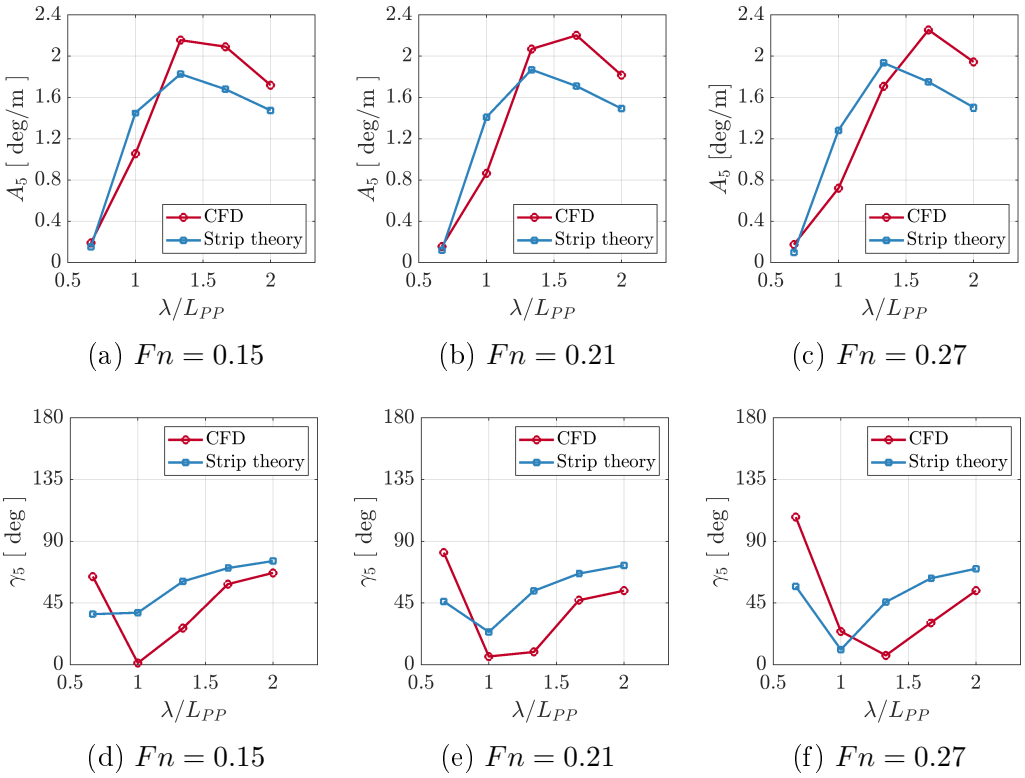

(a) $Fn = 0.15$ (b) $Fn = 0.21$ (c) $Fn = 0.27$

(d) $Fn = 0.15$ (e) $Fn = 0.21$ (f) $Fn = 0.27$

Figure 5.16: Pitch RAO results: (a)-(c) amplitudes (d)-(f) phases.

The heave and pitch RAO results obtained from CFD and strip theory are fairly similar for the lowest speed, $Fn = 0.15$. For heave motion some differences exist at higher speeds. More specifically, the motion amplitude at resonance is under predicted by strip theory. However, the phases are in good agreement and follow a similar trend. Similarly, the amplitude of the pitch motion obtained from strip theory is slightly under predicted. The reason for these differences can be ascribed to two factors. Firstly, in CFD the vessel encounters third-order Stokes wave, while strip theory uses first-order wave theory. Generally speaking, a higher order wave has a larger amplitude, sharper wave crest and flatter troughs, while first-order waves follow a sinusoidal profile (Centrale Nantes, 2020*b*). Secondly, strip theory programs are known to produce inferior results at higher speeds (Belga *et al.*, 2018). Nevertheless, strip theory is still considered to be a useful tool to conduct preliminary seakeeping studies at lower computational cost.

5.8.3 Added resistance in waves

The added resistance experienced is an important aspect of the seakeeping behaviour of ships in waves (Castiglione *et al.*, 2011). In Section 5.8.1, it has briefly been depicted and discussed how the resistance increases due to waves.

Figure 5.17a−5.17c illustrates a preliminary evaluation of the added resistance, where a comparison of the resistance coefficient in waves, $C_{T,waves}$, and in calm water, $C_{T,calm}$, is presented as a function of λ/L_{PP}.

The results show that the added resistance in waves is more notable at the lowest speed. At the higher speeds, resistance in calm water and head waves increases, the former more strongly. It is also observed that the peak increase in resistance is observed when the maximum motion response occurs, i.e. for $Fn = 0.15$ and $Fn = 0.21$ when $\lambda/L_{PP} = 1.33$; and for $Fn = 0.27$ when $\lambda/L_{PP} = 1.67$. This behaviour is consistent with literature. For example, Castiglione *et al.* (2011) noticed that the added resistance in waves for a catamaran is more significant at low speeds and is negligible for higher speeds.

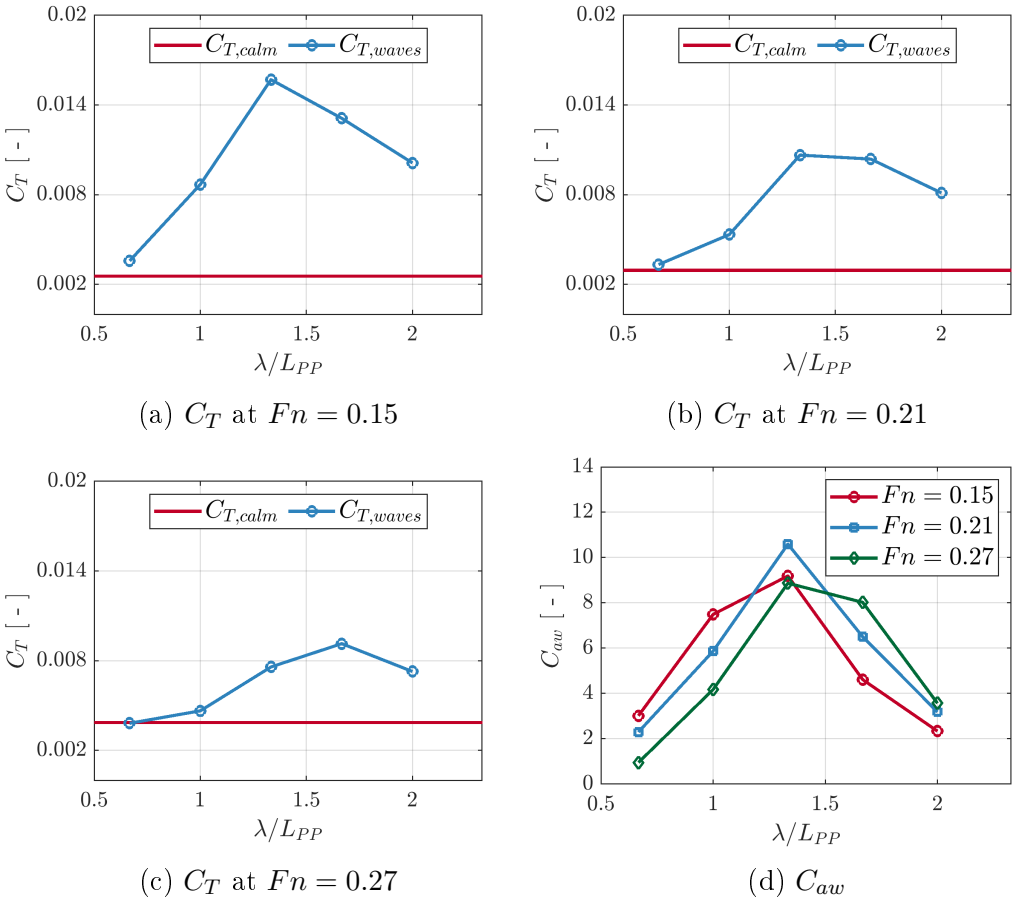

(a) C_T at $Fn = 0.15$

(b) C_T at $Fn = 0.21$

(c) C_T at $Fn = 0.27$

(d) C_{aw}

Figure 5.17: Resistance coefficient, C_T, and added wave resistance coefficient, C_{aw}

The results obtained for the added resistance coefficient, C_{aw}, are shown in Figure 5.17d. For all three speeds, a maximum value is observed when $\lambda/L_{PP} = 1.33$. However, the global maximum added resistance is seen for the

service speed, i.e. $Fn = 0.21$. This could be ascribed to the fact that f_e is close to f_{n3} and f_{n5}. This observation was also made by Simonsen *et al.* (2013), who found that the maximum added resistance occurred when $\lambda/L_{PP} = 1.33$ and $f_e \approx f_n$ for $Fn = 0.33$. At lower speeds, the added wave resistance coefficient increases when $\lambda/L_{PP} = 0.67$ and 1. In contrast, in longer waves it increases for the higher speeds.

According to Castiglione *et al.* (2011), the added resistance results from the relative motion between a ship and incident waves. In short waves and at high encounter frequencies it is expected that the added resistance will be small, since the motion of a ship is limited and the waves are reflected by the hull. In long waves, the relative motion between the ship and the incident wave is small and therefore, a small added resistance component is expected. A peak added resistance is expected when the relative motion is high, usually at or close to the natural frequencies of the ship. Therefore, the results presented above confirms that there is a relationship between the motion of a ship and the added resistance.

5.8.4 Influence on effective power at various operating speeds

The effective power, P_E, is defined as the power required to propel the vessel through water at a constant forward speed, and is calculated as the product of the total drag resistance and speed (Bertram, 2012).

As the SA Agulhas II occasionally operates on a tight schedule during her expeditions, it is often required to increase sailing speed to a maximum of 18 kn. Bearing in mind that the daily operational cost of the vessel is approximately 400 000ZAR (Devanunthan, 2019), of which 30%−50% is dedicated to fuel (Bergqvist *et al.*, 2015), it was deemed worthwhile to investigate the effect of operating speed on the effective power.

In order to investigate the influence on the effective power relative to her service speed of 14 kn, two cases are considered, a reduced speed of 10 kn and an increased speed of 18 kn. The % change in effective power is quantified as follows (Tezdogan *et al.*, 2015):

$$\%\text{Change in } P_E \text{ at 10 kn} = \frac{P_{E(10\text{ kn})} \cdot t_{(10\text{ kn})}}{P_{E(14\text{ kn})} \cdot t_{(14\text{ kn})}} - 1 \tag{5.19}$$

$$\%\text{Change in } P_E \text{ at 18 kn} = \frac{P_{E(18\text{ kn})} \cdot t_{(18\text{ kn})}}{P_{E(14\text{ kn})} \cdot t_{(14\text{ kn})}} - 1 \tag{5.20}$$

where $t_{(10\text{ kn})}/t_{(14\text{ kn})}$ and $t_{(18\text{ kn})}/t_{(14\text{ kn})}$ are referred to as the transit time ratios.

It should be noted that the change in effective power also gives an approximation of the increase or decrease in fuel consumption and CO_2 emissions. However, the direct calculation of fuel consumption is more complex and de-

pends on a variety of variables such as propeller speed, specific oil consumption and engine load, as discussed by Tezdogan *et al.* (2015).

The potential benefit of operating at reduced speeds is shown in Figure 5.18a. The change in effective power due to increased speeds is shown in Figure 5.18b. The maximum effective power reduction of 42 % is observed when reducing operating speed by 4 kn. On the contrary, it is seen than a speed increase of 4 kn could lead to an increase in the maximum effective power of 87 % when $\lambda/L_{PP} = 1.33$.

Tezdogan *et al.* (2015) found that the effective power decreases by 52 % when reducing the operating speed of the KCS from 24 kn to 19 kn, for a similar wave-to-ship length ratio. Therefore, it can be assumed that the results obtained are consistent with literature.

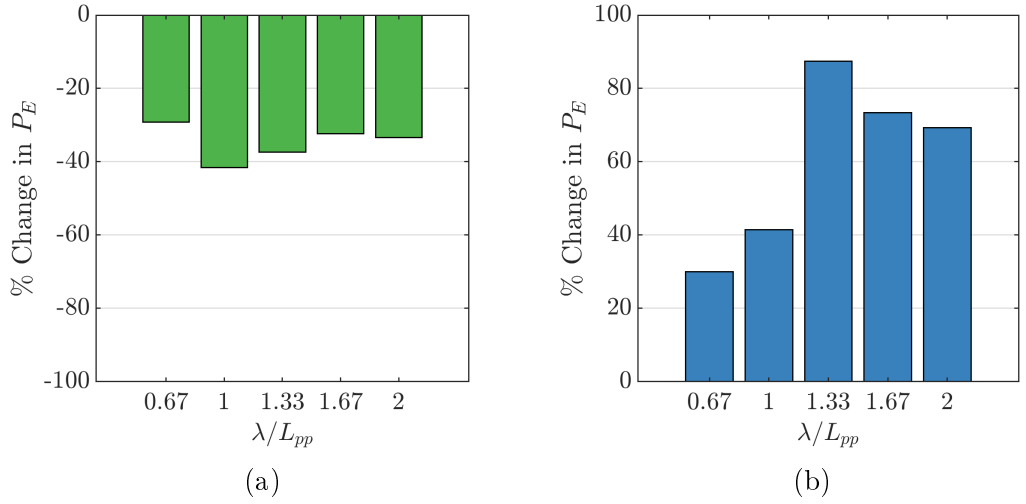

Figure 5.18: Estimation of (a) the effective power decrease from 14 kn to 10 kn and (b) the effective power increase from 14 kn to 18 kn in waves.

In a recent study presented by Durandt (2020), a data-driven model was developed for the SA Agulhas II to optimise operating conditions based on the vessel's speed. This study presented that an increase of approximately 20% in speed (from 13.4 to 17.2 kn) could double the required power. The present study, which is based on physics modelling, suggests that the increase could be up to 87 %, especially in cases where the vessel is experiencing severe motion.

From the RAOS calculated using CFD, it is estimated that the vessel experiences severe motion when the encounter frequency ranges from 0.124 to 0.143 Hz. Therefore, as depicted in Figure 5.18, it may be advantageous to operate the vessel at lower speeds in such operating conditions. However, it should be borne in mind that operating at lower speeds increases time-related operating cost such as labour and maintenance (Durandt, 2020).

5.8.5 The occurrence of wave slamming

Slamming is defined as the sudden increase in force in a short duration imposed on a body (Kapsenberg, 2011). According to the American Bureau of Shipping (2011), the phenomenon occurs when the bow or stern of a vessel emerges from a wave and re-enters the water with a heavy impact. Ice-going vessels, such as the SA Agulhas II, are prone to experience bow slamming due to their increased bow flare angle. Also, the vessel's stern area has been designed with a flat section to provide the necessary space required for container laboratories (Omer, 2016*a*). This flat stern area design results in stern slamming even when operating in sea conditions with the wave height less than 1 m (Omer, 2016*a*).

From the free surface elevation plots presented in Figures 5.12 and 5.14 it is evident that the vessel might be experiencing slamming as she heaves and pitches through regular head waves. To further investigate the occurrence of slamming, numerical pressure probes were used to measure the pressure at the bow and stern region (see Figure 5.19). These probes are useful to quantify the pressure experienced at these regions.

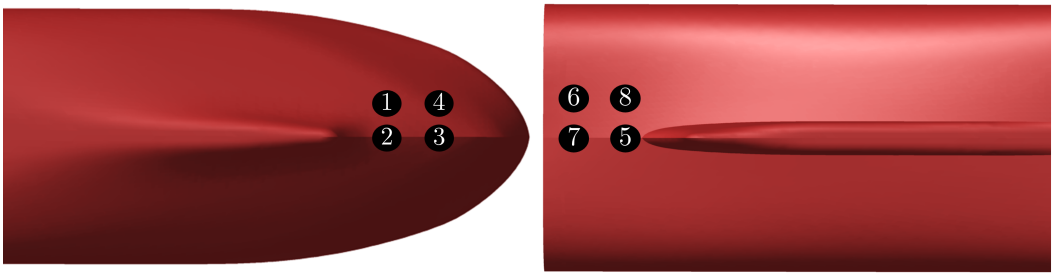

(a) Bow region (b) Stern region

Figure 5.19: Location of flow probes used to measure hydrodynamic pressure at the bow and stern region

The time series of the measured pressure obtained from the numerical pressure probes are shown in Figure 5.20. For Case 2.3 an instantaneous increase in pressure of 85 kPa is found, while for Case 3.5, it is 70 kPa. These increases are more pronounced at the centreline of the vessel's bow, i.e. Probes 2 and 3. The pressure measurements at the stern region showed no instantaneous increase in pressure. This suggests that no stern slamming occurs for these wave conditions.

The results discussed above show that the vessel might experience wave slamming even though the vessel is not operating in extreme wave conditions. It would be interesting to further investigate the pressure in such a wave condition. For example, Kim (2013) conducted a study on the KCS travelling in bow-quartering seas with a height of 19 m. The study found that the pressure measured at the bow could increase up to 200 kPa. Furthermore, it is recommended to conduct CFD simulations of a stationary ship in following waves.

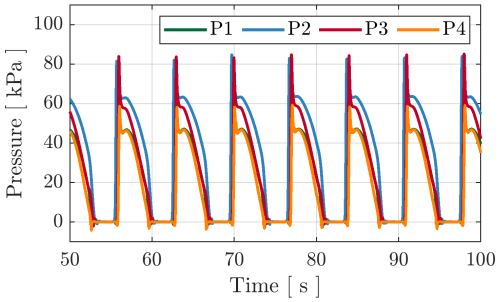

(a) Pressure at bow during Case 2.3

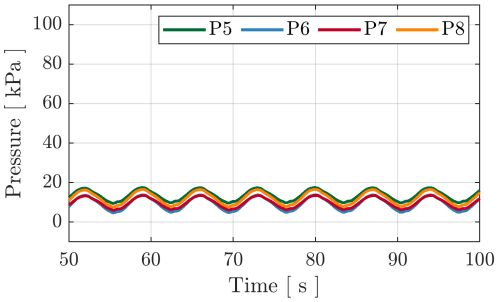

(b) Pressure at bow during Case 2.3

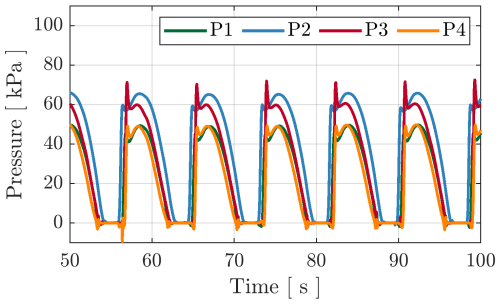

(c) Pressure at stern during Case 3.5

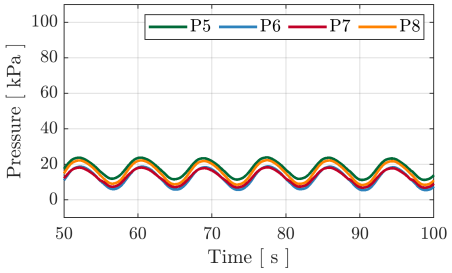

(d) Pressure at stern during Case 3.5

Figure 5.20: Numerical pressure measurements at bow and stern region

A study presented by Oberhagemann *et al.* (2010), found that the pressure at the stern region reaches a peak value of 305 kPa in following waves with an amplitude of 14.2 m. In contrast, a peak pressure value of approximately 70 kPa was observed in head waves with an amplitude of 12.2 m.

5.9 Conclusion

This chapter presented a CFD study of the seakeeping behaviour of the SA Agulhas II in head waves. A benchmark study of her calm water characteristics was conducted. Thereafter, her heave and pitch motion were evaluated. The maximum heave response occurred when $f_e = 0.143$ Hz, which is close to the estimated f_{n3}. For pitch, the maximum response occurred when $f_e = 0.124$ to 0.134 Hz, which is slightly higher than the estimated f_{n5}. The maximum added resistance in waves occurred when the largest amplitude motion occurred. The absolute maximum added resistance coefficient was observed for the medium speed, $Fn = 0.21$, and when $\lambda/L_{PP} = 1.33$. It is estimated that the effective power decreases by 42 % when decreasing speed from 14 kn to 10 kn, whereas an increase from 14 kn to 18 kn could lead to an increase of 87 %. Finally, instantaneous increases in pressure at the bow region were observed close to resonance conditions. This suggests that slamming might occur even in wave heights of 2.69 m.

Chapter 6

Conclusion and recommendations

6.1 Conclusion

The SA Agulhas II plays a key role in logistical support and research activities in the Southern Ocean and Antarctica. Although she is built to Polar Class PC5, it is estimated that she spends 85 % of her voyages in long open water transits in the Southern Ocean. The aim of this study was to investigate seakeeping behaviour of the SA Agulhas II in waves. This section draws conclusions from the main findings in response to the objectives posed in Section 1.3.

Full-scale measurements

Full-scale measurements were conducted during the 2019 SCALE Winter Cruise. During this campaign, the vessel was instrumented with ten linear DC accelerometers, which were used in the Six Accelerometer Method (SAM) to calculate the angular velocity of the body. Furthermore, the lines plan drawing of the vessel was acquired from which a 3D geometry of the hull was developed. Hydrostatic properties of the vessel were used to estimate her heave, roll and pitch motion natural frequencies, which were calculated as $f_{n3} \approx 0.149$ Hz, $f_{n4} \approx 0.067$ Hz and $f_{n5} \approx 0.112$ Hz. Moreover, information about the sea state parameters were obtained from the ECMWF ERA5 database, which is available at Copernicus Climate Change Service (2017). The acquired parameters were used to calculate the wave spectrum described through a parametric formulation, namely the ITTC Wave Spectrum.

Linear acceleration and angular velocity data obtained from this campaign were used to determine the heave, roll and pitch motion of the vessel. The measured responses provided valuable insight into the behaviour of the vessel in a realistic environment. From six case studies, it was observed that heave and pitch showed broad-banded spectra with multiple peaks observed between 0.08 to 0.14 Hz. For roll motion, narrow-banded response spectra were observed with peak frequencies between 0.06 to 0.09 Hz.

Motion prediction in irregular seas

In order to predict the vessel's motion responses in irregular seas, the RAOs of the SA Agulhas II were calculated over a range of wave frequencies and directions using the open-source strip theory program, PDSTRIP. The amplitude of the RAOs showed peaks close to the estimated natural frequencies. For heave absolute maximum peaks were observed at circa 0.14 Hz in beam waves. Peak amplitude for roll motion was observed at 0.07 Hz and for pitch the peak frequencies ranging between 0.10 to 0.13 Hz.

Through the assumption of linearity between the RAOs and ITTC wave spectrum, the motion response spectra of the vessel were predicted in irregular seas. A comparison between measured and predicted motion response spectra showed that it is possible to predict heave and pitch motion with reasonable accuracy. Roll motion showed various discrepancies due to non-linear effects, such as roll-damping from anti-roll tanks. In addition, a sensitivity analysis showed that care should be taken during the prediction process since it is influenced by various input parameters. For example, roll motion was found to be particularly sensitive to the metacentric height and roll radii of gyration.

CFD investigation in head waves

The motion response and added resistance in head waves were investigated using the CFD software package FINE^{TM}/Marine. During this work three speeds were considered: the vessel's service speed of 14 kn, a reduced speed of 10 kn and a maximum speed of 18 kn. The results showed that the maximum heave responses occurred close to f_{n3}. The maximum pitch responses occurred at frequencies slightly higher than f_{n5}. Overall, the results showed that the maximum heave and pitch are expected to occur when the encounter frequency ranges between 0.124 to 0.143 Hz. Furthermore, RAO results obtained from CFD and strip theory were found to be in fair agreement. For all three speeds, the maximum added resistance in waves were observed when resonance occurs. This confirms that there is a relationship between the motion response of the vessel and resistance (Castiglione *et al.*, 2011). It was further shown that reduction of speed from 14 kn to 10 kn could decrease the effective power by 42 %. On the other hand, increasing speed from 14 kn to 18 kn could lead to a maximum increase in effective power of 87 %. During the CFD investigation it was also observed that bow slamming could occur when large amplitude heave and pitch motions occur, even in small to moderate wave heights of 2.69 m.

6.2 Recommendations

Future research in seakeeping for the SA Agulhas II should aim to improve and develop performance prediction techniques. Based on the main findings from this study, the following recommendations are made for future work.

Full-scale measurements

Commercial motion reference units could reduce extensive signal processing required to evaluate the motion response of the SA Agulhas II. Alternatively, additional IMU sensors could be acquired to improve the current Kalman filter algorithm. In addition to motion responses, the vertical bending moment can be investigated by equipping the vessel with strain gauges. Using a variety of responses may provide further insight into the behaviour of the vessel in irregular seas. Moreover, a variety of responses may contribute towards the use of the SA Agulhas II as a means to estimate the sea state in which the vessel is travelling. For example, Montazeri (2016) used sway, heave, pitch and vertical bending at amidship. Finally, the Wave Analysis for Fatigue and Oceanography (WAFO) MATLAB® toolbox is recommended for spectral analysis and statistical evaluation of measured responses (WAFO-group, 2000).

Wave spectrum

For the prediction of motion responses in irregular seas, alternative parametric formulations should be considered in future studies, such as the JONSWAP Spectrum. Further investigations are required for multi-directional sea states, since it was found that the prediction of motion responses in such sea states were particularly difficult. This may also be evaluated using the WAFO toolbox.

An onboard wave radar could be used to more accurately record the seaway during voyages. This may further contribute towards the validation of the motion response prediction, or the estimation of the sea state from measured responses. Alternatively, measurements can be conducted near wave buoys, as presented by Ha and Gourlay (2018).

Response Amplitude Operators

PDSTRIP proved to be a fast, inexpensive and sufficiently accurate method to investigate the seakeeping behaviour of the SA Agulhas II. Further research should attempt to calculate the RAOs of the vessel using alternative hydrodynamic software. More specifically, it is recommended to use software which accounts for additional non-linear effects such as roll damping.

Computational Fluid Dynamics

CFD proved to be a useful method to gain insight into the seakeeping behaviour of the SA Agulhas II in head waves. This study provides a starting point for various aspects which can be considered for future studies.

Future work should extend the geometry of the vessel and incorporate additional appendages, which include propellers, rudders, shafts and the superstructure. A fully appended geometry may be simulated with a rotating propeller and compared to full-scale measurements of shaft torque and rotational speed. As an example, reference is made to Ponkratov (2017). This could further contribute towards the validation of full-scale CFD simulations.

During the 2019 SCALE Winter Cruise it was observed that the vessel was operating at off-design loading conditions. Investigations into the impact of variations in draft and trim conditions are recommended. Additionally, it was observed that the ship is steered to encounter bow quartering waves. This is done to avoid stern slamming. It would be interesting to further evaluate effect of bow quartering waves on her motion responses, resistance and effective power.

The results presented in Section 5.8.5 highlight that the vessel's spoon-shaped bow makes her prone to slamming even in small to moderate wave conditions. CFD shows clear potential for further investigations into slamming. Additional wave probes should be included at the bow and stern region. This may be useful to locate areas where peak impact pressure occurs. Furthermore, it is recommended to evaluate a stationary ship in head waves and following waves. Finally, impact pressure during extreme wave conditions should also be investigated.

Appendices

Appendix A

Euler angles and unit quaternions

A.1 Introduction

In the literature review, presented in Chapter 2, the roll, pitch and yaw displacement angles, ξ_4, ξ_5 and ξ_6, are introduced. These are defined as Euler angles, $\boldsymbol{\Theta} = \begin{bmatrix}\phi & \theta & \psi\end{bmatrix}^T$ (Perez, 2005). The purpose of this chapter is to present a review of Euler angles and unit quaternions with reference to discussions in Fossen (2011). Furthermore, it elaborates the use of quaternions to calculate the roll and pitch angles through the Kalman filter algorithm discussed in Section 4.3.

A.2 Euler angles

The Euler angles define the orientation of the b-frame relative to the n-frame. The Euler angles are three consecutive rotations (Perez, 2005) which include: a rotation about the x_n-axis called roll (ϕ), a rotation about the y_n axis is called pitch (θ) and a rotation about the z_n-axis is called yaw (ψ).

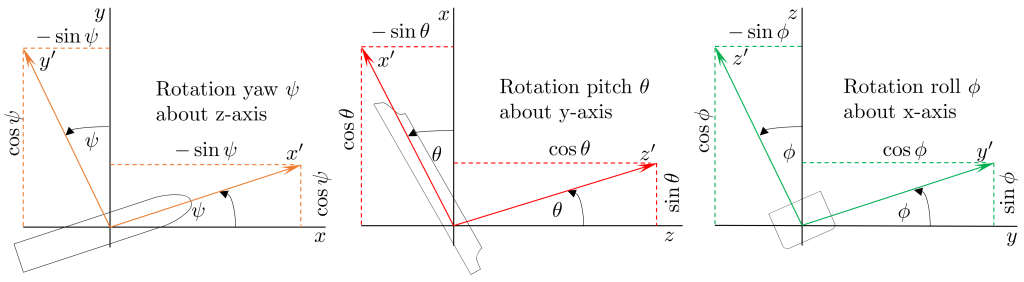

Figure A.1: Demonstration of the three principle rotations.

To transform from the b-frame to the n-frame, a rotation matrix $\boldsymbol{R}(\boldsymbol{\Theta})$ is introduced. The rotation matrix is defined by three principal rotations about

the z, y and x axes (zyx convention) (Fossen, 2011). A demonstration of the three principle rotations is given in Figure A.1.

The principle rotations with respect to the z-axis ($\boldsymbol{R}_{z,\psi}$), the y-axis ($\boldsymbol{R}_{y,\phi}$) and the z-axis ($\boldsymbol{R}_{x,\phi}$) yields the matrix presented in Equation A.1.

$$\boldsymbol{R}_{z,\psi} = \begin{bmatrix} c\psi & -s\psi & 0 \\ s\psi & c\psi & 0 \\ 0 & 0 & 1 \end{bmatrix}, \boldsymbol{R}_{y,\phi} = \begin{bmatrix} c\theta & 0 & s\theta \\ 0 & 1 & 0 \\ -s\theta & 0 & c\theta \end{bmatrix}, \boldsymbol{R}_{x,\phi} = \begin{bmatrix} 1 & 0 & 0 \\ 0 & c\phi & -s\phi \\ 0 & s\phi & c\phi \end{bmatrix} \tag{A.1}$$

where, $c\cdot = \cos(\cdot)$ and $s\cdot = \sin(\cdot)$.

The rotation matrix, $\boldsymbol{R}(\boldsymbol{\Theta})$, is calculated from the three principle rotations by $\boldsymbol{R}(\boldsymbol{\Theta}) = \boldsymbol{R}_{z,\psi}\boldsymbol{R}_{y,\phi}\boldsymbol{R}_{x,\phi}$, and is given as

$$\boldsymbol{R}(\boldsymbol{\Theta}) = \begin{bmatrix} c\psi c\theta & -s\psi c\phi + c\psi s\theta s\phi & s\psi s\phi + c\psi c\phi s\theta \\ s\psi c\theta & c\psi c\phi + s\phi s\theta s\psi & -c\psi s\theta + s\theta s\psi c\phi \\ -s\theta & c\theta s\phi & c\theta c\phi \end{bmatrix} \tag{A.2}$$

A.3 Unit quaternions

Unit quaternions are an alternative four parameter method to represent the orientation of a body (Greenwood, 2003). The unit quaternions are described by one real part, q_0 and three imaginary parts, q_1, q_2 and q_3 in the following vector (Fossen, 2011):

$$\boldsymbol{q} = \begin{bmatrix} q_0 & q_1 & q_2 & q_3 \end{bmatrix}^T \tag{A.3}$$

The quaternions can be determined through the Euler angles as follows:

$$\begin{bmatrix} q_0 \\ q_1 \\ q_2 \\ q_2 \end{bmatrix} = \begin{bmatrix} c\frac{\phi}{2}c\frac{\theta}{2}c\frac{\psi}{2} + s\frac{\phi}{2}s\frac{\theta}{2}s\frac{\psi}{2} \\ s\frac{\phi}{2}c\frac{\theta}{2}c\frac{\psi}{2} - c\frac{\phi}{2}s\frac{\theta}{2}s\frac{\psi}{2} \\ c\frac{\phi}{2}s\frac{\theta}{2}c\frac{\psi}{2} + s\frac{\phi}{2}c\frac{\theta}{2}s\frac{\psi}{2} \\ c\frac{\phi}{2}c\frac{\theta}{2}s\frac{\psi}{2} - s\frac{\phi}{2}s\frac{\theta}{2}c\frac{\psi}{2} \end{bmatrix} \tag{A.4}$$

The parametrization defined in Equation A.4 implies that unit quaternions satisfy the constraint $\boldsymbol{q}^T\boldsymbol{q} = 1$.
The quaternion rotation matrix, $\boldsymbol{R}(\boldsymbol{q})$, is given as follows:

$$\boldsymbol{R}(\boldsymbol{q}) = \begin{bmatrix} 1-2(q_0^2+q_3^2) & 2(q_1q_2-q_3q_0) & 2(q_1q_3+q_2q_0) \\ 2(q_1q_2+q_3q_0) & 1-2(q_1^2+q_3^2) & 2(q_2q_3-q_1q_0) \\ 2(q_1q_3-q_2q_0) & 2(q_2q_3+q_1q_0) & 1-2(q_1^2+q_2^2) \end{bmatrix} = \begin{bmatrix} R_{11} & R_{12} & R_{13} \\ R_{21} & R_{22} & R_{23} \\ R_{31} & R_{32} & R_{33} \end{bmatrix} \tag{A.5}$$

A.4 Quaternions to Euler angles

The unit quaternions can be used to determine the Euler angles by requiring that the associated rotation matrices are equal, i.e. $\boldsymbol{R}(\boldsymbol{\Theta}) = \boldsymbol{R}(\boldsymbol{q})$. This implies that (Fossen, 2011):

$$\begin{bmatrix} c\psi c\theta & -s\psi c\phi + c\psi s\theta s\phi & s\psi s\phi + c\psi c\phi s\theta \\ s\psi c\theta & c\psi c\phi + s\phi s\theta s\psi & -c\psi s\theta + s\theta s\psi c\phi \\ -s\theta & c\theta s\phi & c\theta c\phi \end{bmatrix} = \begin{bmatrix} R_{11} & R_{12} & R_{13} \\ R_{21} & R_{22} & R_{23} \\ R_{31} & R_{32} & R_{33} \end{bmatrix} \tag{A.6}$$

Finally, from Equation A.6 it follows that the Euler angles can be determined using the quaternions as follows:

$$\phi = \text{atan2}\left(R_{32}, R_{33}\right) \tag{A.7}$$

$$\theta = -\arcsin\left(R_{31}\right) \tag{A.8}$$

$$\psi = \text{atan2}\left(R_{21}, R_{11}\right) \tag{A.9}$$

The atan2(x, y) is the four-quadrant arctangent function which returns the angles in the range of $\pm 90°$.

A.5 Attitude determination from onboard measurements

The purpose of this section is to introduce methods to determine the roll and pitch from angular velocity and linear acceleration measurements. Additionally, it serves as an introduction to the Kalman filter algorithm, presented in Section 4.3.1, which combines angular velocity and linear acceleration measurements to determine the attitude of a body.

The following sections summarize the process as described by Kim (2011).

A.5.1 Attitude determination from angular velocity

The Euler angles are determined from the angular velocity based on the relationship between the rate of change of unit quaternions, $\dot{\boldsymbol{q}}$, and the angular velocities, $\boldsymbol{\omega}$, i.e. Equation A.10.

The relationship between the rate of change of quaternions, $\dot{\boldsymbol{q}}$, and the angular velocity of the body, $\boldsymbol{\omega} = \begin{bmatrix} \omega_x & \omega_y & \omega_z \end{bmatrix}^T$, is given as follows:

$$\dot{\boldsymbol{q}} = \boldsymbol{T}_\omega(\boldsymbol{\omega})\boldsymbol{q} \tag{A.10}$$

where $\boldsymbol{T}_\omega(\boldsymbol{\omega})$ is the quaternion transformation matrix which may be expanded as follows (Kim, 2011):

$$\boldsymbol{T}_{\omega}(\boldsymbol{\omega}) = \begin{bmatrix} 0 & -\omega_x & -\omega_y & -\omega_z \\ \omega_x & 0 & \omega_z & -\omega_y \\ \omega_y & -\omega_z & 0 & \omega_x \\ \omega_z & \omega_y & -\omega_x & 0 \end{bmatrix} \tag{A.11}$$

The quaternions, $\boldsymbol{q}$, can be determined by integrating $\dot{\boldsymbol{q}}$ with respect to time. Thereafter, the Euler angles can be calculated based on the requirement that $\boldsymbol{R}(\Theta) = \boldsymbol{R}(q)$, as shown in Equation A.6. This implies that:

$$\phi = \text{atan2}\left(\frac{2(q_2 q_3 + q_1 q_0)}{1 - 2(q_1^2 + q_2^2)}\right) \tag{A.12}$$

$$\theta = -\arcsin\left(2(q_1 q_3 - q_2 q_0)\right) \tag{A.13}$$

A.5.2 Attitude determination with accelerometers

The roll and pitch attitude can be determined from measured accelerations (a_x, a_y, a_z), obtained from a triaxial accelerometer. For this, the assumption is made that the object is stationary or moving at a constant velocity. Thereby, the triaxial accelerometer only measures the gravitational acceleration, g. Therefore, the acceleration measurement may then be expressed as follows:

$$\begin{bmatrix} a_x \\ a_y \\ a_z \end{bmatrix} = \boldsymbol{R}^{-1}(\Theta) \begin{bmatrix} 0 \\ 0 \\ -g \end{bmatrix} = \begin{bmatrix} -g \sin\theta \\ g \sin\phi \cos\theta \\ g \cos\phi \cos\theta \end{bmatrix} \tag{A.14}$$

Hence, the roll (ϕ) and pitch (θ) angles can be determined as follows:

$$\phi = \arcsin\left(\frac{a_y}{g \cos\theta}\right) \tag{A.15}$$

$$\theta = \arcsin\left(\frac{a_x}{g}\right); \theta \neq \pm 90^{\circ} \tag{A.16}$$

The Euler angles determined the accelerometers, i.e. Equations A.15–A.16 can be transformed into unit quaternions by substituting it into Equation A.4 (Fossen, 2011). The quaternions calculated from the accelerometer is applied in the Kalman filter algorithm to serve as an attitude observer, see Section 4.3.1.

A.6 Conclusion

This chapter presented a review Euler angles and unit quaternions. Furthermore, a means to calculate the attitude from angular velocity and linear acceleration measurements were discussed.

Appendix B

The Six Accelerometer Method

B.1 Introduction

In Chapter 4, it is seen that knowledge is required about the angular velocity of the vessel to determine the Euler angles, more specifically roll and pitch. In order to determine the angular velocity of the body, the Six Accelerometer Method (SAM) was implemented. This chapter presents the methodology, derivation and validation of the SAM.

B.2 Methodology

During the full-scale measurement campaign, presented in Chapter 3, the vessel was instrumented with ten linear accelerometers. Based on kinematic principles, the angular acceleration and velocity of a body can be determined from linear acceleration measurements. The theory of this method was presented by Padgaonkar *et al.* (1975). In addition, the SAM has previously been applied on the SA Agulhas II by Boulle (2016). Although a similar approach is taken in this study, it is worth noting that the sensor location of Point 2 is different. Therefore, the calculation of the angular acceleration differs.

An illustration of the layout of the SAM is shown in Figure B.1a, while the location of Points 0, 1 and 2 are shown in Figure B.1a. An illustration of the angular acceleration, velocity and the corresponding notation is given in Figure B.1b.

The theoretical development of the SAM starts by considering the acceleration at a point P $\boldsymbol{a}_p$ on a rigid body, which is given as (Greenwood, 2003):

$$\boldsymbol{a}_p = \ddot{\boldsymbol{R}} + \boldsymbol{\alpha} \times \boldsymbol{r}_P + \boldsymbol{\omega} \times (\boldsymbol{\omega} \times \boldsymbol{r}_P) + (\boldsymbol{a}_{P/O'})_r + 2\boldsymbol{\omega} \times (\boldsymbol{v}_{P/O'})_r \tag{B.1}$$

where,
$\ddot{\boldsymbol{R}}$ = acceleration of the b-frame with respect to the n-frame
$(\boldsymbol{a}_{P/O'})_r$ = acceleration of point P relative to the b-frame

$\boldsymbol{\omega}$ = angular velocity of the body
$(\boldsymbol{v}_{P/O'})_r$ = velocity of point P relative to the b-frame
$\boldsymbol{\alpha}$ = angular acceleration of the body
$\boldsymbol{r}_P$ = position of the point P relative from the origin of the b-frame

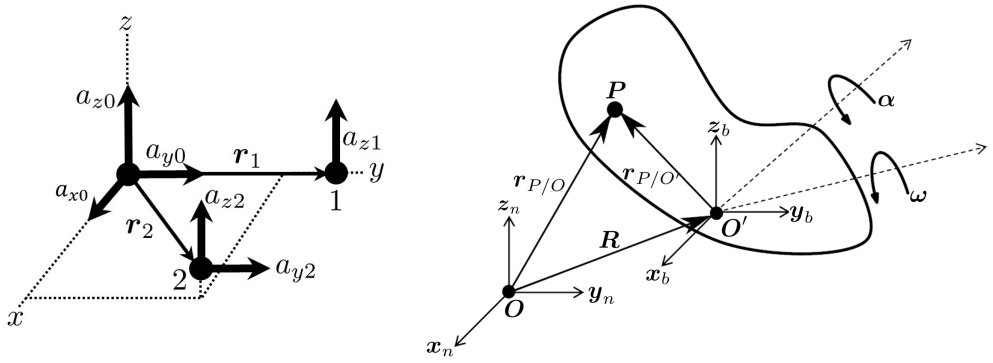

(a) (b)

Figure B.1: Illustration of (a) the configuration of the SAM and (b) the angular acceleration and velocity of a rigid body.

The assumption is made that the vessel is a rigid body, which implies that $(\boldsymbol{a}_{P/O'})_r = 0$ and $(\boldsymbol{v}_{P/O'})_r = 0$, Equation B.1 reduces to:

$$\boldsymbol{a_p} = \ddot{\boldsymbol{R}} + \boldsymbol{\alpha} \times \boldsymbol{r}_P + \boldsymbol{\omega} \times (\boldsymbol{\omega} \times \boldsymbol{r}_P) \tag{B.2}$$

From, the SAM configuration it is seen that:

$$\ddot{\boldsymbol{R}} = a_{x0}\mathbf{i} + a_{y0}\mathbf{j} + a_{z0}\mathbf{k} \tag{B.3}$$

$$\boldsymbol{r}_0 = 0\mathbf{i} + 0\mathbf{j} + 0\mathbf{k} \tag{B.4}$$

$$\boldsymbol{r}_1 = 0\mathbf{i} + r_{y1}\mathbf{j} + 0\mathbf{k} \tag{B.5}$$

$$\boldsymbol{r}_2 = r_{x2}\mathbf{i} + r_{y2}\mathbf{j} + r_{z2}\mathbf{k} \tag{B.6}$$

It follows that the angular acceleration of the body can then be calculated as follows:

$$\alpha_x = \frac{(a_{z1} - a_{z0})}{r_{y1}} \tag{B.7}$$

$$\alpha_y = \frac{(a_{z0} - a_{z2})}{r_{x2}} + \frac{\omega_x(\omega_z r_{x2} - \omega_x r_{z2})}{r_{x2}} - \frac{\omega_y(\omega_y r_{z2} - \omega_z r_{y2})}{r_{x2}} + \frac{\alpha_x r_{y2}}{r_{x2}} \tag{B.8}$$

$$\alpha_z = \frac{(a_{y2} - a_{y0})}{r_{x2}} + \frac{\omega_x(\omega_x r_{y2} - \omega_y r_{x2})}{r_{x2}} - \frac{\omega_z(\omega_y r_{z2} - \omega_z r_{y2})}{r_{x2}} + \frac{\alpha_x r_{z2}}{r_{x2}} \tag{B.9}$$

The derivation of Equations B.7–B.9 is presented in the following section. From these equations, it is seen that prior knowledge is required about the angular velocity, $\boldsymbol{\omega}$, of the body. Since it is not known, it is solved numerically through an iterative procedure, as shown in Figure B.2.

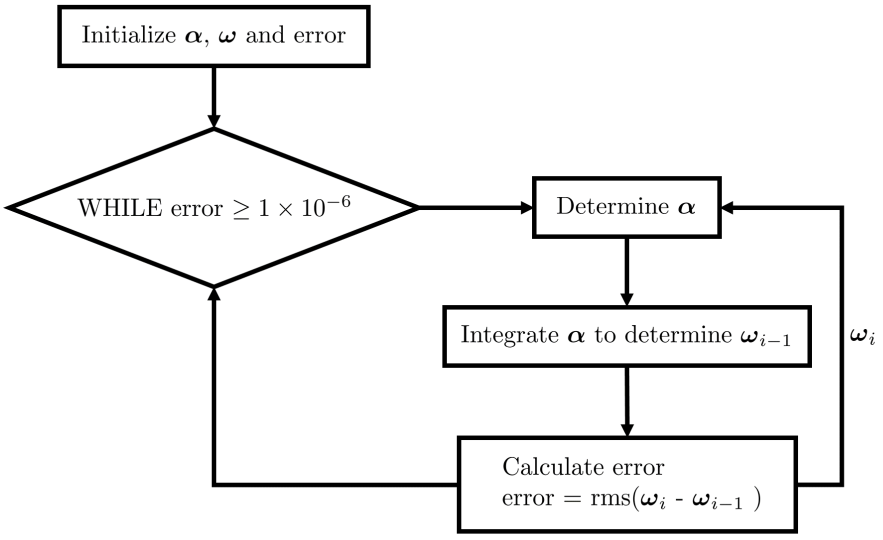

Figure B.2: Flow diagram of the iterative calculation of angular velocity.

The values of $\boldsymbol{\alpha}$ and $\boldsymbol{\omega}$ are initialized as zero. Then, $\boldsymbol{\alpha}$ is determined through Equations B.7–B.9 and $\boldsymbol{\omega}$ is determined by integrating $\boldsymbol{\alpha}$. For the integration procedure, it was noted that the cumulative trapezoidal method used by Boulle (2016) did not lead to convergence for periods longer than 20 minutes. Therefore, the `timeint.m` function (Brandt, 2018) was used, as discussed in Section 3.5. Thereafter, $\boldsymbol{\omega}$ is substituted back into Equations B.7–B.9.

The iterative process is repeated until sufficient convergence is achieved, i.e. until the error tolerance is smaller than 1×10^{-6}. The error is defined as the root-means-square (RMS) difference between the current and previous iteration of $\boldsymbol{\omega}$. The RMS is defined as follows (Brandt, 2010):

$$x_{RMS} = \sqrt{\frac{1}{N}\sum_{n=0}^{N-1} x^2(n)} \tag{B.10}$$

where N is the number of samples of the signal $x(n)$.

Once $\boldsymbol{\alpha}$ and $\boldsymbol{\omega}$ have been determined, the acceleration at any point in the vessel can be calculated using Equation B.2. This approach is used to validate the SAM, by calculating the acceleration at points 4 and 5 and comparing it with the measured acceleration at those points. Furthermore, this was also

applied to calculate the acceleration at the COG of the vessel, as discussed in Section 4.3.2.

B.3 Derivation of the angular acceleration of a rigid body using the six accelerometer method

This section discusses the derivation of the angular acceleration, Equations B.7–B.9. A similar derivation for a different configuration was presented in Boulle (2016).

Recalling that $\ddot{\boldsymbol{R}} = \boldsymbol{a_0}$, the accelerations at points $P = 1$ and 2 can be given as follows:

$$\boldsymbol{a_1} = \boldsymbol{a_0} + \boldsymbol{\alpha} \times \boldsymbol{r}_1 + \boldsymbol{\omega} \times (\boldsymbol{\omega} \times \boldsymbol{r}_1) \tag{B.11}$$

$$\boldsymbol{a_2} = \boldsymbol{a_0} + \boldsymbol{\alpha} \times \boldsymbol{r}_2 + \boldsymbol{\omega} \times (\boldsymbol{\omega} \times \boldsymbol{r}_2) \tag{B.12}$$

where, $\boldsymbol{\omega}$ and $\boldsymbol{\alpha}$ are the angular velocity and acceleration of body, which is defined as:

$$\boldsymbol{\omega} = \omega_x \mathbf{i} + \omega_y \mathbf{j} + \omega_z \mathbf{k} \tag{B.13}$$

$$\boldsymbol{\alpha} = \alpha_x \mathbf{i} + \alpha_y \mathbf{j} + \alpha_z \mathbf{k} \tag{B.14}$$

The cross products in Equation B.11 can be solved to obtain the following:

$$\boldsymbol{\alpha} \times \boldsymbol{r}_1 = \begin{vmatrix} \mathbf{i} & \mathbf{j} & \mathbf{k} \\ \alpha_x & \alpha_y & \alpha_z \\ 0 & r_{y1} & 0 \end{vmatrix} = -\alpha_z r_{y1} \mathbf{i} + \alpha_x r_{y1} \mathbf{k} \tag{B.15}$$

$$\boldsymbol{\omega} \times \boldsymbol{r}_1 = \begin{vmatrix} \mathbf{i} & \mathbf{j} & \mathbf{k} \\ \omega_x & \omega_y & \omega_z \\ 0 & r_{y1} & 0 \end{vmatrix} = -\omega_z r_{y1} \mathbf{i} + \omega_x r_{y1} \mathbf{i} \tag{B.16}$$

$$\boldsymbol{\omega} \times (\boldsymbol{\omega} \times \boldsymbol{r}_1) = \begin{vmatrix} \mathbf{i} & \mathbf{j} & \mathbf{k} \\ \omega_x & \omega_y & \omega_z \\ -\omega_z r_{y1} & 0 & \omega_x r_{y1} \end{vmatrix} = \omega_x \omega_y r_{y1} \mathbf{i} - (\omega_x^2 + \omega_z^2) r_{y1} \mathbf{j} + \omega_z \omega_y r_{y1} \mathbf{k} \tag{B.17}$$

Substituting Equations B.15–B.17 into Equation B.11 yields the following:

$$\begin{bmatrix} a_{x1}\mathbf{i} \\ a_{y1}\mathbf{j} \\ a_{z1}\mathbf{k} \end{bmatrix} = \begin{bmatrix} a_{x0}\mathbf{i} \\ a_{y0}\mathbf{j} \\ a_{z0}\mathbf{k} \end{bmatrix} + \begin{bmatrix} \omega_x \omega_y r_{y1} \mathbf{i} \\ -(\omega_x^2 + \omega_z^2) r_{y1} \mathbf{j} \\ \omega_z \omega_y r_{y1} \mathbf{k} \end{bmatrix} + \begin{bmatrix} -\alpha_z r_{y1} \mathbf{i} \\ 0\mathbf{j} \\ \alpha_x r_{y1} \mathbf{k} \end{bmatrix}. \tag{B.18}$$

Solving the linear acceleration in the z-direction ($\mathbf{k}$ component) yields the angular acceleration about the x-axis:

$$\alpha_x = \frac{(a_{z1} - a_{z0})}{r_{y1}}. \tag{B.19}$$

Furthermore, the cross products in Equation B.12 can be solved as follows:

$$\boldsymbol{\alpha} \times \boldsymbol{r}_2 = \begin{vmatrix} \mathbf{i} & \mathbf{j} & \mathbf{k} \\ \alpha_x & \alpha_y & \alpha_z \\ r_{x2} & r_{y2} & r_{z2} \end{vmatrix} = (\alpha_y r_{z2} - \alpha_z r_{y2})\mathbf{i} + (\alpha_z r_{x2} - \alpha_x r_{z2})\mathbf{j} + (\alpha_x r_{y2} - \alpha_y r_{x2})\mathbf{k} \tag{B.20}$$

$$\boldsymbol{\omega} \times \boldsymbol{r}_1 = \begin{vmatrix} \mathbf{i} & \mathbf{j} & \mathbf{k} \\ \omega_x & \omega_y & \omega_z \\ r_{x2} & r_{y2} & r_{z2} \end{vmatrix} = (\omega_y r_{z2} - \omega_z r_{y2})\mathbf{i} + (\omega_z r_{x2} - \omega_x r_{z2})\mathbf{j} + (\omega_x r_{y2} - \omega_y r_{x2})\mathbf{k} \tag{B.21}$$

$$\begin{aligned} \boldsymbol{\omega} \times (\boldsymbol{\omega} \times \boldsymbol{r}_1) = & \begin{vmatrix} \mathbf{i} & \mathbf{j} & \mathbf{k} \\ \omega_x & \omega_y & \omega_z \\ (\omega_y r_{z2} - \omega_z r_{y2}) & (\omega_z r_{x2} - \omega_x r_{z2}) & (\omega_x r_{y2} - \omega_y r_{x2}) \end{vmatrix} \\ & = (\omega_y(\omega_x r_{y2} - \omega_z r_{x2}) - \omega_z(\omega_z r_{x2} - \omega_y r_{x2}))\mathbf{i} + \\ & (\omega_z(\omega_y r_{z2} - \omega_z r_{y2}) - \omega_x(\omega_x r_{y2} - \omega_y r_{x2}))\mathbf{j} + \\ & (\omega_x(\omega_z r_{x2} - \omega_x r_{z2}) - \omega_y(\omega_y r_{z2} - \omega_z r_{y2}))\mathbf{k} \end{aligned} \tag{B.22}$$

Substituting Equations B.20 and B.22 into Equation B.12, yields the following:

$$\begin{aligned} \begin{bmatrix} a_{x2}\mathbf{i} \\ a_{y2}\mathbf{j} \\ a_{z2}\mathbf{k} \end{bmatrix} = & \begin{bmatrix} a_{x0}\mathbf{i} \\ a_{y0}\mathbf{j} \\ a_{z0}\mathbf{k} \end{bmatrix} + \begin{bmatrix} (\omega_y(\omega_x r_{y2} - \omega_z r_{x2}) - \omega_z(\omega_x r_{y2} - \omega_y r_{x2}))\mathbf{i} \\ (\omega_z(\omega_y r_{z2} - \omega_z r_{y2}) - \omega_x(\omega_x r_{y2} - \omega_y r_{x2}))\mathbf{j} \\ (\omega_x(\omega_z r_{x2} - \omega_x r_{z2}) - \omega_y(\omega_y r_{z2} - \omega_z r_{y2}))\mathbf{k} \end{bmatrix} + \\ & \begin{bmatrix} (\alpha_y r_{z2} - \alpha_z r_{y2})\mathbf{i} \\ (\alpha_z r_{x2} - \alpha_x r_{z2})\mathbf{j} \\ (\alpha_x r_{y2} - \alpha_y r_{x2})\mathbf{k} \end{bmatrix}. \end{aligned} \tag{B.23}$$

By solving the $\mathbf{k}$ component of Equation B.23 the angular acceleration about the y-axis is obtained:

$$\alpha_y = \frac{(a_{z0} - a_{z2})}{r_{x2}} + \frac{\omega_x(\omega_z r_{x2} - \omega_x r_{z2})}{r_{x2}} - \frac{\omega_y(\omega_y r_{z2} - \omega_z r_{y2})}{r_{x2}} + \frac{\alpha_x r_{y2}}{r_{x2}} \tag{B.24}$$

Similarly, the $\mathbf{j}$ component can be solved to obtain the α_z as follows:

$$\alpha_z = \frac{(a_{y2} - a_{y0})}{r_{x2}} + \frac{\omega_x(\omega_x r_{y2} - \omega_y r_{x2})}{r_{x2}} - \frac{\omega_z(\omega_y r_{z2} - \omega_z r_{y2})}{r_{x2}} + \frac{\alpha_x r_{z2}}{r_{x2}} \tag{B.25}$$

B.4 Validation of the Six Accelerometer Method

The SAM was validated by comparing the predicted acceleration with the measured accelerations at Points $3-5$. As an example, Figure B.3 shows the predicted and measured vertical acceleration at Point 3 during Case B. It is seen that the predicted acceleration is in good agreement with the measured. It is also worth noticing that Case B had the roughest sea conditions.

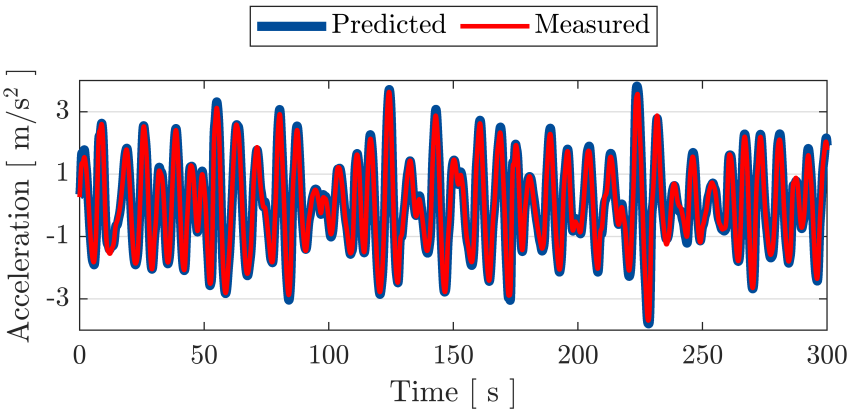

Figure B.3: Validation of the SAM at point 3

The SAM is further validated by evaluating the difference between the predicted and the measured RMS values. The calculated rms values and the % difference for all six case studies, discussed in Section 4.2, are shown in Table B.1. It is seen that the acceleration at a certain point can be predicted accurately within 5 % for most cases. A larger difference of 9.23 % is seen for Case B at Point 4. Furthermore, the largest vertical acceleration is noted in the chain locker (Points 3 and 5) for Case B, when the vessel was travelling through stormy seas.

B.5 Conclusion

Linear acceleration data obtained from the full-scale measurement champaign was used in the SAM to determine the angular velocity of the vessel. The validation of this method found that the linear acceleration can be predicted within 5 % accuracy of the measured linear acceleration. Having determined the angular velocities successfully, data can be used in the Kalman filter algorithm to determine roll and pitch motion.

Table B.1: Predicted vs. measured rms shown for all six case studies at various locations on the vessel

Case no.	RMS [m/s^2]	Point ID					
		2 (x)	2 (y)	2 (z)	3	4	5
A	Measured	0.27	0.38	0.39	0.87	0.32	0.89
	Predicted	0.27	0.38	0.38	0.89	0.34	0.89
	% Difference	-0.85	-0.03	0.03	0.38	4.28	0.08
B	Measured	0.43	0.73	0.57	1.37	0.66	1.37
	Predicted	0.43	0.73	0.57	1.39	0.72	1.34
	% Difference	-0.91	0.09	0.11	1.58	9.23	1.42
C	Measured	0.27	0.37	0.41	0.83	0.34	0.83
	Predicted	0.25	0.37	0.41	0.84	0.36	0.84
	% Difference	-4.23	-0.04	0.03	1.07	5.04	0.66
D	Measured	0.18	0.24	0.23	0.53	0.24	0.52
	Predicted	0.18	0.24	0.23	0.52	0.25	0.52
	% Difference	-1.56	-0.10	0.18	-1.82	2.86	-0.09
E	Measured	0.16	0.28	0.25	0.54	0.26	0.55
	Predicted	0.18	0.28	0.25	0.54	0.27	0.54
	% Difference	-4.81	-0.14	0.08	-0.74	2.85	-0.91
F	Measured	0.30	0.44	0.43	0.97	0.39	0.96
	Predicted	0.29	0.45	0.43	0.97	0.38	0.97
	% Difference	-3.48	-0.02	0.09	-0.52	0.16	1.05

Appendix C

Sensitivity analysis of the motion prediction in irregular seas

In Chapter 4, the motion response spectra was predicted and compared with measured results. The results showed that some differences exist, especially for cases C and F. In addition to this, the roll motion of the ship showed various discrepancies in all case studies. Therefore, a a sensitivity analysis was conducted to investigate influencing parameters.

The methodology presented by (Skandali, 2015) was applied to conduct the sensitivity analysis.

C.1 Sensitivity analysis

The parameters that are analysed include the sea state parameters (i.e. H_s, T_p and χ), the speed of the vessel (U), and the loading conditions of the vessel (i.e. GM, k_{44} and k_{55}). These parameters are increased and decreased below the original values to investigate the effect on the significant amplitude and peak period of the motion response. The difference in the parameter, δx, is calculated by taking the difference between the new value x_{new} and the original value $x_{original}$ of the parameter as follows (Skandali, 2015):

$$\delta x = \frac{x_{new} - x_{original}}{x_{original}} 100\%. \tag{C.1}$$

The percentage changes in the amplitude and the peak period of the heave, roll and pitch response are calculated similarly.

The values of the original and adapted parameters are presented in Table C.1.

Table C.1: Investigated parameters for sensitivity analysis.

Parameter		Original	Increased value	% Increase	Decreased value	% Decrease
H_s	[m]	3	4	+33.3 %	2	−33.3 %
T_p	[s]	10	13	+30 %	7	−30 %
χ	[deg]	140	170	+21.4 %	110	−21.4 %
U	[kn]	12	16	+25 %	8	−25 %
GM	[m]	1.63	2.03	+24.5 %	1.23	−24.5 %
k_{44}	[m]	8.12	9.34	+15 %	6.91	−15 %
k_{55}	[m]	26.8	30.7	+15 %	22.7	−15 %

C.2 Results

The affect of increasing and decreasing the parameters of interest in the significant amplitude and peak period are summarised in Tables C.2 and C.3, respectively. Furthermore, Figures C.1−C.7 show the resultant response spectra obtained during the sensitivity analysis.

Table C.2: The affect of increasing and decreasing the investigated parameters on the magnitude of the significant amplitude of the response.

	$\delta\xi_{3,1/3}$ [%]		$\delta\xi_{4,1/3}$ [%]		$\delta\xi_{5,1/3}$ [%]	
	Decreased	Increased	Decreased	Increased	Decreased	Increased
H_s	-33.33	33.35	-33.5	33.34	-33.34	33.34
T_p	-62.37	35.32	-29.91	44.78	-43.22	-4.88
χ	-27.08	78.81	-72.09	21.93	-13.68	3.16
U	-9.39	11.4	16.39	-12.34	-0.73	0.27
GM	-0.07	0.31	-4.94	35.94	-0.03	0.04
k_{44}	0.15	0.15	-5.29	13.87	-0.44	-0.08
k_{55}	4.44	-3.36	1.27	-1.38	2.75	-3.71

Table C.3: The affect of increasing and decreasing the investigated parameters on the peak period of the response.

	$\delta T_{p,3}$ [%]		$\delta T_{p,4}$ [%]		$\delta T_{p,5}$ [%]	
	Decreased	Increased	Decreased	Increased	Decreased	Increased
H_s	0	0	0	0	0	0
T_p	-20.92	30.11	-17.52	102.78	-14.29	13.39
χ	6.12	-12.96	8.96	78.05	9.1	-20.52
U	10.96	-10.47	11.46	-8.75	9.93	-7.7
GM	-0.24	0	0	67.82	-0.01	-0.01
k_{44}	0	0	-0.14	83.97	0	-0.01
k_{55}	-1.63	0.8	-0.69	-0.01	1.41	-0.01

Based on the results obtained, the following observations are made:

- The amplitude of the motion response are directly proportional to H_s, but does not affect peak period of the response.
- The heave response increases with an increase in T_p. This is expected since the heave RAOs (depicted in Figure 4.7), showed that heave had a larger response at lower frequencies. Roll response shows a significant peak when T_p is close to the roll natural frequency of 0.06 Hz (14 s). The pitch response shows the largest amplitude motion when $T_p = 10\ s$.
- For the wave encounter angle, χ, it is observed that the roll responses of the ship increases in beam, whereas the pitch response decreases. It is also noteworthy that roll shows a significant peak at a lower frequency in beam seams.
- Ship speed, U, had a small effect on the heave and pitch motion of the ship. However, the vessel has larger roll response at lower speeds.
- The transverse metacentric height, GM, has negligibly small affect on heave and pitch. Decreasing GM leads to a slight decrease in the magnitude of the roll motion and vice versa.
- The roll radii of gyration, k_{44}, has little effect on heave and pitch, but significantly influences roll. As expected, a decrease in k_{44} leads to a significant increase in the roll response. On the other hand, if it is increased, the response it decreases in terms of percentage.
- The pitch radii of gyration, k_{55}, influences all the responses similarly. An decrease of k_{55} leads to an increase in the responses and vice versa.

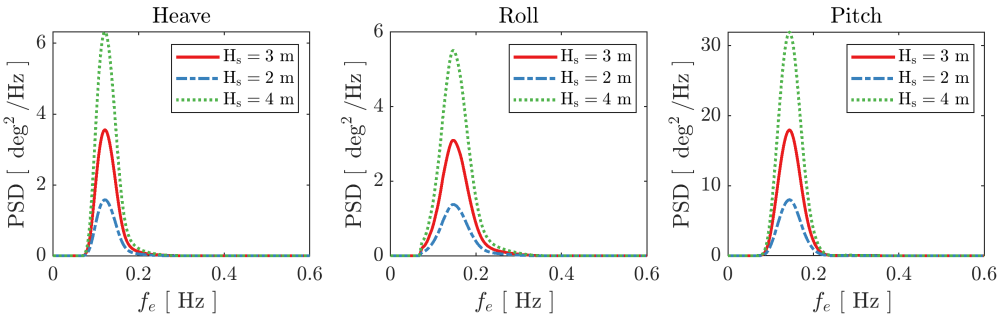

Figure C.1: Sensitivity analysis of significant wave height.

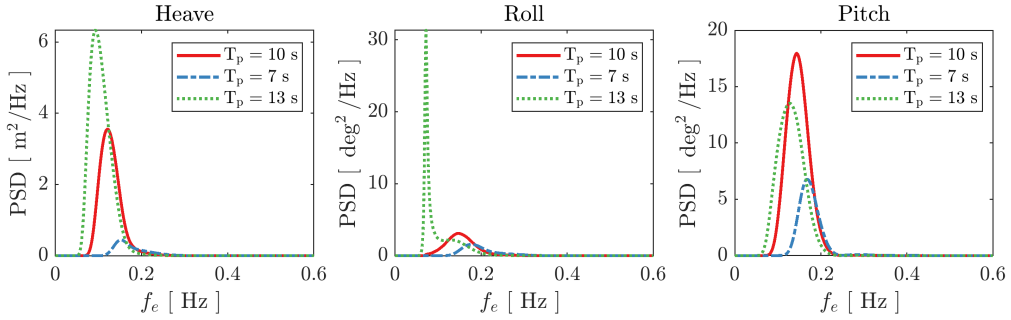

Figure C.2: Sensitivity analysis of peak period.

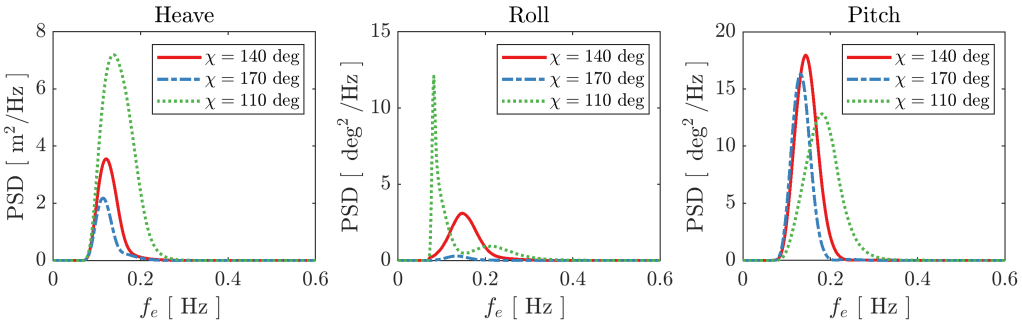

Figure C.3: Sensitivity analysis of wave encounter angle.

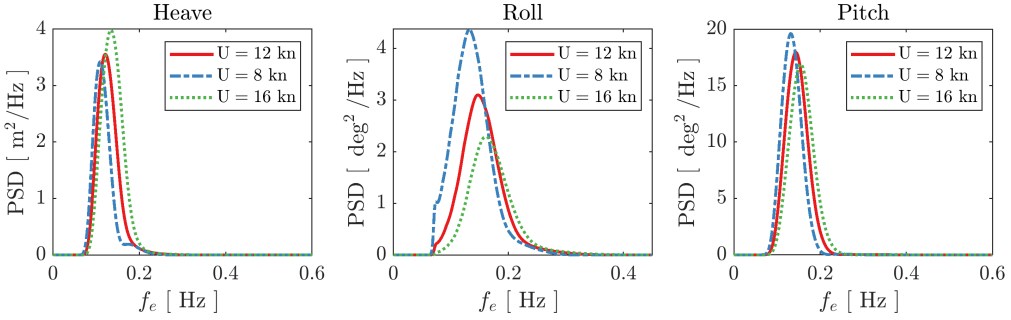

Figure C.4: Sensitivity analysis to ship speed.

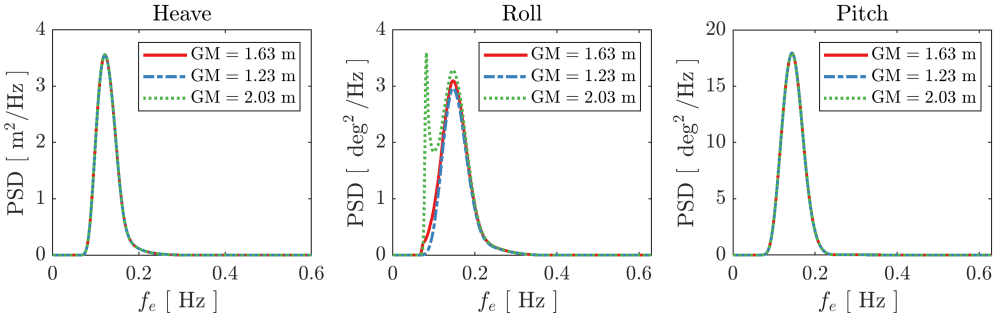

Figure C.5: Sensitivity analysis of metacentric height.

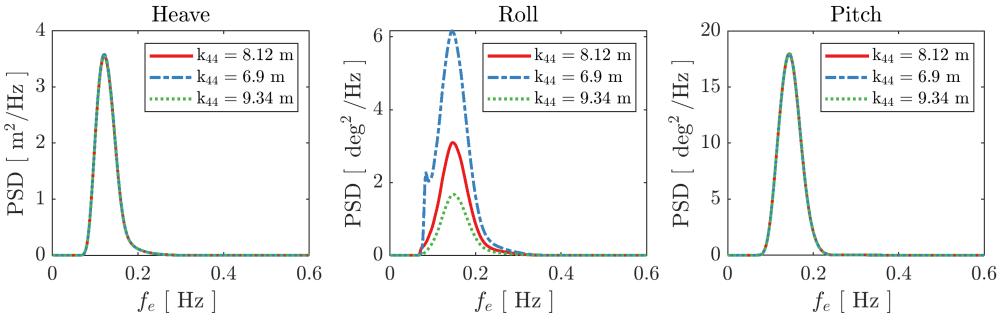

Figure C.6: Sensitivity analysis of roll radii of gyration.

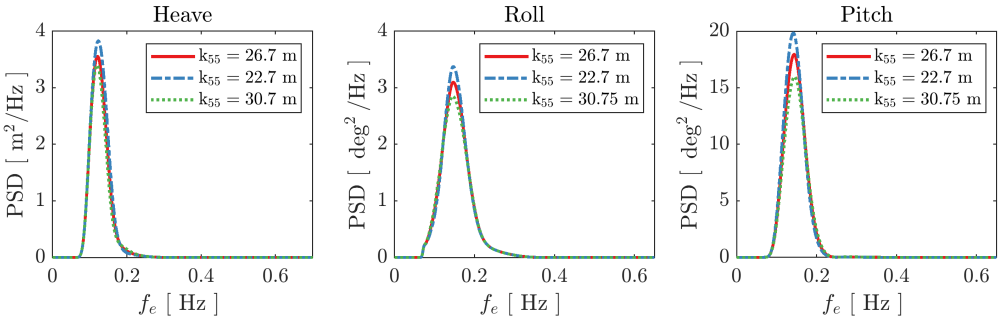

Figure C.7: Sensitivity analysis of pitch radii of gyration.

C.3 Conclusion

This chapter presented a sensitivity analysis of the prediction of the motion response in irregular seas. The results indicate that the prediction of motion response is primarily influenced by the sea state parameters, such as the wave encounter direction. In addition to this, the roll response was significantly influenced by the roll radii of gyration and the transverse metacentric height. Therefore, care should be taken when specifying these parameters in hydrodynamic software.

Appendix D

CFD Verification and Validation study

In Chapter 5, the CFD investigation of the SA Agulhas II is presented. This chapter presents a Verification and Validation (V&V) study, which is a vital tool for the interpretation of numerical simulation results (ITTC, 2011).

D.1 Vessel specifications and investigated conditions

When possible, CFD simulations are verified by comparing it with results obtained from Experimental Fluid Dynamics (EFD). The present did not have access to EFD for the SA Agulhas II. Therefore, the Kriso Container Ship (KCS) was chosen to conduct the V&V study. The KCS is a conceptual modern containership with a bulbous bow that was developed by the Korean Maritime and Ocean Engineering Research Institute (KRISO). She was specifically designed to provide experimental data for flow physics (Carrica *et al.*, 2011). Therefore, she has been used in various seakeeping CFD studies (Tezdogan *et al.*, 2015).

The geometry of the KCS was obtained from NUMECA International (2020*a*) and is shown in Figures D.1. The main characteristics were obtained from the study presented by Tezdogan *et al.* (2015) and are shown in Table D.1.

EFD data regarding this vessel is widely available. For this study, calm water EFD data was obtained from Case 2.1 of the Tokyo 2015 workshop

Figure D.1: Side view of the KCS geometry.

Table D.1: Main characteristics of the KCS (Tezdogan *et al.*, 2015)

Details	
Length between perpendiculars (L_{BP})	230.0 m
Length of waterline (L_{WL})	232.5 m
Beam at waterline (B_{WL})	32.2 m
Depth (D)	19.0 m
Design draft (T)	10.8 m
Displacement (Δ)	52,030 m^3
Block coefficient (C_B)	0.6505
Ship wetted area with rudder (S)	9539 m^2
Longitudinal centre of buoyancy (LCB) ($\%L_{BP}$), fwd +	-1.48
Longitudinal centre of gravity (LCG) from the aft peak	111.603 m
Vertical centre of gravity (KG) from keel	7.28 m
Metacentric height from keel (GM_t)	0.60 m
Roll radius of gyration, k_{44}	$0.40B$
Pitch radius of gyration k_{55}	$0.25L_{BP}$
Yaw radius of gyration , k_{66}	$0.25L_{BP}$

(National Maritime Research Institute, 2015). During these experiments a 1:31.6 model-scale ship was towed at $0.92 - 2.38$ m/s, i.e. Fn ranging from $0.11-0.28$. The corresponding speeds at full-scale range from $10-26$ kn ($5.14-13.38$ m/s). CFD simulation results will be compared with the resistance, trim and sinkage in calm water.

Experimental studies of a 1:52.667 model of the KCS in head waves were conducted by Simonsen *et al.* (2013) and Otzen and Simonsen (2010) at FORCE Technology's towing tank in Denmark. During these experiments, the heave and pitch motion and the resistance of the vessel in waves were evaluated at various speeds. The results of these experiments were obtained from Tezdogan *et al.* (2015). To validate the present CFD study using FINE^{TM}/Marine, three cases were investigated. The parameters of the wave conditions are shown in Table D.2. For all three cases, the full-scale ship was travelling at a speed of 24 kn ($Fn = 0.26$). According to Tezdogan *et al.* (2015), the natural heave and pitch frequency of the KCS is $f_n = 0.124$ Hz. Therefore, Case 1 is chosen to conduct the verification study.

The heave and pitch motion responses and resistance are evaluated during the CFD simulations and compared with EFD data. To investigate the consistency of the CFD simulations, the results are also compared with other CFD studies presented by Simonsen *et al.* (2013), Tezdogan *et al.* (2015), Carrica *et al.* (2011), Manzke and Rung (2010) and Akimoto *et al.* (2010).

Table D.2: Investigated conditions for the V&V study

Case no.	U [kn]	Fn	λ (m)	λ/L_{pp}	H_w (m)	f_e (Hz)
1	24	0.26	265	1.15	4.43	0.124
2			307	1.33	5.11	0.112
3			460	2	7.67	0.085

D.2 Scaling resistance from model-scale to full-scale

The full-scale KCS geometry was used in the CFD simulations, while the resistance tests of the KCS were conducted using a geometrically similar model-scale experiments in towing tanks. Therefore, it is required to convert the model-scale resistance to full-scale (Bertram, 2012). In order to achieve this, the ITTC-1957 method was used, presented by (Tezdogan *et al.*, 2015).

The total drag force, $F_{x,T}$, acting upon a vessel is comprised of residuary and frictional resistance forces, $F_{x,R}$ and $F_{x,F}$, as follows Tezdogan *et al.* (2015):

$$F_{x,T} = F_{x,R} + F_{x,F} \tag{D.1}$$

which can be expressed in dimensionless form by the total resistance coefficient, see Equation 5.14, as follows:

$$C_T = C_R(Fn) + C_F(Re) \tag{D.2}$$

where C_R and C_F are defined as the residuary and frictional resistance coefficients, respectively. C_R is a function of the Froude number (Fn), while C_F is a function of the Reynolds number (Re).
The residuary resistance coefficient for model-scale and full-scale ship remains constant (Bertram, 2012). However, the frictional resistance coefficient C_F for model-scale and full-scale vessels differ and is defined according to the ITTC-1957 formula:

$$C_F = \frac{0.075}{(\log_{10} Re - 2)^2} \tag{D.3}$$

To summarize, the total resistance coefficient of the full scale ship C_{Ts} is calculated as follows:

$$C_{Ts} = C_{Fs} + C_{Tm} - C_{Fm} \tag{D.4}$$

Unless stated otherwise, the calm water resistance coefficient of the full-scale vessel, C_{Ts}, is from now on referred using the symbol C_T.

D.3 Verification and Validation methodology

According to the ITTC (2017*b*) verification is "a process for assessing simulation and numerical uncertainty (U_{SN})." Whereas, validation is "a process for assessing simulation modelling uncertainty by using benchmark experimental data." The methodology of the verification and validation study was adopted from Stern *et al.* (2006), but was also presented by the ITTC (2017*b*), Kim *et al.* (2017) and Jin *et al.* (2017).

D.3.1 Verification study

Simulation and numerical uncertainties, U_{SN}, comprises of iterative, grid size, and time-step size uncertainties(i.e. U_I, U_G and U_T) as follows (ITTC, 2017*b*):

$$U_{SN}^2 = U_I^2 + U_G^2 + U_T^2 \tag{D.5}$$

To estimate U_G and U_T, convergences studies are conducted by systematically refining the ith input parameters, i.e. grid size or time step size, while all other input parameters remain constant. Multiple solutions are obtained from which the simulation numerical uncertainty can be determined. The parameter refinement ratio, r_i, between multiple solutions is defined as follows :

$$r_i = \Delta x_{i,2}/\Delta x_{i,1} = \Delta x_{i,3}/\Delta x_{i,2} \tag{D.6}$$

Information regarding the the grid and the time-step size during the V&V study is listed in Table D.3. As mentioned previously, Case 1 was chosen to investigate the grid size and time-step size dependency study. In accordance with the (ITTC, 2017*b*), a uniform grid refinement ratio, r_G, of $\sqrt{2}$ was chosen for the grid convergence study. This was conducted by generating a fine mesh, which was systematically coarsened. A time-step refinement ratio, r_T, of 2 was chosen. For the time-step convergence study, the time-step size, Δt, was discretized based on the number of time steps per encountered wave period, T_e. Notice that the coarsest time step, $T_e/100$, is chosen based on the recommendations in (ITTC, 2014*a*). It is also worth noting that the grid convergence study was conducted using the smallest time-step, while the time-step convergence study was conducted using the finest mesh.

The changes between the coarse (S_3), medium, (S_2) and fine (S_1) simulation results are defined as follows:

$$\varepsilon_{i,32} = S_3 - S_2 \tag{D.7}$$

$$\varepsilon_{i,21} = S_2 - S_1 \tag{D.8}$$

From which the convergence ratio, R_i, can be calculated as follows:

$$R_i = \varepsilon_{i,21}/\varepsilon_{i,32} \tag{D.9}$$

Table D.3: Information of the grid and time-step size used in the V&V study

		Number of cells	Δt
Calm water		1 788 272	$0.005(L_{OA}/V_{ref})$
	Coarse	2 196 316	$T_e/100$
Case 1	Medium	2 986 439	$T_e/200$
	Fine	4 432 019	$T_e/400$
Case 2		2 617 485	$T_e/200$
Case 3		1 839 675	$T_e/200$

According to Stern *et al.* (2006) four convergence conditions may be seen:

(i) Monotonic convergence: $0 < R_i < 1$

(ii) Oscillatory convergence: $0 < R_i$; $|R_i| < 1$

(iii) Monotonic divergence: $R_i > 1$

(iv) Oscillatory divergence: $R_i > 1$; $|R_i| > 1$

For conditions (iii) and (iv) uncertainties can not be estimated. For condition (ii), the uncertainty is estimated as follows:

$$U_i = \left| \frac{S_U - S_L}{2} \right| \tag{D.10}$$

where S_U and S_L the maximum and minimum values of the solution, respectively.

For condition (i) the uncertainty is calculated using the generalized Richardson extrapolation (RE). According to the RE approach, the estimated error, $\delta^*_{RE_{i,1}}$, and the order of accuracy, p_i, is calculated as follows:

$$\delta^*_{RE_{i,1}} = \frac{\varepsilon_{i,21}}{r_i^{p_i} - 1} \tag{D.11}$$

$$p_i = \frac{\ln(\varepsilon_{i,32}/\varepsilon_{i,21})}{\ln(r_i)} \tag{D.12}$$

The correction factor, C_i, is defined as follows:

$$C_i = \frac{r_i^{p_i} - 1}{r_i^{p_{i_{est}}} - 1} \tag{D.13}$$

where $p_{i_{est}}$ is an estimate for the limiting order of accuracy for which a value of 4 is chosen based on the convergence criteria specified in Centrale Nantes (2020*b*). The numerical uncertainty, U_i, can then calculated as follows

$$U_i = \begin{cases} (9.6(1-C_G^2)+0.1)\left|\delta^*_{RE_{i,1}}\right| & |1-C_G| \leq 0.125 \\ (2\,|1-C_G|+1)\left|\delta^*_{RE_{i,1}}\right| & |1-C_G| \geq 0.125 \end{cases} \tag{D.14}$$

The methodology discussed above was applied to determine the grid size uncertainty, U_G, and the time-step size uncertainty, U_T. Iterative uncertainty, U_I is not reported in this study. Similar studies have found it to be negligibly small when compared to U_G and U_T (Tezdogan *et al.*, 2015). Other studies presented by De Marco *et al.* (2017), Jin *et al.* (2017) and D'Aure *et al.* (2015) followed a similar approach.

D.3.2 Validation study

In the validation study, numerical and simulation uncertainty is evaluated by comparing it with comparing it with benchmark EFD data. Firstly, the comparison error, E, is defined as follows (ITTC, 2017*b*):

$$E(\,\%D) = \frac{D-S}{D} \times 100 \tag{D.15}$$

where D refers to EFD data, and S refers to the simulation results.

The validation uncertainty, U_V, is calculated as follows:

$$U_V = \sqrt{U_{SN}^2 + U_D^2} \tag{D.16}$$

where U_D is referred to the experimental uncertainty.

For validation to be achieved, it is required that $|E| < U_V$ (Stern *et al.*, 2006). If the comparison error is much larger than the validation uncertainty ($E \gg U_V$), validation is not achieved and it is recommended to make improvements to simulation modelling (De Marco *et al.*, 2017).

D.4 Results

D.4.1 Verification study

The results of the grid size and time-step size verification studies are shown in Tables D.4 and D.5. For the grid size verification study, monotonic convergence is achieved for heave and pitch amplitude, as well the total resistance coefficient. For the time step size verification study, oscillatory convergence is seen for heave and pitch amplitude, while monotonic convergence is achieved for the total resistance coefficient. Further, it is seen that small levels of numerical uncertainty, U_G, were calculated for the heave and pitch RAOs, and the total resistance coefficient, while the estimated values for U_T is slightly larger than U_G. This implies that the responses are more sensitive to time-step size, especially for the resonant case. For other cases, it is expected that

the values of the estimated uncertainty will be smaller than the resonant case (Tezdogan *et al.*, 2015).

Table D.4: Grid size verification results

		Solutions							
	r_G	S_1	S_2	S_3	R_G	p_G	δ^*_{RE} (%S1)	U_G (%S_1)	EFD
A_3	$\sqrt{2}$	1.007	1.004	0.913	0.140	5.67	-0.008	0.782	0.950
A_5	$\sqrt{2}$	0.933	0.932	0.913	0.066	7.86	-0.008	0.074	0.943
$C_T \times 10^3$	$\sqrt{2}$	4.945	4.910	4.730	0.891	1.41	-0.171	0.288	5.133

Table D.5: Time-step size verification results

		Solutions							
	r_T	S_1	S_2	S_3	R_T	p_G	δ^*_{RE} (%S1)	U_T (%S_1)	EFD
A_3	2	1.007	1.070	0.983	-0.483		-	3.522	0.95
A_5	2	0.933	0.938	0.865	-0.069		-	3.909	0.943
$C_T \times 10^3$	2	4.945	4.976	5.038	0.855	1.01	0.630	1.797	5.133

D.4.2 Validation study

The validation results of the CFD study is shown in Table D.6. According to Tezdogan *et al.* (2015), an experimental uncertainty of 5.83 % was presented in the study by Simonsen *et al.* (2013).

For validation to be achieved, it is required that the validation uncertainty, U_V, is larger than the absolute value average comparison error, $|E|$. This has been achieved for the heave and pitch RAOs and the total resistance coefficient. Therefore, validation achieved at the U_V level (ITTC, 2017*b*).

Table D.6: Validation results of the CFD study

	$U_{SN}(\%D)$	$U_D(\%D)$	$U_V(\%D)$	$E(\%D)$
A_3	4.59	5.83	7.88	-4.98
A_5	3.87	5.83	6.99	-1.38
C_T	1.75	5.83	6.09	2.34

Since validation has been achieved for Case 1, the CFD simulations of calm water conditions and seakeeping simulations of Cases 1, 2 and 3 are further compared with experimental data and other CFD studies. The results are discussed below.

D.4.3 Calm water resistance

An illustration of the calculation of the full-scale resistance coefficient, C_T, from the model scale experiments at $Fn = 0.26$ is shown in Table D.7. Comparisons of the calm water resistance coefficient results obtained from the CFD simulations and EFD data are shown in Figure D.2 and Table D.8. It is seen that the comparison error is below 10 % for all speeds investigated.

Table D.7: Calculation of full-scale resistance coefficient, C_T, from model-scale experiments at $Fn = 0.26$

	Model-scale EFD	Full-scale EFD
Re	1.26×10^7	2.24×10^9
C_R	8.27×10^{-4}	8.27×10^{-4}
C_F	2.90×10^{-3}	1.40×10^{-3}
C_T	3.71×10^{-3}	2.21×10^{-3}

Table D.8: Comparison of EFD and CFD results of the total drag resistance coefficient of the KCS

Fn	Re	$C_T \times 10^{-}3$ (EFD)	$C_T \times 10^{-}3$ (CFD)	E (%D)
0.11	9.32×10^8	1.97	1.81	-8.47
0.15	1.31×10^9	1.95	1.819	-7.45
0.20	1.68×10^9	1.88	1.76	-5.15
0.23	2.05×10^9	1.92	1.92	-0.39
0.26	2.24×10^9	2.21	2.13	-3.89
0.28	2.42×10^9	3.03	2.96	-2.49

The calm water sinkage normalised with the ship length, $\xi_{3,0}/L_{pp}$, and trim results, $\xi_{5,0}$, are shown in Table D.9 and Figure D.3. The maximum E calculated for the sinkage is 136 %. Although this error seems high in terms of percentage, the actual difference only 3.91 cm for the full-scale ship. For trim angle, a maximum E of 44.48 % is seen. For both sinkage and trim, E decreases as ship speed increases. D'Aure *et al.* (2015) suggest that the large comparative errors of the sinkage and trim motion of a vessel at the lowest Froude number could be ascribed to the mesh properties. At low Froude numbers, the motion of the vessel is significantly small compared to the vertical cell size. As the Froude number increases, the motion increases and is better predicted by CFD. Since the prediction the drag force is of more importance than the sinkage and trim motion of the vessel, it can be concluded that the results obtained are sufficient. Also, considering that a mesh resolution of 1.78 million cells was used, the CFD results are reasonably accurate and compatible with the EFD data.

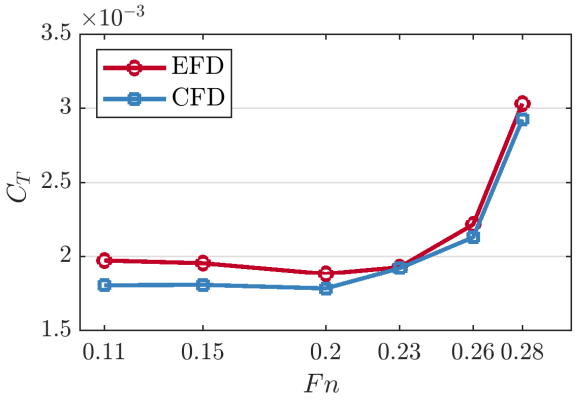

Figure D.2: Illustration of the EFD and CFD calm water resistance coefficient results of the KCS

Table D.9: A comparison of EFD and CFD results of the sinkage and trim for the KCS.

Fn	$\xi_{3,0}/L_{PP}$			$\xi_{5,0}$ [deg]		
	EFD	CFD	E(%D)	EFD	CFD	E(%D)
0.11	-1.2×10^{-4}	-2.9×10^{-4}	136	−0.017	−0.025	44.5
0.15	-3.8×10^{-4}	-5.7×10^{-4}	52.1	−0.053	−0.051	-3.39
0.20	-8.2×10^{-4}	-9.9×10^{-4}	20.2	−0.097	−0.093	-4.58
0.23	-1.3×10^{-3}	-1.59×10^{-3}	22.7	−0.127	−0.136	6.97
0.26	-1.9×10^{-3}	-2.02×10^{-3}	5.58	−0.169	−0.169	-0.06
0.28	-2.3×10^{-3}	-2.42×10^{-3}	3.36	−0.159	−0.136	-14.5

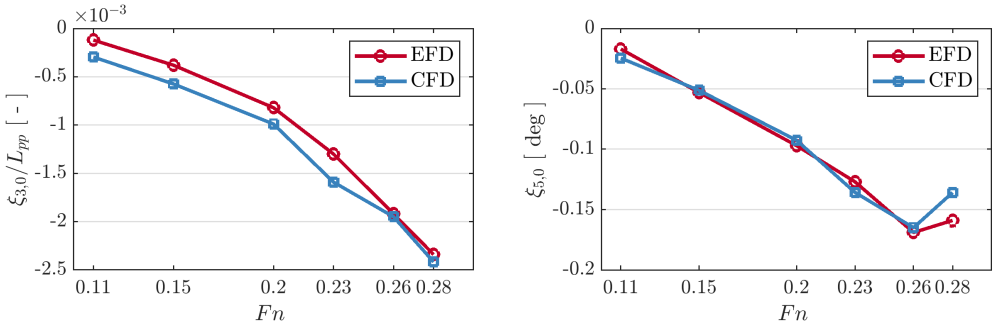

(a) Sinkage (b) Trim

Figure D.3: Illustration of the EFD and CFD results for the non-dimensional sinkage and trim

D.4.4 Motion and added resistance of KCS in waves

In order to further validate the present seakeeping CFD study, the results obtained for Cases 1, 2 and 3 are compared with experimental data and other

CFD studies. A comparison of the heave and pitch motion amplitude, as well as the resistance coefficient and added wave resistance coefficient is presented in Table D.10. Notice that pitch motion amplitude is given in deg/m. It is seen the comparison error for the present study for heave, pitch and the resistance coefficient is under 10 %. For the added wave resistance coefficient, the maximum E of 14.34 % is observed. Nevertheless, the results presented for this study are consistent with other CFD studies.

Table D.10: A comparison of the CFD and EFD results for heave amplitude (A_3), pitch amplitude (A_5), resistance coefficient ($C_{T,0}$) and added wave resistance coefficient (C_{aw}).

Case		A_3	A_5	$C_{T,0}$ $\times 10^{-3}$	C_{aw}
3	EFD (Simonsen *et al.*, 2013)	0.95	0.94	5.13	11.05
	CFD (Tezdogan *et al.*, 2015)	0.94	0.91	4.64	9.11
	E (%D)	-0.42	-4.18	-9.53	-17.59
	CFD (Simonsen *et al.*, 2013)	0.99	1.05	5.01	11.54
	E (%D)	4.73	10.97	-2.35	4.44
	CFD (Simonsen *et al.*, 2013)	0.86	0.99	4.25	6.95
	E (%D)	-9.36	-5.48	-17.15	-37.11
	Present CFD	1.03	0.93	4.94	10.16
	E (%D)	8.94	-1.15	-3.66	-8.03
4	EFD (Simonsen *et al.*, 2013)	1.10	1.14	5.84	8.62
	CFD (Tezdogan *et al.*, 2015)	1.00	0.89	5.48	8.29
	E (%D)	-9.50	-9.19	-6.20	-3.79
	CFD (Simonsen *et al.*, 2013)	0.95	1.13	5.29	9.49
	E (%D)	-14.10	-1.24	-9.42	10.18
	Present CFD	1.11	0.96	6.41	9.850
	E (%D)	0.45	-1.33	9.70	14.34
6	EFD (Otzen and Simonsen, 2010)	0.90	1.22	4.14	1.92
	CFD (Tezdogan *et al.*, 2015)	0.84	1.27	3.79	1.72
	E (%D)	-5.99	4.62	-8.49	-10.39
	CFD (Carrica *et al.*, 2011)	0.85	1.17	4.18	-
	E (%D)	-5.21	-4.24	0.95	-
	CFD (Manzke and Rung, 2010)	0.89	1.23	5.99	-
	E (%D)	-1.11	0.68	44.56	-
	CFD (Akimoto *et al.*, 2010)	1.25	1.22	5.99	-
	E (%D)	39.29	0	44.56	-
	Present CFD	0.94	1.34	4.50	2.10
	E (%D)	4.36	9.93	8.54	9.71

D.5 Concluding remarks

A V&V study was undertaken using NUMECA FINE^{TM}/Marine Version 8.2. The full-scale KCS was evaluated in calm water conditions and in head waves. The resonant condition was used to quantify the validation uncertainties. Using the Richardson extrapolation method, the validation uncertainty levels for the heave and pitch RAOs, and the total resistance coefficient were calculated as 7.88 %, 6.99 % and 6.09 %, respectively. Furthermore, the average comparison error was smaller than th validation uncertainty.

Quantitative comparisons of experimental data and CFD results showed that FINE^{TM}/Marine is capable to accurately predict the calm water and seakeeping behaviour of a ship. In addition to this, the results were consistent with various other CFD studies.

Furthermore, the results may be deemed satisfactory, considering the mesh resolution and time-step size used in the present study. Tt would be beneficial to use the finest mesh and smallest time-step for all simulations, since it proved to have the smallest comparison error. However, this results in an increase in computational cost and time. Therefore, for simulations performed using the SA Agulhas II, a medium sized mesh and time-step was used.

Appendix E

Additional figures

E.1 CFD

An example of the 8$^{\text{th}}$ order FS used to evaluate the unsteady time series of the incident wave elevation, drag force, as well as the heave and pitch motion is shown in Figure E.1. Notice that the FS was applied to the last 10 wave encounters.

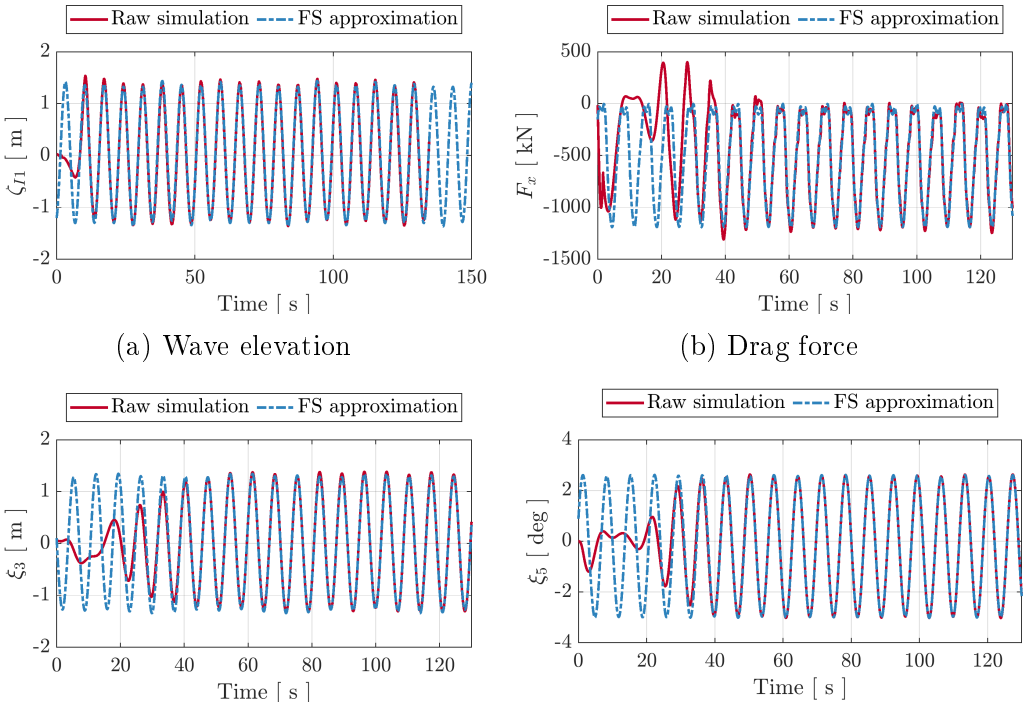

(a) Wave elevation

(b) Drag force

(c) Heave motion

(d) Pitch motion

Figure E.1: An illustration of the FS approximation for Case 2.3

E.2 PDSTRIP geometry input

The station curve geometry input for PDSTRIP is shown in Figure E.2.

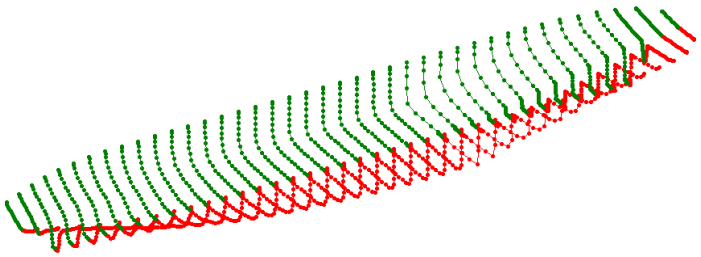

Figure E.2: Station curve geometry input for PDSTRIP.

E.3 Sea state parameters obtained from ECMWF

Figure E.3 depicts the sea state parameters for Case B obtained from the ECMWF ERA5 database (Copernicus Climate Change Service, 2017).

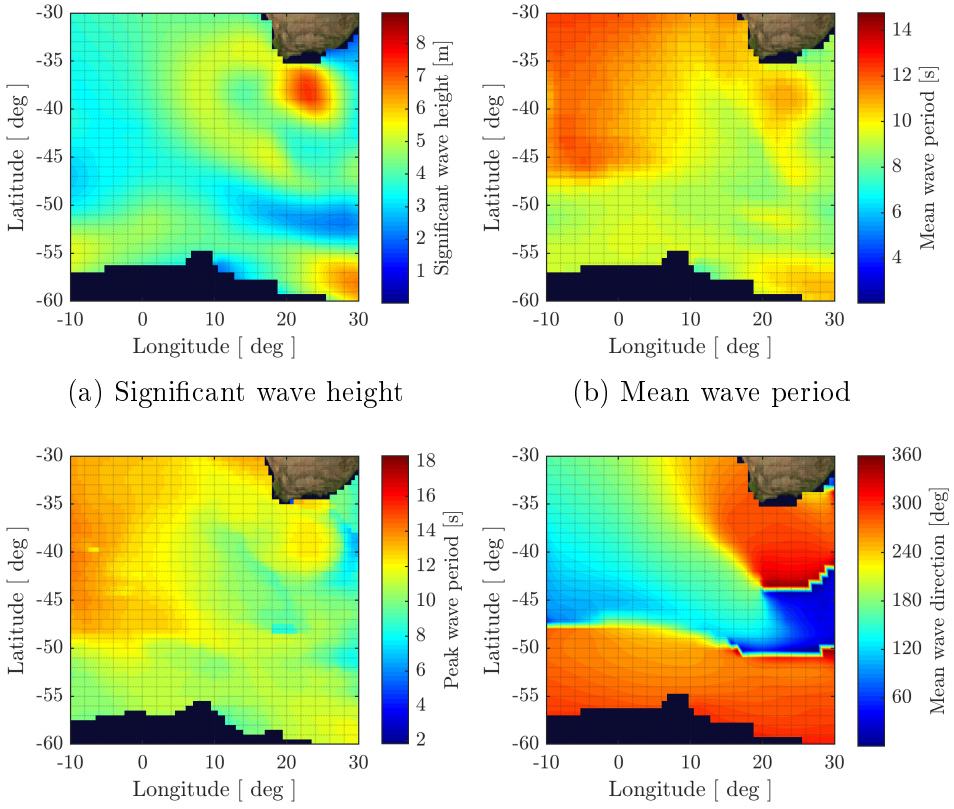

(a) Significant wave height

(b) Mean wave period

(c) Peak wave period

(d) Mean wave direction

Figure E.3: Illustration of sea state parameters for Case B

References

Abankwa, N.O., Johnston, S.J., Scott, M. and Cox, S.J. (2015). Ship motion measurement using an inertial measurement unit. In: *2015 IEEE 2nd World Forum on Internet of Things (WF-IoT)*. IEEE, Milan, Italy.

Ahmad, M. and Adnan, F. (2014 06). Evaluation of service performances of liquefied natural gas carriers in actual seas. *Jurnal Teknologi*, vol. 69, pp. 2180–3722.

Akimoto, H., Omori, T., Saito, H. and Masiur, R. (2010). Numerical simulation of KCS container carrier in head wave conditions. In: *Proceedings from Gothenburg 2010-A Workshop on Numerical Ship Hydrodynamics*. Gothenburg.

American Bureau of Shipping (2011). *Guide for Slamming Loads and Strength Assessment for Vessels*.

Anderson, John D., J.D. (1995). *Computational fluid dynamics: the basics with applications*. McGraw-Hill series in mechanical engineering. McGraw-Hill, New York, N.Y. ISBN 0070016852.

Andrun, M., Blagojević, B. and Bašić, J. (2018). The Influence of Momentum Discretization Schemes in the Finite-Volume Method on the Wigley Hull Resistance. In: *23rd Symposium on Theory and Practice of Shipbuilding SORTA 2018*. Split, Croatia.

Antarctic Legacy of South Africa (2020). South African National Antarctic Programme.
Available at: https://www.sanap.ac.za/

Auestad, O., Gravdahl, J. and Fossen, T. (2013). Heave Motion Estimation on a Craft Using a Strapdown Inertial Measurement Unit. *IFAC Proceedings Volumes*, vol. 46, no. 33, pp. 298–303. ISSN 1474-6670.

Bekhit, A. and Lungu, A. (2019). URANSE simulation for the seakeeping of the KVLCC2 ship model in short and long regular head waves. *IOP Conference Series: Materials Science and Engineering*, vol. 591, p. 012102.
Available at: https://doi.org/10.1088%2F1757-899x%2F591%2F1%2F012102

Bekker, A. (2017). From (Big) Data to Insight – A Roadmap for the "SA Agulhas II". In: *High Performance Marine Vehicles – 10 to 13 September 2017 – Zewenwacht, South Africa*, pp. 212–223. Zewenwacht, South Africa.

Bekker, A. (2018). Exploring the blue skies potential of digital twin technology for a polar supply and research vessel. In: *Proceedings of the 13th International Marine Design*, vol. 1, pp. 135–146. Helsinki, Finland. ISBN 9781138541870.

Belga, F., Sutulo, S. and Guedes Soares, C. (2018). *Comparative study of various strip-theory seakeeping codes in predicting heave and pitch motions of fast displacement ships in head seas.* ISBN 9781138585393.

Bender, I.C., Guinasso, J.L., Walpert, J.N. and Howden, S.D. (2010). A comparison of methods for determining significant wave heights-applied to a 3-m discus buoy during Hurricane Katrina. *Journal of Atmospheric and Oceanic Technology*, vol. 27, no. 6, pp. 1012–1028. ISSN 07390572.

Bergdahl, L. (2008). Wave-induced loads and ship motions. Tech. Rep. 2009:1, Chalmers University of Technology.

Bergqvist, R., Turesson, M. and Weddmark, A. (2015). Sulphur emission control areas and transport strategies -the case of Sweden and the forest industry. *European Transport Research Review*, vol. 7, no. 2.

Bertram, V. (2012). *Practical Ship Hydrodynamics.* 2nd edn. Oxford UK Elsevier Ltd. Publishers. ISBN 9780080971506.

Bertram, V., Veelo, B., Söding, H. and Graf, K. (2006). Development of a freely available strip method for seakeeping. *Proc. 5th International Conference on Computer and IT Applications in the Maritime Industries.*

Bialystocki, N. and Konovessis, D. (2016). On the estimation of ship's fuel consumption and speed curve: A statistical approach. *Journal of Ocean Engineering and Science*, vol. 1, no. 2, pp. 157 – 166. ISSN 2468-0133.

Bieda, R. and Jaskot, K. (2016). Determinig of an object orientation in 3D space using direction cosine matrix and non-stationary Kalman filter. *Archives of Control Sciences*, vol. 26, no. 2, pp. 223–244. ISSN 12302384.

Birk, L. (2019). Ship Hydrodynamics. In: *Fundamentals of Ship Hydrodynamics: Fluid Mechanics, Ship Resistance and Propulsion*, chap. 1, pp. 1–9. John Wiley & Sons, Ltd. ISBN 9781119191575.

Boonstra, R.J. (2019). *Keel-Rudder Interaction.* Masters, Delft University of Technology.

Boulle, B.G. (2016). *Motion sickness and rigid body motion of a polar supply and research vessel on voyages to Antarctica and the Southern Ocean.* Master's Thesis, Stellenbosch University.

Brandt, A. (2010). *Noise and Vibration Analysis: Signal Analysis and Experimental Procedures.* John Wiley & Sons, Ltd. ISBN 978-0-470-74644-8.

Brandt, A. (2018). *ABRAVIBE A MATLAB/Octave toolbox for Noise and Vibration Analysis and Teaching*. 2nd edn.
Available at: https://www.abravibe.com/

Carrica, P.M., Fu, H. and Stern, F. (2011). Computations of self-propulsion free to sink and trim and of motions in head waves of the KRISO Container Ship (KCS) model. *Applied Ocean Research*, vol. 33, no. 4, pp. 309–320. ISSN 01411187.
Available at: http://dx.doi.org/10.1016/j.apor.2011.07.003

Castiglione, T., Stern, F., Bova, S. and Kandasamy, M. (2011). Numerical investigation of the seakeeping behavior of a catamaran advancing in regular head waves. *Ocean Engineering*, vol. 38, no. 16, pp. 1806–1822. ISSN 00298018.

Centrale Nantes (2020*a*). *Theory Guide - FINE®/Marine 8.2.*

Centrale Nantes (2020*b*). *User Guide - FINE™/Marine 8.2.*

Chen, C., Liu, Y.-d., He, Y.-p. and Li, X.-y. (2020). Numerical analysis of added resistance on an icebreaker in regular waves. *Journal of Marine Science and Technology*. ISSN 1437-8213.
Available at: https://doi.org/10.1007/s00773-020-00745-2

Chen, L., He, G., Wang, D. and Zhang, J. (2015). Computation of wave-making resistance on high speed catamaran using FINE/Marine. In: *Proceedings of the International Offshore and Polar Engineering Conference*, vol. 2015-Janua, pp. 983–988. Hawaii, USA. ISBN 9781880653890. ISSN 15551792.

Copernicus Climate Change Service (2017). ERA5: Fifth generation of ECMWF atmospheric reanalyses of the global climate.
Available at: https://cds.climate.copernicus.eu/cdsapp{#}!/home

D'Aure, B., Mallol, B. and Hirsch, C. (2015). Resistance and Seakeeping CFD Simulations for the Korean Container Ship. In: *Proceedings of the Tokyo 2015: A Workshop on CFD in Ship Hydrodynamics*, pp. pp. 359–364.

de Carvalho Ribeiro Belga, F. (2017). *Seakeeping optimization of a fast displacement catamaran on the basis of strip-theory codes Naval Architecture and Marine Engineering Examination Committee*. Masters Thesis, Técnico Lisboa.

de Jong, P. (2005). *Investigation of Nonlinearities in the Superposition of Ship Motions by 6DOF Forced Oscillations*. Masters thesis, Delft University of Technology.

De Marco, A., Mancini, S., Miranda, S., Scognamiglio, R. and Vitiello, L. (2017). Experimental and numerical hydrodynamic analysis of a stepped planing hull. *Applied Ocean Research*, vol. 64, pp. 135–154. ISSN 01411187.
Available at: http://dx.doi.org/10.1016/j.apor.2017.02.004

Deng, G.B., Queutey, P. and Visonneau, M. (2010). RANS prediction of the KVLCC2 tanker in head waves. *Journal of Hydrodynamics*, vol. 22, no. 5 SUPPL. 1, pp. 476–481. ISSN 10016058.
Available at: http://dx.doi.org/10.1016/S1001-6058(09)60239-0

Devanunthan, N. (2019). The SA Agulhas II: Operations and Logistics. Presented at the SA Agulhas II mini conference in Stellenbosch, South Africa.

DNV GL (2012). DNV GL Vessel Register - SA Agulhas II (30528). Available at: https://vesselregister.dnvgl.com/VesselRegister/vesseldetails.html?vesselid=30528

DNVGL (2018). *Wave loads Class guideline DNV GL−CG0130*. January 2018.

Durandt, P. (2020). Data-driven regression models for voyage cost optimisation based on the operating conditions of the sa agulhas ii.

Faltinsen, O. (1990). *Sea loads on ships and offshore structures*. Cambridge University Press, Cambridge, England. ISBN 0521372852.

Fossen, T.I. (2011). *Handbook of Marine Craft Hydrodynamics and Motion Control*. John Wiley & Sons Ltd, Trondheim, Norway. ISBN 9781119994121.

Gourlay, T., von Graefe, A., Shigunov, V. and Lataire, E. (2015). Comparison of Aqwa, GL, Rankine, Moses, Octupus, PDSTRIP, AND WAMIT with Model Test Results For Cargo Ship Wave-Induced Motions in Shallow Water. In: *Proceedings of the ASME 2015 34th International Conference on Ocean, Offshore and Arctic Engineering*. St. John's, Newfoundland, Canada.

Greenwood, D.T. (2003). *Advanced Dynamics*. ISBN 978-0521029933.

Guilmineau, E., Leroyer, A., Visonneau, M. and Ory, E. (2012). CFD analysis of a LNGC carrier in waves. In: *Proceedings of the International Conference on Offshore Mechanics and Arctic Engineering - OMAE*, vol. 5, pp. 773–780. Rio de Janeiro, Brazil. ISBN 9780791844922.

Ha, J.H. and Gourlay, T. (2018). Full-scale measurements and method validation of container ship wave-induced motion at the port of fremantle. *Journal of Waterway, Port, Coastal and Ocean Engineering*, vol. 144, no. 6, pp. 1–24. ISSN 0733950X.

Haward, B.M., Lewis, C.H. and Griffin, M.J. (2009). Motions and crew responses on an offshore oil production and storage vessel. *Applied Ergonomics*, vol. 40, no. 5, pp. 904–914. ISSN 00036870.
Available at: http://dx.doi.org/10.1016/j.apergo.2009.01.001

Hochkirch, K. and Mallol, B. (2013). On the Importance of Full-Scale CFD Simulations for Ships. In: *12th International Conference on Computer Applications and Information Technology in the Maritime Industries (COMPIT 2013)*, pp. 85–95. Cortona, Italy.

Höfler, M. and Höfler, T. (2017). *Sea State Estimation in the Time Domain*. Master's thesis, Technical University of Denmark.

Holthuijsen, L.H. (2007). *Waves in oceanic and coastal waters*. Cambridge University Press, Delft, The Netherlands. ISBN 0521860288.

Ikeda, Y., Himeno, Y. and Tanaka, N. (1978). Components of roll damping of ship at forward speed. *Journal of the Society of Naval Architects of Japan*, vol. 1978, no. 143, pp. 113–125.

IMO (2009). Guidelines For Voluntary Use Of The Ship Energy Efficiency Operational Indicator (EEOI). Tech. Rep., MEPC.1/Circ.684, London.

ITTC (2011). Practical guidelines for ship CFD applications. In: *Proceedings of the 26th ITTC*.

ITTC (2014*a*). Practical guidelines for ship CFD applications. In: *Proceedings of the 27th ITTC*.

ITTC (2014*b*). Seakeeping Experiments. In: *Proceedings of the 27th ITTC*.

ITTC (2017*a*). Recommended Procedures and Guidelines - Global Loads and Seakeeping Procedure. In: *Proceedings of the 28th ITTC*.

ITTC (2017*b*). Uncertainty Analysis in CFD Verification and Validation Methodology and Procedures. In: *Proceedings of the 28th ITTC*.

Jiao, J., Ren, H., Adenya, C.A. and Chen, C. (2017). Development of a shipboard remote control and telemetry experimental system for large-scale model's motions and loads measurement in realistic sea waves. *Sensors (Switzerland)*, vol. 17, no. 11. ISSN 14248220.

Jin, Y., Chai, S., Duffy, J., Chin, C. and Bose, N. (2017). URANS predictions of wave induced loads and motions on ships in regular head and oblique waves at zero forward speed. *Journal of Fluids and Structures*. ISSN 10958622.

Journée, J. and Massie, W. (2001). *Offshore Hydrodynamics*. First edition edn. Delft University of Technology.

Judge, C.Q. (2019). EN455 Course Notes in Seakeeping and Maneuvering.
Available at: https://www.usna.edu/NAOE/academics/en455.php

Kalman, R.E. (1960). A new approach to linear filtering and prediction problems. *Transactions of the ASME–Journal of Basic Engineering*, vol. 82, no. Series D, pp. 35–45.

Kapsenberg, G.K. (2011). Slamming of ships: Where are we now? *Philosophical Transactions of the Royal Society A: Mathematical, Physical and Engineering Sciences*, vol. 369, no. 1947, pp. 2892–2919. ISSN 1364503X.

Kim, P. (2011). *Kalman Filter for Beginners with MATLAB Examples*. A-JIN Publishing Company. ISBN 1463648359.

Kim, S.P. (2013). CFD as a seakeeping tool for ship design. *International Journal of Naval Architecture and Ocean Engineering*, vol. 3, no. 1, pp. 65–71. ISSN 2092-6782.
Available at: http://dx.doi.org/10.2478/IJNAOE-2013-0046

Kim, Y.C., Kim, K.S., Kim, J., Kim, Y., Park, I.R. and Jang, Y.H. (2017). Analysis of added resistance and seakeeping responses in head sea conditions for low-speed full ships using URANS approach. *International Journal of Naval Architecture and Ocean Engineering*. ISSN 20926790.

Koning, J. (nd). Xsens MTi Measuring Ship Movements.
Available at: https://www.xsens.com/cases/xsens-mti-measuring-ship-movements

Küchler, S., Eberharter, J.K., Langer, K., Schneider, K. and Sawodny, O. (2011). Heave Motion Estimation of a Vessel Using Acceleration Measurements. *IFAC Proceedings Volumes*, vol. 44, no. 1, pp. 14742–14747. ISSN 1474-6670.
Available at: http://www.sciencedirect.com/science/article/pii/S1474667016459975

Labbe, R.R. (2020). Kalman and bayesian filters in python. https://github.com/rlabbe/Kalman-and-Bayesian-Filters-in-Python.

Lagemann, B. (2019). *Efficient seakeeping performance predictions with CFD*. Master's thesis, KTH, Naval Systems.

Lewandowski, E.M. (2004). *The dynamics of marine craft*. WORLD SCIENTIFIC, Singapore. ISBN 9810247559.

Liu, Y. (2003). On second-order roll motions of ships. In: *Proceedings of the 22nd International Conference on Offshore Mechanics and Arctic Engineering*, vol. 1, pp. 33–38. Cancun, Mexica.

Lloyd, A.R.J.M., Hosoda, R., Robinson, D.W., Nicholson, K. and Victory, G. (1991). Seakeeping [and discussion]. *Philosophical Transactions: Physical Sciences and Engineering*, vol. 334, no. 1634, pp. 253–264. ISSN 09628428.

Lucas, M. (2012). A new ship for polar research.
Available at: https://seamester.co.za/

Luus, J. (2019). The determination of rigid body motion with sensor fusion. Tech. Rep., Stellenbosch University, Stellenbosch.

Maersk (nd). Slow steaming-the full story.
Available at: https://www.yumpu.com/en/document/read/7803715/slow-steaming-the-full-story-maersk

Manzke, M. and Rung, T. (2010). Resistance prediction and seakeeping analysis with FreSCo+. In: *Proceedings from Gothenburg 2010-A Workshop on Numerical Ship Hydrodynamics*. Gothenburg.

McCann, J. (2019). *Wild Sea - A History of the Southern Ocean*. University of Chicago Press. ISBN 978-0-226-62238-5.

Montazeri, N. (2016). *Estimation of waves and ship responses using onboard measurements*. PhD Thesis, Technical University of Denmark.

Montazeri, N., Nielsen, U.D. and Juncher Jensen, J. (2016). Estimation of wind sea and swell using shipboard measurements - A refined parametric modelling approach. *Applied Ocean Research*, vol. 54, pp. 73–86. ISSN 01411187.
Available at: http://dx.doi.org/10.1016/j.apor.2015.11.004

Moton, C.J. (1991). Open-water resistance and seakeeping characteristics of ships with icebreaking bows. Tech. Rep. Trident Scolar Report No. 184, United States Naval Academy, Annapolis, Maryland.

National Maritime Research Institute (2015). A Workshop on CFD in Ship Hydrodynamics. Tokyo.
Available at: https://t2015.nmri.go.jp/

Nielsen, U. (2005). *Estimation of directional wave spectra from measured ship responses*. Ph.D. thesis.

Nielsen, U.D., Brodtkorb, A.H. and Sørensen, A.J. (2018). A brute-force spectral approach for wave estimation using measured vessel motions. *Marine Structures*, vol. 60, pp. 101–121. ISSN 0951-8339.
Available at: http://www.sciencedirect.com/science/article/pii/S0951833917303209

Niklas, K. and Pruszko, H. (2019). Full scale cfd seakeeping simulations for case study ship redesigned from v-shaped bulbous bow to x-bow hull form. *Applied Ocean Research*, vol. 89, pp. 188 – 201. ISSN 0141-1187.

Ntamba Ntamba, B.M., Schwarz-Röhr, B., Zhang, C. and Härting, A. (2019). Full scale measurement of ship motions to validate strip theory. In: *5th MASHCON: International conference on ship manoeuvring in shallow and confined water with non-exclusive focus on manoeuvring in waves, wind and current*, pp. 297–303. Knowledge centre manoeuvring in shallow and confined water.

NUMECA International (2020*a*). *Tutorials - FINE®/Marine 8.2*.

NUMECA International (2020*b*). *User Guide - HEXPRESS™ 8.2*.

Oberhagemann, J., Moctar, O.E., Holtmann, M., Schellin, T., Bertram, V. and Kim, D. (2010). Hydro-Elastic Simulation of Stern Slamming and Whipping. *The International Journal of Ocean and Climate Systems*, vol. 1, no. 3-4, pp. 179–188. ISSN 1759-3131.

Omer, H and Bekker, A. (2016*a*). Detection of wave slamming sites from ship deflections. *R & D Journal of the South African Institution of Mechanical Engineering*, vol. 32, pp. 50–57.

Omer, H. (2016*b*). *The Impact of Wave Slamming Induced Vibration on Human Factors and Equipment*. Master's thesis, Stellenbosch Univeristy.

Omer, H. and Bekker, A. (2018). Human responses to wave slamming vibration on a polar supply and research vessel. *Applied Ergonomics*, vol. 67, pp. 71–82. ISSN 18729126.

Otzen, J. and Simonsen, C. (2010). Uncertainty Assessment for KCS Resistance and Propulsion Tests in Waves. Tech. Rep., FORCE Technology, Lyngby.

Padgaonkar, A., Krieger, K. and King, A. (1975). Measurement of Angular Acceleration of a Rigid Body Using Linear Accelerometers. *Journal of Applied Mechanics*, vol. 42, no. 3, pp. 552–556.

Perez, T. (2005). *Ship Motion Control: Course Keeping and Roll Stabilisation Using Rudder and Fins*. Springer, London. ISBN 9781849969789.

Perez, T. and Blanke, M. (2002). Mathematical Ship Modeling for Control Applications. Tech. Rep., Technical University of Denmark.

Pérez-Rojas, L., Oliva-Remola, A. and Goicoechea, M. (2019). On the sinkage of ships. In: *Proceedings of the 25th Pan-American Conference of Naval Engineering—COPINAVAL*, pp. 129–138. Springer International Publishing, Cham. ISBN 978-3-319-89812-4.

Pisula, P.J., Lewis, C.H. and Bridger, R.S. (2012). Vessel motion thresholds for maintaining physical and cognitive performance: A study of naval personnel at sea. *Ergonomics*, vol. 55, no. 6, pp. 636–649. ISSN 00140139.

Ponkratov, D. (2017). 2016 Workshop on Ship Scale Hydrodynamic Computer Simulation. *Lloyd's Register*, , no. February, p. 225.

Ramberg, A. (2017). *Ocean Waves Estimation : An Artificial Intelligence Approach*. Master's thesis, Mälardalen University, School of Innovation, Design and Engineering.

Rhasatsha (2020). University of Stellenbosch HPC. http://www.sun.ac.za/hpc.

Riska, K. (2010). Design of Ice Breaking Ships. *Encyclopaedia of Life Support Systems*.

Ronen, D. (2011). The effect of oil price on containership speed and fleet size. *Journal of the Operational Research Society*, vol. 62, no. 1, pp. 211–216. ISSN 14769360. Available at: http://dx.doi.org/10.1057/jors.2009.169

Saad, B. (2014). *Development of a practical tool to determine the hull damping of modern ship hull forms*. Masters Thesis, University of Rostock.

Salmony, P. (2018). IMU Attitude Estimation.
Available at: http://philsal.co.uk/projects/imu-attitude-estimation

SCALE (2019). SCALE (Southern oCean seAsonaL Experiment).
Available at: http://scale.org.za/

Schobeiri, M.T. (2010). *Fluid mechanics for engineers: A graduate textbook*. ISBN 9783642115936.

Schoop-Zipfel, K.J. (2016). *Efficient Simulation of Ship Maneuvers in Waves*. PhD Thesis, Hamburg University of Technology.

Seif, M.S., Mehdigholi, H. and Najafi, A. (2014). Experimental and numerical modeling of the high speed planing vessel motion. *Journal of Marine Engineering & Technology*, vol. 13, no. 2, pp. 62–72. ISSN 2046-4177.

Seo, S., Park, S. and Koo, B.Y. (2017). Effect of wave periods on added resistance and motions of a ship in head sea simulations. *Ocean Engineering*, vol. 137, no. October 2016, pp. 309–327. ISSN 00298018.
Available at: http://dx.doi.org/10.1016/j.oceaneng.2017.04.009

Simonsen, C.D., Otzen, J.F., Joncquez, S. and Stern, F. (2013). EFD and CFD for KCS heaving and pitching in regular head waves. *Journal of Marine Science and Technology (Japan)*, vol. 18, no. 4, pp. 435–459. ISSN 09484280.

Sirigu, S.A., Bracco, G., Bonfanti, M., Dafnakis, P. and Mattiazzo, G. (2018). Onboard sea state estimation method validation based on measured floater motion. *IFAC-PapersOnLine*, vol. 51, no. 29, pp. 68–73. ISSN 24058963.
Available at: https://doi.org/10.1016/j.ifacol.2018.09.471

Skandali, D. (2015). *Identification of response amplitude operators for ships based on full scale measurements*. Masters Thesis, Technische Universiteit Delft.

Skelton, P. (2014). The South African Antarctic and Southern Ocean Research Plan 2014-2024. Tech. Rep., The National Research Foundation.

Soal, K.I. (2014). *Vibration response of the polar supply and research vessel the S . A . Agulhas II in Antarctica and the Southern ocean*. Masters thesis, Stellenbosch University.

St. Denis, M. and Pierson, W.J. (1953). On the Motions of Ships in Confused Seas. *Transactions Society of Naval Architects and Marine Engineers*.

Stern, F., Wilson, R. and Shao, J. (2006). Quantitative V&V of CFD simulations and certification of CFD codes. *International Journal for Numerical Methods in Fluids*. ISSN 02712091.

Storsul, M.T. (2019). *A CFD Study of Numerical Wave Tanks*. Masters, Norwegian University of Science and Technology.

Suominen, M., Karhunen, J., Bekker, A., Kujala, P., Elo, M., Von Bock Und Polach, R., Enlund, H. and Saarinen, S. (2013). Full-scale measurements on board PSRV S.A. Agulhas II in the Baltic Sea. In: *Proceedings of the International Conference on Port and Ocean Engineering under Arctic Conditions, POAC*. ISSN 20777841.

Tezdogan, T., Demirel, Y.K., Kellett, P., Khorasanchi, M., Incecik, A. and Turan, O. (2015). Full-scale unsteady RANS CFD simulations of ship behaviour and performance in head seas due to slow steaming. *Ocean Engineering*, vol. 97, pp. 186–206. ISSN 00298018.
Available at: http://dx.doi.org/10.1016/j.oceaneng.2015.01.011

Tezdogan, T., Incecik, A. and Turan, O. (2014). Operability assessment of high speed passenger ships based on human comfort criteria. *Ocean Engineering*, vol. 89, pp. 32–52. ISSN 00298018.
Available at: http://dx.doi.org/10.1016/j.oceaneng.2014.07.009

Titterton, D.H. and Weston, J.L. (2004). *Strapdown Inertial Navigation Technology*. 2nd edn. The Institution of Electrical Engineers. ISBN 0-86341-358-7.

Toffoli, A. and Bitner-Gregersen, E.M. (2017). *Types of Ocean Surface Waves, Wave Classification*, pp. 1–8. American Cancer Society. ISBN 9781118476406.

Van Dokkum, K. (2014). *Ship knowledge: ship design, construction and operation*. 10th edn. Dokmar Maritime Publishers B.V., Vlissingen. ISBN 978-90-71500-40-4.

Van Zijl, C.M. (2020). *Operational Modal Analysis on the SA Agulhas II*. Masters thesis, Stellenbosch University.

Versteeg, H.K. and Malalasekera, W. (2007). *An Introduction to Computational Fluid Dynamics 2nd Edition*. ISBN 9780131274983.

Vogt, J.W., Bovio, M. and Mallol, B. (2016). Validation of Wind Loads on a Slender Vessel using CFD. Tech. Rep., DAMEN.

WAFO-group (2000). *WAFO - A Matlab Toolbox for Analysis of Random Waves and Loads - A Tutorial*. Math. Stat., Center for Math. Sci., Lund Univ., Lund, Sweden.